Geometric and electronic structures of low-dimensional materials

Yanlin Gao

February 2019

Geometric and electronic structures of low-dimensional materials

Yanlin Gao
Doctoral Program in Nano-Science and Nano-Technology

Submitted to the Graduate School of
Pure and Applied Sciences
in Partial Fulfillment of the Requirements
for the Degree of Doctor of Philosophy in Science

at the
University of Tsukuba

Abstract

Low-dimensional materials exhibit peculiar electronic properties arising from their dimensionality and atomic network topology, which makes them important materials in the current nanoscale sciences and technologies. In this thesis, we focus on geometric and electronic properties of low-dimensional materials, *i.e.*, a sheet consisting of hexagonally arranged Ga and N atoms (h-GaN) and graphene derivatives using the density functional theory (DFT).

We studied geometric and electronic properties of h-GaN under the biaxial compression, surface hydrogenation, and external electric field. The h-GaN sheet preserves the planar conformation under an equilibrium lattice constant of 3.2 Å. The h-GaN is a semiconductor with an indirect band gap of 2.28 eV between the Γ and K points. The biaxial compressive strain causes structural buckling on h-GaN, leading to polarization normal to the atomic layer, which is tunable by attaching H atoms on Ga and N atoms. An external electric field normal to the layer also causes structural buckling, whose height is proportional to the field strength. In addition to the monolayer h-GaN, we also investigated energetics and electronic structures of h-GaN thin films and hybrid structures with graphene and monolayer h-BN. The h-GaN sheets in the thin films are tightly bound each other owing to the small interlayer spacing, so that their electronic structures are sensitive to the number of layers. We further found that GaN thin films with a wurtzite structure undergo a structural phase transition into the layered structure of h-GaN by applying a biaxial tensile strain. For h-GaN heterostructures with graphene and h-BN, the optimum interlayer spacing is 3.4 Å for both cases, indicating that the h-GaN sheet is bound to the graphene or h-BN via a weak van der Waals interaction.

Electronic properties of graphene edges under a lateral electric field in regard to their edge shapes and terminations were studied to provide a theoretical insight into their field emission properties. The field emission property of graphene is sensitive to its edge shape and termination. The armchair edge shows the largest emission current due to its smallest electrostatic potential barrier among all edge shapes studied here. The electric field outside the chiral edges is spatially modulated along the edge because of the inhomogeneous charge density at the edge atomic sites arising from the bond alternation. The graphene edges functionalized by H, OH, and COOH cause relatively large emission current for a wide range of the electric field due to the decrease in the electrostatic potential barriers caused by the dipoles at the edge, while O and CHO terminations substantially suppress the current by increasing the potential barrier. In addition, the NH group increases and decreases the field emission current from the zigzag and armchair edges, respectively, because of the different electrostatic environment around the edge atomic sites arising from its conformations.

Contents

Chapter 1

Introduction

Layered materials consist of two-dimensional (2D) covalent networks which are stacked each other via weak van der Waals interactions. The weak interlayer interaction allows them to be exfoliated into an isolated 2D sheet; therefore, the layered materials are thought to be the source of 2D materials. Several 2D materials, such as graphene, silicene, germanene, hexagonal boron nitride (h-BN), and transition metal dichalcogenides (TMDCs), have been successfully synthesized. These 2D materials exhibit peculiar electronic properties ascribed to their dimensionality and atomic network topology, which makes them important materials in the current nanoscale sciences and technologies.

1.1 Graphene

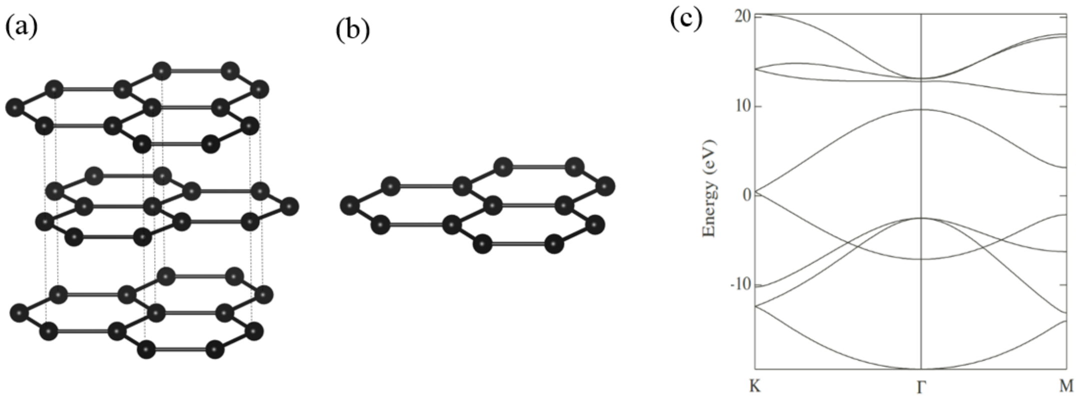

Figure 1.1: Geometric structures of (a) graphite and (b) graphene. (c) Electronic structure of graphene obtained by the generalized tight binding approximation.

Graphene is a 2D carbon (C) allotrope consisting of hexagonally arranged C atoms, which has been exfoliated from graphite [Figs. 1.1(a) and 1.1(b)] [1]. This hexagonal network with a single-atom thickness leads to the peculiar electronic band structure characterized by linear dispersion bands around the six corners of the hexagonal Brillouin zone and at the Fermi level (E_F) [Fig. 1.1(c)]. Because of this electronic structure, electrons in graphene behave as massless Dirac fermions, whose speed is around 1/300 of the light speed, producing a high carrier mobility and conductivity [2, 3, 4, 5]. Indeed, graphene has a carrier mobility of up to $200,000$ cm^2/(V·s) [2, 3, 4] and the low resistivity of 10^{-6} Ω which is less than that of silver and copper at room temperature [5]. In addition, the quantum Hall effect can be observed in graphene [6], and the quantum spin Hall effect may also occur under ultralow temperature due to the existence of spin-orbital coupling [7]. Owing to the strong 2D hexagonal covalent network, graphene has outstanding mechanical, thermal, and optical properties: 1 Tpa Young's modulus [8], 5000 W/(m·K) thermal conductivity [9], and 97.7 % light transmittance. These properties enable graphene a constituent material of functional devices with tremendous performance, such as field emission source, solar cells, supercapacitor, electronics, photodetector, and sensing devices [1, 6, 10].

1.2 Graphene-like 2D materials

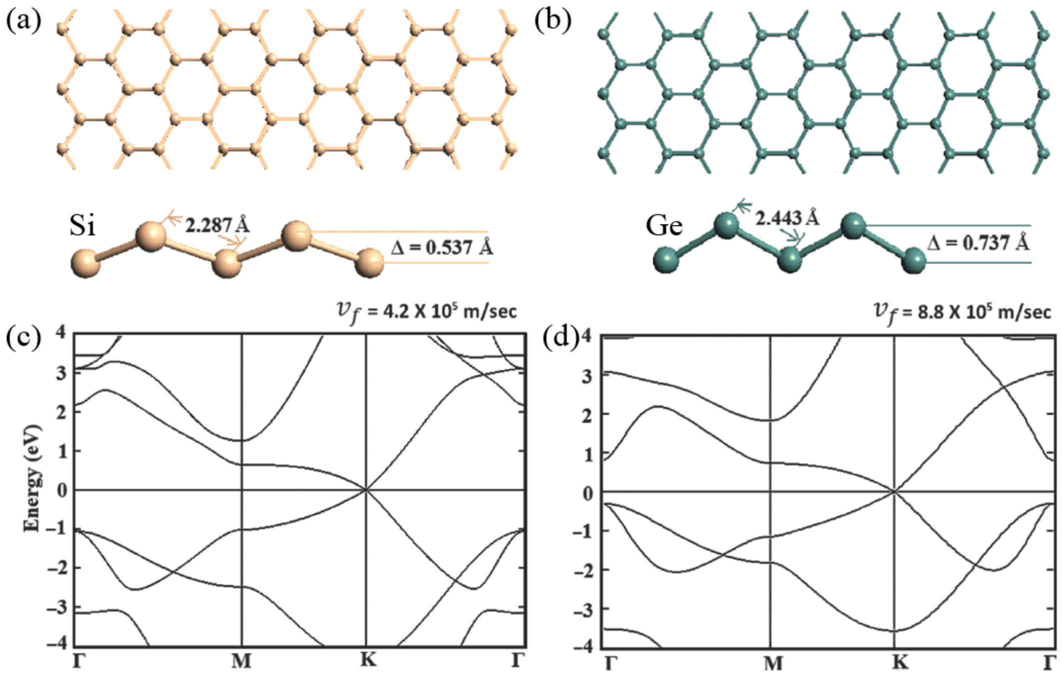

Figure 1.2: Geometric structures of (a) silicene and (b) germanene. Electronic structures of (c) silicene and (d) germanene [11].

Following the discovery of graphene, various 2D materials have been indeed synthesized using appropriate experiment techniques. These materials show interesting variations in the electronic structure, arising from different constituent elements and network morphologies.

Silicon and germanium can form 2D hexagonal networks, because they are isoelectronic to carbon. These 2D allotropes of silicon and germanium are known as silicene and germanene, respectively, and have been synthesized on substrates [12, 13, 14]. In spite of 2D hexagonal covalent networks, because of the weak π-π interaction between atoms, they have a buckled honeycomb structure rather than planar structure as shown in Figs. 1.2(a) and 1.2(b). Free-standing silicene and gemanene qualitatively have the same electronic structure as graphene due to their hexagonal network topology [Figs. 1.2(c) and 1.2(d)] [15], leading to massless fermions at the E_F. However, distinct from graphene, the buckled structures make them sensitive to the external electric field, so that their band gaps can be opened by an external electric field normal to the layer, because atoms in a buckled structure are no longer equivalent under the electric field. In addition, since they have strong spin orbital coupling effect due to the heavy atomic mass and buckled structure, spin Hall effect has been expected under a relatively high temperature [16].

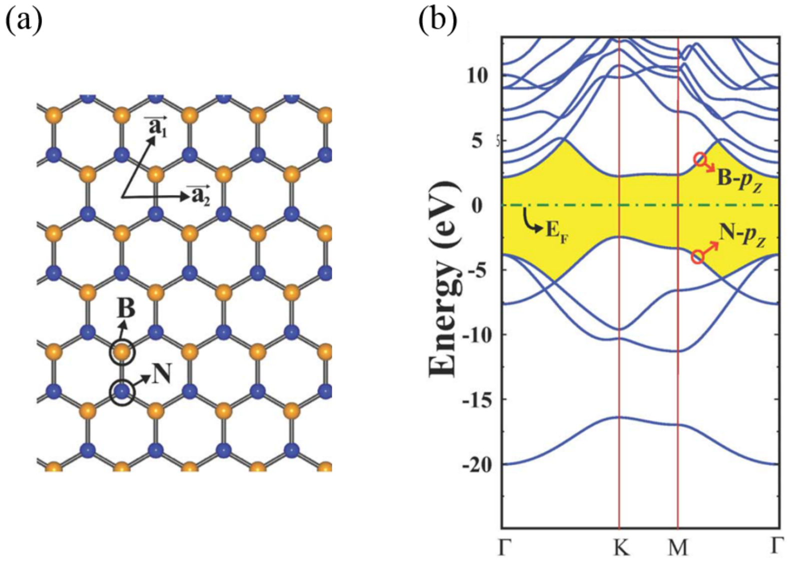

Figure 1.3: (a) Geometric and (b) electronic structures of h-BN sheet [17].

In addition to group IV elements, the combination of appropriate elements, *e.g.* III and V elements, is expected to have 2D layered structures. For example, B and N can have a graphene-like structure in which they are alternately arranged, because of their isoelectronicity to carbon [Fig. 1.3 (a)]. In this case, due to the electronegativity difference between the constituent elements forming the honeycomb lattice, monolayer h-BN is an insulator with large energy gap of about 5 eV between the valence band top contributed from N atoms and the conduction band bottom from B atoms [Fig. 1.3(b)], even though it also shares similar geometrical features with graphene. The atom thickness, insulating property, and chemical stability enable it

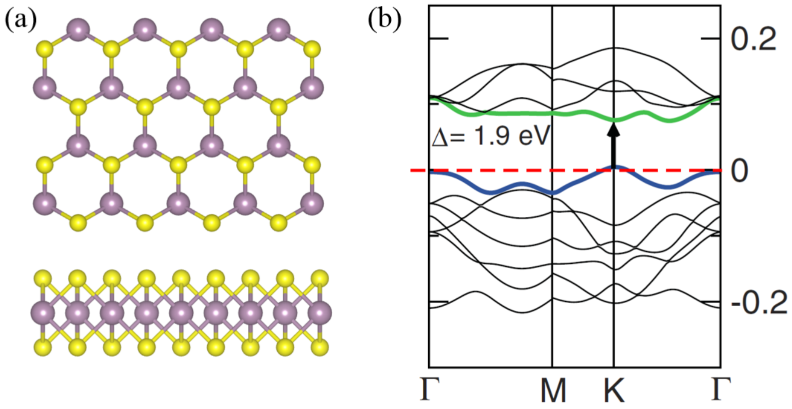

Figure 1.4: (a) Geometric and (b) electronic structures of MoS_2 sheet [18].

to be a good dielectric layer for electronic devices consisting of semiconducting 2D materials [19].

A molybdenum sulphide (MoS_2) sheet, as a prototypical TMDC, consists of a Mo atomic layer sandwiched by S atomic layers coordinated in a triangular prismatic fashion, so that the atoms in MoS_2 also follow a hexagonal arrangement [Fig. 1.4 (a)]. In contrast to graphene, an isolated MoS_2 sheet is a semiconductor with a direct band gap of 1.9 eV [Fig. 1.4(b)] [18, 20]. Absence of inversion symmetry causes the valley Hall effect. Furthermore, *d*-orbitals of Mo cause a strong spin-orbit coupling, which makes it a promising material for spintronic devices.

1.3 Structural modulation of 2D materials

Most of 2D materials can be a starting material for novel nanostructures possessing unusual physical properties by imposing additional boundary conditions (Fig. 1.5). Nanoribbons are representative examples of such nanostructures derived from 2D materials by imposing an open boundary condition. Depending on the edge shape, such nanoribbons exhibit interesting variations in their electronic structures which are absent in the 2D structures. For the case of graphene (Fig. 1.6), armchair graphene nanoribbons (AGNRs) are metals or semiconductors depending on the ribbon width: the band gap oscillates with triple periodicity of the ribbon width and asymptotically decreases with increasing the width. Chiral graphene nanoribbons are metals or semiconductors depending on their ribbon width and edge shape: the gap decreases not only with increasing the ribbon width but also with changing the edge angle from armchair to zigzag. In contrast, zigzag graphene nanoribbons (ZGNRs) are metals with half-filed flat dispersion bands in the Brillouin zone boundary owing to the delicate balance of the electron transfer among the atoms near the edge (Fig. 1.7) [21, 22, 23], irrespective of the ribbon width.

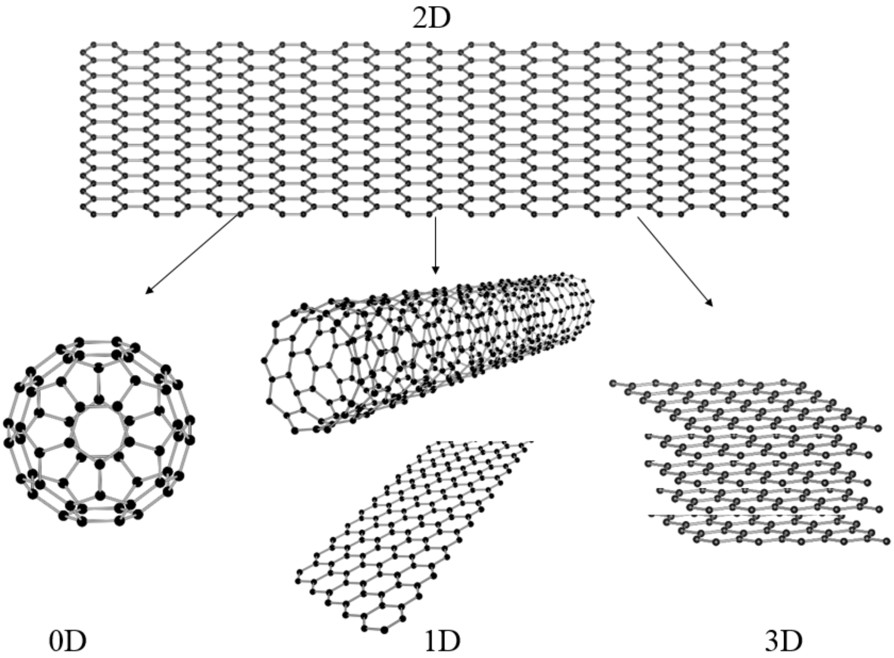

Figure 1.5: 2D material and designed novel structures from the 2D material.

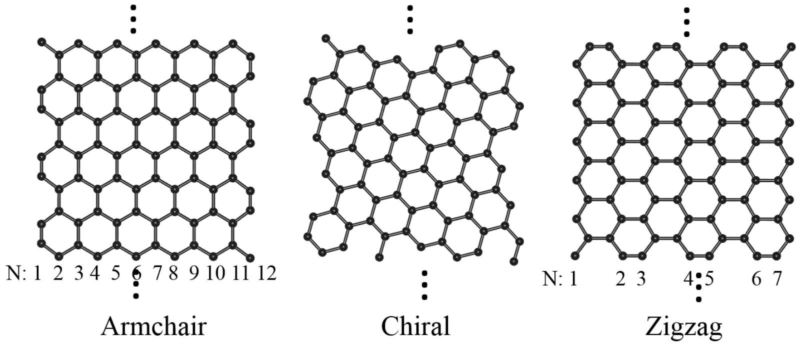

Figure 1.6: Geometric structures of armchair, chiral and zigzag nanoribbons.

Other 2D materials, such as silicene, germanene, TMDCs and h-BN, may also form a strip structure with nanometer width and various edge morphologies [17, 24, 25, 26, 27, 28, 29, 30]. For example, zigzag MoS_2 nanoribbons are metals with ferromagnetic edge states regardless of the passivation, but armchair MoS_2 nanoribbons are semiconductors, whose band gap decreases with the increase of the ribbon width, and converges to a certain value smaller than that of the monolayer MoS_2 [Fig. 1.9(a)] [27, 28, 29, 30]. Armchair h-BN nanoribbons (BNNRs) are semiconductors, whose band gap oscillates by increasing the ribbon width. Zigzag and chiral BNNRs with bare edges are metallic, owing to unsaturated σ bonds at the zigzag portion of their edges [Fig. 1.9(b)] [17, 26, 31].

The interaction among layers in 2D materials also plays a crucial role for modulating their electronic properties. The electronic band structure of a multilayer graphene is sensitive to its stacking arrangement and the number of layers. A

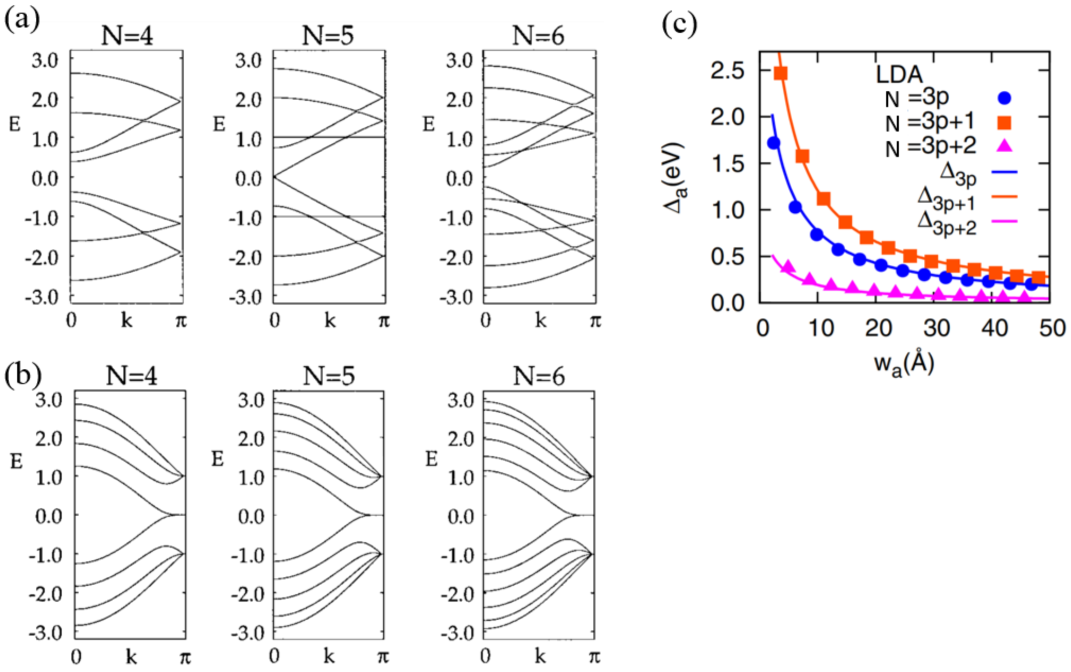

Figure 1.7: Band structures of (a) AGNRs and (b) ZGNRs with ribbon width N (N=4, 5 and 6) [21]. (c) The variation of band gaps of AGNRs with increasing the ribbon width N [23].

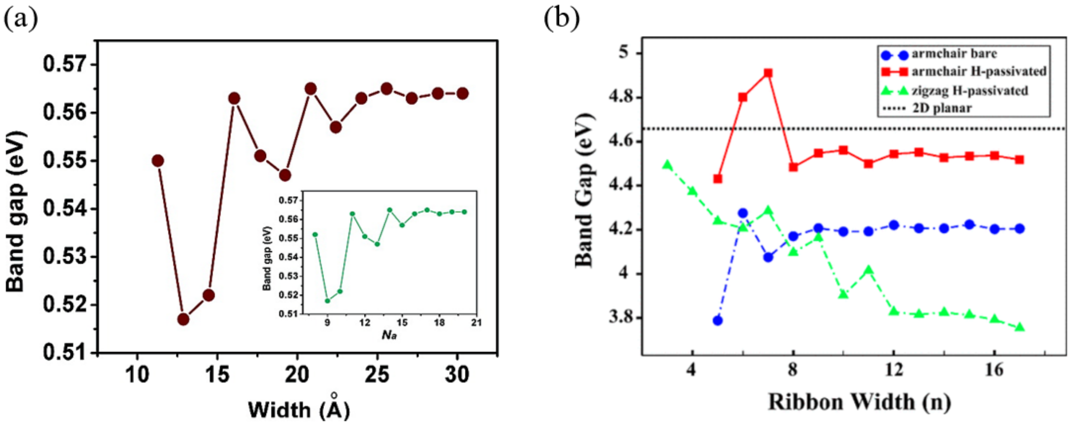

Figure 1.8: The variation of band gaps of (a) MoS_2 armchair nanoribbon [27] and (b) h-BN nanoribbon with increasing the ribbon width [17].

monolayer graphene possesses pairs of linear dispersion bands, and its carries behave as massless Dirac fermions, leading to extremely high carrier mobility. A bilayer graphene with AB (Bermal) stacking arrangement, however, has parabolic dispersion bands around the E_F because of the interlayer interaction, which leads to a finite carrier mass. Furthermore, the weak van der Waals interaction allows graphene to form thin films with two kinds of stacking arrangements, *i.e.*, the ABA (Bermal) and ABC (rhombohedral) stacking arrangements. The electronic structure of graphene thin films with Bernal stacking depends on the number of layers:

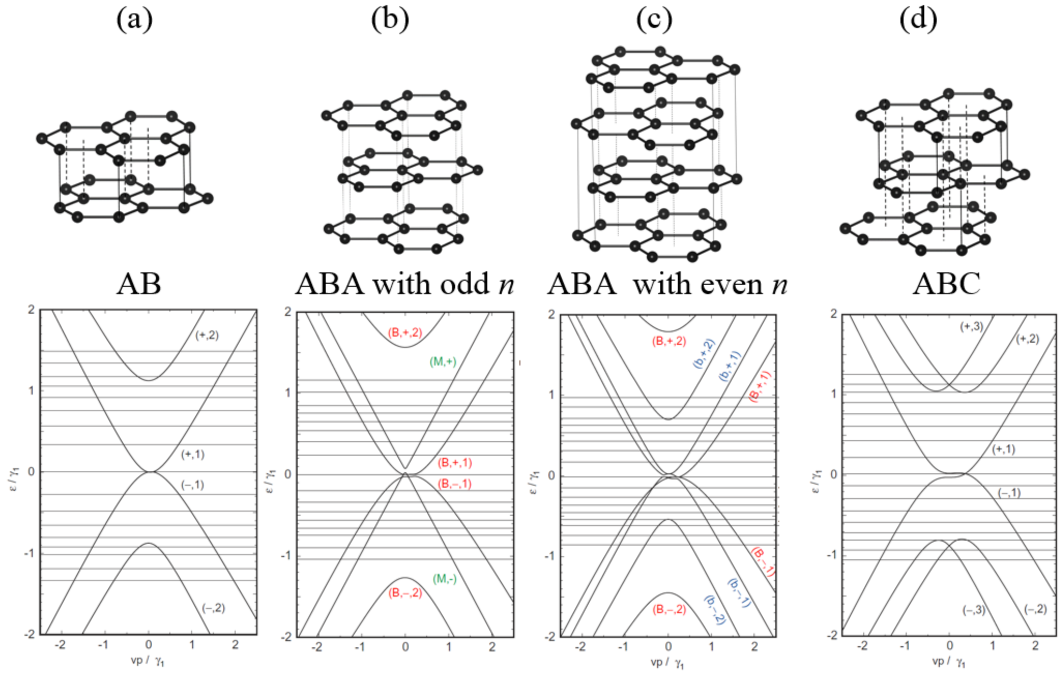

Figure 1.9: Geometric and electronic structures of (a) AB stacked bilayer, (b) ABA stacked three-layer, (c) ABA stacked four-layer, and (d) ABC stacked three-layer graphene [32], n indicate the layer number of graphene.

it shows parabolic bands for films with even graphene layers, but a combination of quadratic bands and linear bands for systems with odd graphene layers. Thin films with ABC staking are metals with a pair of flat bands around the E_F and the vicinity of the K point (Fig. 1.9) [32, 33, 34, 35]. As an analogue of graphene, a similar variation in band structure has been observed in silicene films, depending on the interlayer stacking arrangement and the numbers of layers [36]. MoS_2 is found to undergo a transition in the electronic structure from a semiconductor with a direct band gap of 1.9 eV to that with an indirect band gap of 1.29 eV by forming multi-layered stacking structures [18]. In contrast, the band gaps of h-BN sheets hardly change with the number of sheets.

Hybrid structures consisting of 2D materials and foreign materials may cause further modulation in their electronic properties, owing to the symmetry breaking brought by the interaction with foreign materials [37, 38, 39, 40]. Specifically, several heterostructures involving graphene have been synthesized and exhibit novel properties far beyond their simplex superposition. The electronic structure of van der Walls heterostructures consisting of graphene and h-BN depends on the stacking arrangement and interlayer spacing [37, 39]. Superlattices consisting of graphene and MoS_2 exhibits metallic electronic properties owing to the charge transfer between them, causing a small gap in the Dirac cone at the K point, which are different from the simple superposition of the electronic structures of the isolated graphene and monolayer MoS_2 [38]. It is also theoretically proved that the electronic structures of monolayer h-BN, h-AlN, and h-GaN can be easily tuned by forming heterostructures with monolayer MoS_2. The heterostructures, h-AlN/MoS_2 and h-GaN/MoS_2, are direct band gap semiconductors with narrower band gap than that of monolayer h-AlN and h-GaN which have the indirect band gaps [40].

1.4 Application of 2D materials in field emission

Electrons in materials are strongly bound by the deep ionic potential. By applying external physical stimuli, electrons overcome or go through the potential, emitting from their surfaces. Depending to the physical stimuli, the electron emission can be roughly classified into thermal electron emission, photoelectron emission, and field emission. For the thermal electron emission and photoelectron emission, electrons get adequate energy to overcome the potential barrier. For the field emission, an external electric field narrows and lowers the potential barrier of the material surfaces, enabling the electrons to tunnel through the barrier.

Field emission is a quantum mechanical process of electrons tunneling through the potential barrier of surfaces of materials (metal or semiconductor) to vacuum under a strong electric field of the order of 10^6–10^7 V/cm. The Fowler–Nordheim (F–N) theory gives the relation among the field emission current density I, electric field F, and the work function ϕ of the material surface with the following formula:

$$I = \frac{a\beta^2 F^2}{\phi} \exp(-\frac{b\phi^{3/2}}{\beta F}) \tag{1.1}$$

$$\beta = \frac{-6.8 \times 10^3 \phi^{3/2}}{m}, \tag{1.2}$$

where $a = 1.54 \times 10^{-6}$ A $\cdot$ eV/V^2, $b = 6.83 \times 10^9$ eV$^{-3/2} \cdot$ V/m, β is the field enhancement factor at the material surface, and m is the slope of the F–N plot, obtained by $\ln(I/F^2)$ versus $1/F$. Several materials, such as molybdenum, silicon, and diamond, have been reported to work as the electron emission sources of field emission devices. Among such materials, 2D materials realize the substantial emission current owing to their structural morphology.

2D materials have been attracting much attention as the constituent material for field emission devices, because of their geometric and electronic structures: their atom thickness enlarges the local electric field outside them, and 2D conducting area leads to a large current and fast heat dispersion [41, 42, 43, 44, 45, 46, 47]. Erande *et al.* fabricated few-layered black phosphorus nanosheet emitters, showing a turn-on electric field of 4.2 V/μm at the current of 10 μA/cm^2. Suryawanshi *et al.* fabricated WS_2 planar emitters and provided the mechanism of the current fluctuation [41]. It was reported that the BN sheets protruding from the ZnS nanowire shows superior field emission properties with a turn-on electric field of 1.9 V/μm, field enhancement factor of 1600, and small field emission current fluctuation [44]. The turn-on electric field of the BN sheets with zigzag edges was reported to be as low as 1 V/μm [47].

Among 2D materials, graphene has received a great deal of attention because of its excellent electron emission properties such as low turn-on electric field, high emission current density, and long-term emission stability. Graphene-based emitters showed different field emission efficiency depending on the substrate and graphene morphology. It was experimentally reported that suspended edge atomic sites preferentially emit electrons compared with its other atomic sites deposited on supporting substrates [48, 49]. A graphene foam emitter derived from highly porous reduced graphene oxide (rGO) showed outstanding field emission properties with a turn-on electric field as low as 1.06 V/μm, and stable current of 9.2 mA/cm^2 for 22 hours. Jeong *et al.* demonstrated that the length of rGO arrays affects its field emission property and ZnO coating layers may further improve the emitting stability [50]. Zhang *et al.* investigated the effect of the morphology of few-layer graphene on the field emission property leading to the conclusion that the optimal morphology of few-layer graphene for the field emission is sharp corners, large height, and less amorphous carbon [51].

Although these experimental works showed that the graphene is applicable to the field emission devices, microscopic insight into the physical mechanisms of the field emission from the graphene edge is still unclear. In particular, a little is known on how the edge shape and termination affect the field emission properties. Indeed, theoretical researches on the field emission of graphene are only limited to clean and hydrogenated GNRs with armchair and zigzag edges [52, 53]. Thus, the physical mechanisms of the field emission from the chiral edges of graphene and effect of various functional groups on the field emission from graphene edge are still unclear.

1.5 Thesis objective

Objectives of this thesis are following. In Chapter 3, we aim to theoretically clarify the geometric and electronic structures of h-GaN under the structural modulation and an external electric field, on the basis of the density functional theory. In addition, we also aim to investigate the energetics and electronic structures of h-GaN thin films and its hybrid structures. In Chapter 4, we would like to clarify the electrostatic properties of GNRs in terms of the edge shape and functionalization, for providing microscopic insight into the field emission mechanism of graphene-based electron emitters.

Chapter 2

Calculation methods

In this chapter, theoretical methods used in this thesis are described. Computational procedures to solve many-body Schrödinger equation will be given in the section 2.1. To treat the electric field applied to the low-dimensional materials within the framework of the density functional theory (DFT), the effective screen medium (ESM) method is adopted and described in section 2.2.

2.1 Density functional theory

The density functional theory is a quantum mechanical approach for investigating the ground state of many-body electron systems, such as atoms, molecules, and solids, by using electron density instead of the wavefunction. This simplification substantially reduces computational cost, so that the DFT is widely used in the modern electronic structure calculations. In this section, I will explain the basic idea of the DFT proposed by Hohenberg and Kohn together with several approximations required for practical application of the DFT to the real systems [54, 55].

2.1.1 The Schrödinger equation of N-electron system

The electronic property of a material is determined by the motion of its electrons, which is described by the many-electron Schrödinger equation. By solving this equation, we can get all electronic information about this material. The Schrödinger equation describing a system with N electrons is

$$\hat{H}\psi(\boldsymbol{r}_1, ..., \boldsymbol{r}_N) = E\psi(\boldsymbol{r}_1, ..., \boldsymbol{r}_N), \tag{2.1}$$

$$\hat{H} = \hat{T}_e + \hat{V}_{ne} + \hat{V}_{ee}, \tag{2.2}$$

where $\psi(\boldsymbol{r}_1, ..., \boldsymbol{r}_N)$ denotes the wavefunction of the system with electron coordinates $(\boldsymbol{r}_1, ..., \boldsymbol{r}_N)$, E is the energy eigenvalue, and $\hat{H}$ is the Hamiltonian operator including three terms: the first term $\hat{T}_e$ is kinetic energy operator of electrons, the second term $\hat{V}_{ne}$ corresponds to the Coulomb attraction between nuclei and electrons, and the third term $\hat{V}_{ee}$ corresponds to the electron-electron interaction.

2.1.2 Hohenberg–Kohn theorems

Hohenberg and Kohn proposed two theorems, which simplify the N-electron problem by introducing the electron density of the ground states instead of treating many-body wavefunction [54].

(1) The first theorem: *the external potential* $V_{ne}(\boldsymbol{r})$ *is determined with a trivial additive constant by the corresponding ground-state electron density* $n_0(\boldsymbol{r})$. It means

$$n_0(\boldsymbol{r}) \Rightarrow V_{ne}(\boldsymbol{r}). \tag{2.3}$$

Since all N-electron systems have the same T_e and V_{ee}, the ground-state wavefunction $|\psi_0\rangle$ for each N-electron system is only associated with the number of electron N and the external potential V_{ne}. It was known that

$$N = \int n_0(\boldsymbol{r}) d\boldsymbol{r}, \tag{2.4}$$

hence, $|\psi_0\rangle$ is determined by $n_0(\boldsymbol{r})$ and $V_{ne}(\boldsymbol{r})$.

Since the ground-state electron density $n_0(\boldsymbol{r})$ can be obtained by the ground-state wavefunction $|\psi_0\rangle$ for the $\hat{H}$:

$$n_0(\boldsymbol{r}) = \langle\psi_0|\hat{n}|\psi_0\rangle. \tag{2.5}$$

Then, it is concluded that the ground-state electron density $n_0(\boldsymbol{r})$ is one-to-one mapping with the external potential $V_{ne}(\boldsymbol{r})$,

$$V_{ne}(\boldsymbol{r}) \Leftrightarrow n_0(\boldsymbol{r}). \tag{2.6}$$

Thus, all physical quantities of a system can be expressed as functionals of the electron density. By treating electron density $n(\boldsymbol{r})$ instead of wavefunction $|\psi_0\rangle$, the $3N$-dimensional problem of the many-body Schrödinger equation turns into 3-dimensional problem of the electron density. Since the density operator is

$$\hat{n}(\boldsymbol{r}) = \sum_{i=1}^{N} \delta(\boldsymbol{r} - \boldsymbol{r_i}), \tag{2.7}$$

the total energy of the system is expressed as:

$$\begin{aligned}
E[n(\boldsymbol{r})] &= T[n(\boldsymbol{r})] + V_{ee}[n(\boldsymbol{r})] + V_{ne}[n(\boldsymbol{r})] \\
&= F[n(\boldsymbol{r})] + V_{ne}[n(\boldsymbol{r})] \\
&= F[n(\boldsymbol{r})] + \langle\psi|\hat{V}_{ne}|\psi\rangle \\
&= F[n(\boldsymbol{r})] + \int \psi^*[\sum_{i=1}^{N} \upsilon_{ne}(\boldsymbol{r_i})]\psi d\boldsymbol{r_1}...d\boldsymbol{r_N} \\
&= F[n(\boldsymbol{r})] + \int \psi^*[\int \sum_{i=1}^{N} \upsilon_{ne}(\boldsymbol{r})\delta(\boldsymbol{r} - \boldsymbol{r_i})d\boldsymbol{r}]\psi d\boldsymbol{r_1}...d\boldsymbol{r_N} \\
&= F[n(\boldsymbol{r})] + \int \upsilon_{ne}(\boldsymbol{r})n(\boldsymbol{r})d\boldsymbol{r},
\end{aligned} \tag{2.8}$$

where $\upsilon_{ne}(\boldsymbol{r})$ is potential from the nuclei, and $F[n(\boldsymbol{r})]$ is a universal functional of the electron density $n(\boldsymbol{r})$ independent on external potential $\upsilon_{ne}(\boldsymbol{r})$.

(2) The second theorem: *the ground-state energy can be obtained variationally: the density that minimizes the total energy is the exact ground-state density*, which means

$$E[n(\boldsymbol{r})] \geqslant E[n_0(\boldsymbol{r})], \tag{2.9}$$

which gives the energy variational principle:

$$\delta\{E[n(\boldsymbol{r})] - \mu(\int n(\boldsymbol{r})d\boldsymbol{r} - N)\} = 0, \tag{2.10}$$

namely,

$$\frac{\delta[E[n(\boldsymbol{r})]}{\delta n(\boldsymbol{r})} = \mu, \tag{2.11}$$

where μ is a Lagrange multiplier to specify the number of electrons.

2.1.3 Kohn–Sham equation

To further reduce the complexity of the problem, Kohn and Sham separated the $F[n(\boldsymbol{r})]$ into three parts:

$$F[n(\boldsymbol{r})] = T_s[n(\boldsymbol{r})] + \frac{e^2}{2}\int \frac{n(\boldsymbol{r})n(\boldsymbol{r'})}{\mid \boldsymbol{r} - \boldsymbol{r'} \mid} d\boldsymbol{r}d\boldsymbol{r'} + E_{xc}[n(\boldsymbol{r})], \tag{2.12}$$

where the first term $T_s[n(\boldsymbol{r})]$ is a hypothetical kinetic energy of non-interacting electrons, the second term is the electrostatic potential energy between electrons, and the final term E_{xc} is the residues, which contains all quantum many-body effects in interacting electrons except the direct Coulomb interaction. E_{xc} is called as the exchange correlation energy. Thus, the total energy $E[n(r)]$ is rewritten as

$$E[n(\boldsymbol{r})] = T_s[n(\boldsymbol{r})] + \frac{e^2}{2}\int \frac{n(\boldsymbol{r})n(\boldsymbol{r'})}{\mid \boldsymbol{r} - \boldsymbol{r'} \mid} d\boldsymbol{r}d\boldsymbol{r'} + E_{xc}[n(\boldsymbol{r})] + \int \upsilon_{ne}(\boldsymbol{r})n(\boldsymbol{r})d\boldsymbol{r}. \tag{2.13}$$

Applying the variational principle of Eq.(2.11) to the $E[n(\boldsymbol{r})]$ of Eq.(2.13) with respect to the $n(\boldsymbol{r})$ according to the Hohenberg–Kohn theorem, we can obtain

$$\frac{\delta T_s[n(\boldsymbol{r})]}{\delta n(\boldsymbol{r})} + \upsilon_{eff} = \mu, \tag{2.14}$$

and

$$\upsilon_{eff} = \upsilon_{ne}(\boldsymbol{r}) + \int \frac{n(\boldsymbol{r'})}{\mid \boldsymbol{r} - \boldsymbol{r'} \mid} + \frac{\delta E_{xc}(\boldsymbol{r})}{\delta n[(\boldsymbol{r})]} = \upsilon_{ne}(\boldsymbol{r}) + \int \frac{n(\boldsymbol{r'})}{\mid \boldsymbol{r} - \boldsymbol{r'} \mid} + \upsilon_{xc}(\boldsymbol{r}), \tag{2.15}$$

where $\upsilon_{xc}(\boldsymbol{r})$ is the exchange correlation potential obtained by the functional derivative of E_{xc}. Kohn and Sham defined a electron density $n(\boldsymbol{r})$ in term of the one-body wavefunction $\psi_i(\boldsymbol{r})$ as:

$$n(\boldsymbol{r}) = \sum_{i=1}^{N} \mid \psi_i(\boldsymbol{r}) \mid^2 . \tag{2.16}$$

Then, $T_s[n]$ is expressed as:

$$T_s[n(\boldsymbol{r})] = \sum_{i=1}^{N} \langle \psi_i(\boldsymbol{r}) \mid -\frac{\hbar^2}{2m}\nabla^2 \mid \psi_i(\boldsymbol{r})\rangle. \tag{2.17}$$

By substituting the Eq. (2.17) into Eq. (2.14), we obtained

$$\left[-\frac{\hbar^2}{2m}\nabla^2 + \upsilon_{eff}(\boldsymbol{r})\right]\psi_i(\boldsymbol{r}) = \epsilon_i\psi_i(\boldsymbol{r}), \tag{2.18}$$

where ϵ_i is eigenenergy of electron. Equation (2.18) describes one electron motion under the effective potential υ_{eff}, containing the potential $\upsilon_{ne}(\boldsymbol{r})$ from the nuclei, electrostatic potential $\int \frac{n(\boldsymbol{r}')}{|\boldsymbol{r}-\boldsymbol{r}'|}$, and exchange-correlation potential $\upsilon_{ex}(\boldsymbol{r})$. Thus, the problem of N-electron system is converted into that of one electron system under the effective potential υ_{eff} without introducing any approximations. Equations (2.15), (2.16) and (2.18), are together called as the Kohn–Sham equation [55], which is the exact expression of the interacting many-electron systems.

2.1.4 Local density approximation

The local density approximation (LDA) is the simplest method describing the exchange-correlation energy E_{xc} [56, 57]. In this approximation, the electron density of the system is considered to be locally constant. Therefore the exchange-correlation energy is expressed as

$$E_{xc}[n(\boldsymbol{r})] = \int \varepsilon_{xc}[n(\boldsymbol{r})]n(\boldsymbol{r})d\boldsymbol{r}. \tag{2.19}$$

where ε_{xc} refers to the exchange-correlation energy of the homogeneous electrons gas with the electron density of $n(\boldsymbol{r})$. Then $\upsilon_{xc}[n(\boldsymbol{r})]$ is described as

$$\upsilon_{xc}(\boldsymbol{r}) = \frac{\delta E_{xc}[n(\boldsymbol{r})]}{\delta n[(\boldsymbol{r})]} = \frac{dn[(\boldsymbol{r})]\varepsilon_{xc}(n)n}{dn}|_{n=n(\boldsymbol{r})\pm\infty}. \tag{2.20}$$

The widely used ε_{xc} is the functional form obtained using the quantum Monte Carlo calculation on homogeneous electrons gas by Ceperley and Alder [57].

2.1.5 Generalized gradient approximation

The LDA is applicable for systems with slowly varying densities, since ε_{xc} is referred as the exchange-correlation energy of the homogeneous electron gas. However, when electron density possesses a strong inhomogeneity (*e.g.*, systems including transition metal elements), the LDA often causes a overestimation in the total or binding energy, leading to a underestimation of the bond length. To overcome this problem, generalized gradient approximation (GGA) method was developed [58, 59], in which the gradient correction on the electrons density is taken into account,

$$E_{xc}[n(\boldsymbol{r})] = \int f[n(\boldsymbol{r}), \nabla n(\boldsymbol{r})] d\boldsymbol{r}. \tag{2.21}$$

The GGA improves the accuracy of calculation results. Among several GGA functionals, in this thesis, we used the PBE functional proposed by Perdew, Burke, and Ernzerhof [58, 59].

2.1.6 Pseudopotential

Electrons in an atom or molecule are divides into valence and core electrons, depending on their distribution. The valence electrons in the outermost occupied shell dominantly affect the physical and chemical properties of materials, while the core electrons in inner shells are chemically inert and hardly contribute to the chemical bonds. Furthermore, the core electron wavefunction oscillates in the core region, so that a large amount of the plane wave basis set to expand are required in the DFT calculations, leading to large computational cost.

In this subsection, we will explain the pseudopotential approach to reduce the computational cost arising from the core electrons. Wave functions $|\psi_v\rangle$ and $|\psi_c\rangle$ are the exact solutions of the Schrödinger equation

$$\hat{H}|\psi_n\rangle = E|\psi_n\rangle \tag{2.22}$$

for valence electron ($n = v$) and core electrons ($n = c$), respectively. The valence wavefunction $|\psi_v\rangle$ can be written as the sum of a smooth pseudo wavefunction $|\phi_v\rangle$ and an oscillating function $\sum_c a_{cv}|\psi_v\rangle$, which is obtained from the orthogonalization of valence to the core orbitals

$$|\psi_v\rangle = |\phi_v\rangle + \sum_c a_{cv}|\psi_c\rangle, \tag{2.23}$$

where

$$a_{cv} = -\langle\psi_c|\phi_v\rangle. \tag{2.24}$$

By substituting this valence wavefunction $|\psi_v\rangle$ into Eq. (2.22),

$$\hat{H}|\phi_v\rangle = E_v|\phi_v\rangle + \sum_c (E_c - E_v)|\psi_c\rangle\langle\psi_c|\phi_v\rangle \tag{2.25}$$

is obtained, and it can be rewritten as

$$(\hat{T} + \hat{V}^{PP})|\phi_v\rangle = E_v|\phi_v\rangle, \tag{2.26}$$

$$\hat{V}^{PP} = \hat{V} - \sum_c (E_c - E_v)|\psi_c\rangle\langle\psi_c| \tag{2.27}$$

where $\hat{V}^{PP}$ is the pseudopotential and $\hat{V}$ is the true potenital.

In this thesis, we applied ultrasoft pseudopotential developed by Vanderbilt [60]. To get the screened potential $V^{AE}(r)$ and all-electron wavefunction $|\psi_i^{AE}\rangle$, an all-electron DFT calculation for a free atom is carried out by comparing with the reference configuration,

$$(\hat{T} + \hat{V}^{AE} - \epsilon_i)|\psi_i^{AE}\rangle = 0, \tag{2.28}$$

where i indicates quantum numbers n, l, and m. Then, we need to construct a psuedo wavefunction $|\phi_i\rangle$ and a local potential $V_{loc}^{PP}(r)$, which smoothly connect to $|\psi_i^{AE}\rangle$ and $V^{AE}(r)$, respectively. That is,

$$\phi_i(r) = \psi_i^{AE}(r) \quad (r \geq r_c), \tag{2.29}$$

$$V_{loc}^{PP}(r) = V^{AE}(r) \quad (r \geq r_c), \tag{2.30}$$

where r_c denotes the cutoff radius. To obtain the ultrasoft psedopotential by using the above $\phi_i(r)$ and $V_{loc}^{PP}(r)$, we define orbitals $|\chi_i\rangle$

$$|\chi_i\rangle = (\epsilon_i - \hat{T} - \hat{V}_{loc})|\phi_i\rangle. \tag{2.31}$$

Then, a matrix of inner products B_{ij} can be formed by

$$B_{ij} = \langle\phi_i|\chi_j\rangle. \tag{2.32}$$

We define another set of orbitals $|\beta_i\rangle$,

$$|\beta_i\rangle = \sum_j (B^{-1})_{ji}|\chi_j\rangle, \tag{2.33}$$

where j is a composite index as i. Then, we define deficit charge density $Q_{ij}(\boldsymbol{r})$

$$Q_{ij}(\boldsymbol{r}) = \int \left[\psi_i^{*AE}(\boldsymbol{r})\psi_j^{AE}(\boldsymbol{r}) - \phi_i^*(\boldsymbol{r})\phi_j(\boldsymbol{r})\right] d(\boldsymbol{r}). \tag{2.34}$$

Now, we construct matrix D_{ij} as

$$D_{ij} = B_{ij} + \epsilon_i Q_{ij}, \tag{2.35}$$

where $Q_{ij} = \int Q_{ij}(\boldsymbol{r})d\boldsymbol{r}$. Then, there is $|\phi_k\rangle$ satisfying the equation

$$\left(\hat{T} + \hat{V}_{loc}^{PP} + \sum_{ij} D_{ij}|\beta_i\rangle\langle\beta_j|\right)|\phi_k\rangle = \epsilon_k\left(1 + \sum_{ij} D_{ij}|\beta_i\rangle\langle\beta_j|\right)|\phi_k\rangle, \tag{2.36}$$

where k is a composite index as i or j. Finally, construct unscreening $V_{ion,loc}^{PP}(r)$ and $D_{ij}^{(0)}$ as

$$V_{ion,loc}^{PP}(\boldsymbol{r}) = V_{loc}^{PP}(\boldsymbol{r}) - V_{H}^{PP}(\boldsymbol{r}) - V_{xc}^{PP}(\boldsymbol{r}), \tag{2.37}$$

$$D_{ij}^{(0)} = D_{ij} - \int d\boldsymbol{r}V_{loc}^{PP}(\boldsymbol{r})Q_{ij}(\boldsymbol{r}), \tag{2.38}$$

where $V_{H}^{PP}(\boldsymbol{r})$ and $V_{xc}^{PP}(\boldsymbol{r})$ are the Hartree and exchange-correlation potential, respectively, calculated from the valence psuedo wavefunctions. The ultrasoft pseudopotential is expressed as

$$V_{ion}^{PP} = V_{ion,loc}^{PP}(r) + \sum_{i,j} |\beta_i\rangle D_{ij}^{(0)}\langle\beta_j|, \tag{2.39}$$

where the second term compensates the deficit charge density.

2.2 Effective screening medium method

Poisson's equation describes the relation between electron and the electrostatic potential. Poisson's equation deduced from the Kohn–Sham equation is solved by imposing a periodic boundary condition in the conventional DFT approach. However, this procedure may lead to unphysical results for the surfaces and 2D materials with polarity, because the dipole moment on surfaces or planes leads to singularity in electrostatic potential at the cell boundaries, causing unphysical electric field. To overcome this problem, Otani and Sugino developed the effective screening medium (ESM) method [61], in which the semi-infinite media with appropriate permittivity are introduced at the cell boundaries, to remove the singularity arising from such dipole between adjacent cells.

The total-energy functional of the system within the DFT is

$$E[n(\boldsymbol{r}), v(\boldsymbol{r})] = T_s[n(\boldsymbol{r})] + E_{xc}[n(\boldsymbol{r})] - \int d\boldsymbol{r}\frac{\epsilon(\boldsymbol{r})}{8\pi} \mid \nabla v(\boldsymbol{r}) \mid^2 + \int d\boldsymbol{r}n(\boldsymbol{r})v(\boldsymbol{r}), \tag{2.40}$$

where $n(\boldsymbol{r})$, $v(\boldsymbol{r})$, and $\epsilon(\boldsymbol{r})$ are the electron charge density, electrostatic potential, and relative permittivity of the effective medium at the cell boundary, respectively. By taking the variation of $E[n(\boldsymbol{r}),v(\boldsymbol{r})]$ with respect to $v(\boldsymbol{r})$, we get a generalized Poisson's equation

$$\nabla \cdot [\epsilon(\boldsymbol{r})\nabla]v(\boldsymbol{r}) = -4\pi n(\boldsymbol{r}). \tag{2.41}$$

By introducing the Green's function, the Poisson's equation turns into

$$\nabla \cdot [\epsilon(\boldsymbol{r})\nabla] G(\boldsymbol{r}, \boldsymbol{r'}) = -4\pi\delta(\boldsymbol{r} - \boldsymbol{r'}). \tag{2.42}$$

Then, electrostatic potential $\upsilon(\boldsymbol{r})$ is expressed as

$$\upsilon(\boldsymbol{r}) = \int d\boldsymbol{r'} G(\boldsymbol{r}, \boldsymbol{r'}) n_{tot}(\boldsymbol{r'}). \tag{2.43}$$

Here, we assume the relative permittivity $\epsilon(\boldsymbol{r})$ only depends on the z; hence the Poisson's equation

$$\{\partial_z[\epsilon(z)\partial_z] + \epsilon(z){\nabla_{\parallel}}^2\} G((\boldsymbol{r}_{\parallel} - \boldsymbol{r'}_{\parallel}), z, z') = -4\pi\delta((\boldsymbol{r}_{\parallel} - \boldsymbol{r'}_{\parallel})(z - z') \tag{2.44}$$

becomes

$$\{\partial_z[\epsilon(z)\partial_z] - \epsilon(z) g_{\parallel}^2\} G(\boldsymbol{g}_{\parallel}, z, z') = -4\pi\delta(z - z'), \tag{2.45}$$

where $\boldsymbol{g}_{\parallel}$ and $g_{\parallel}$ denote the wave vector parallel to the surface and its absolute value, respectively.

The ESM method can impose different boundary conditions on systems for different purposes. In this thesis, the following three boundary conditions are used to solve the Poisson's equation.

(1) The vaccum/vaccum boundary condition (open boundary condition) [Fig. 2.1(a)]

$$\partial_z \upsilon(\boldsymbol{g}_{\parallel}, z)\big|_{z=\pm\infty} = 0, \quad \epsilon(z) = 1;$$

(2) The metal/metal boundary condition [Fig. 2.1(b)]

$$\upsilon(\boldsymbol{g}_{\parallel}, \pm z_1) = 0, \quad \epsilon(z) = \begin{cases} 1 & \text{if } |z| \le z_1 \\ \infty & \text{if } |z| \ge z_1 \end{cases};$$

(3) The vacuum/metal boundary condition [Fig. 2.1(c)]

$$\begin{cases} \upsilon(\boldsymbol{g}_{\parallel}, z)\big|_{z=z_1} = 0 \\ \partial_z \upsilon(\boldsymbol{g}_{\parallel}, z)\big|_{z=-\infty} = 0 \end{cases}, \quad \epsilon(z) = \begin{cases} 1 & \text{if } |z| \le z_1 \\ \infty & \text{if } |z| \ge z_1 \end{cases}.$$

The first condition is adopted for the calculation on systems with dipole moment or polarity on the surfaces. The electrostatic potential may give a correct vacuum level at the boundary under this condition by introducing the semi-infinite media with relative permittivity of 1 describing the vacuum. The second condition describes the systems in which slabs or 2D materials are sandwiched by two parallel planar electrodes described by the effective medium with infinite permittivity situated at the cell boundaries normal to the z axis, so that an electric field is applied to the material sandwiched by these two electrodes. In the third condition, a planar electrode is located at one of two cell boundaries normal to the z axis described by the semi-infinite media with infinite permittivity, while an open boundary condition is imposed on the other boundary by using a relative permittivity of 1, allowing us to inject carriers into the material by using this metal electrode.

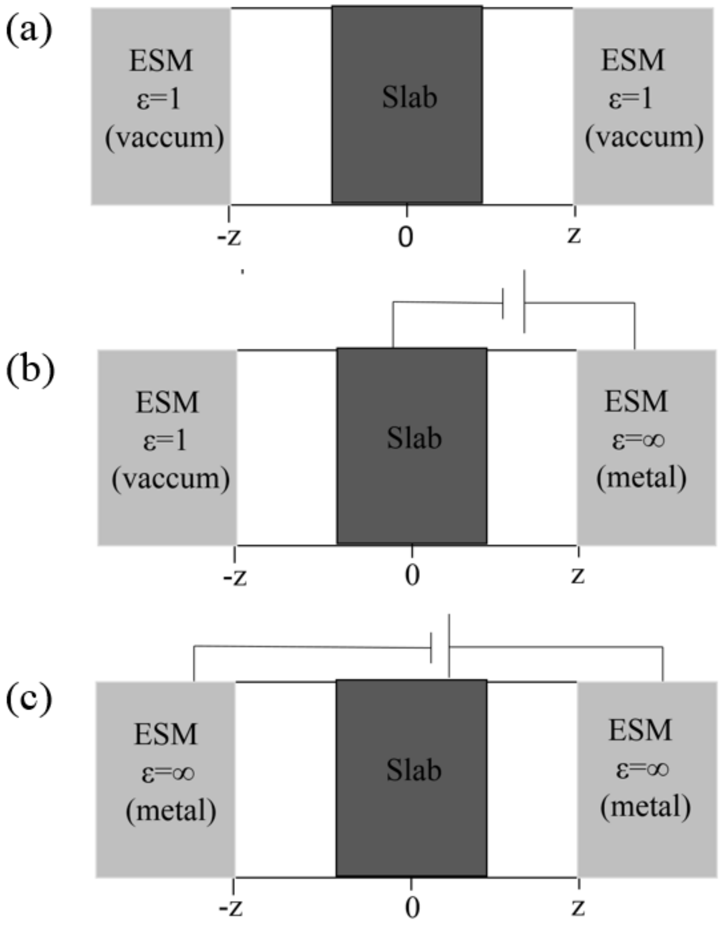

Figure 2.1: Calculation models with different boundary conditions in this thesis using the DFT combined with the ESM method.

Chapter 3

Geometric and electronic properties of h-GaN

In this chapter, we investigate the detailed geometric and electronic properties of a sheet consisting of hexagonally arranged Ga and N atoms (h-GaN) under the biaxial compression, surface hydrogenation, and external electric field, using first-principles total-energy calculations within the framework of the DFT combined with the ESM method. In addition, we investigate the energetics and electronic structure of the h-GaN thin film and van der Waals heterostructures with other 2D materials (graphene or monolayer h-BN), using the DFT with the van der Waals correction and the ESM method.

3.1 Introduction

2D materials with atom thickness exhibit peculiar electronic properties arising from their dimensionality and atomic network topology. Because of the bipartite structure of a honeycomb network of carbon atoms, graphene possesses pairs of linear dispersion bands at the K and K' points, leading to the vanishing density of states at the E_F. In accordance with the linear dispersion bands, graphene possesses extremely high carrier mobility, which allows it to be an emerging material for future electronic, spintronic, optoelectronic, and sensing devices [1, 6, 10]. Analogous to graphene, other group IV elements, such as silicon and germanium, also form a honeycomb network with structural buckling on appropriate supporting substrates; these structures are known as silicene and germanene, respectively. Despite the structural buckling, free-standing silicene and germanene still maintain similar linear dispersion bands at the E_F [62, 63]. In addition to the honeycomb networks of group IV elements, combination of group III and V elements can form a similar honeycomb network with atom thickness because they have the same valence in the primitive cell as graphene. Hexagonal boron nitride (h-BN), consisting of boron and nitrogen which are adjacent to carbon in the periodic table, preserves a planar hexagonal network similar to graphene. Although there are structural similarities between monolayer h-BN and graphene, the monolayer h-BN is an insulator with a large band gap of approximately 5 eV because of the electronegativity difference in the constituent elements [64, 65, 66].

The preceding considerations have stimulated our enthusiasm to explore further variations in 2D materials of III-V compounds. Among the wide variety of possible combinations, GaN is a fascinating candidate for 2D planar materials of III-V compounds, contributing to modern technology as an emerging material. Group III nitride semiconductors with a wurtzite structure, such as GaN and its derivatives, have attracted much attention because of their excellent optical and electrical properties for applications as optical and high-frequency electronic devices because of their high carrier mobility and wide direct band gap [67, 68, 69, 70, 71]. For example, InGaN-based quantum well structures have enabled high-performance light-emitting diodes and laser diodes covering from violet to green wavelength regions [72]. Furthermore, high-density 2D electron gas at the interfaces in AlGaN/GaN heterostructures allows them to be promising materials for high-electron mobility transistors with high voltage and low resistivity [73]. In accordance with the technological demand, it is natural to consider the possibility of 2D layered structures of GaN and its derivatives. Şahin *et al.* have conducted systematic first-principle total-energy calculations on the monolayer honeycomb structures of group-IV elementary materials and III-IV compounds and predicted that monolayer GaN can have a planar structure [74, 75]. Nevertheless, comprehensive and detailed information about the layered structures of GaN is still absent in the literature and will certainly advance the device technology associated with III-V compounds.

All calculations in this study were performed based on the DFT implemented in the Simulation Tool for Atom TEchnology (STATE) code [54, 55, 76]. The generalized gradient approximation with the Perdew-Burke-Ernzerhof functional was used to treat the exchange-correlation potential among interacting electrons [58, 59], and the interaction between electrons and ions was described by ultrasoft pseudopotentials according to the Vanderbilt scheme [60]. The valence wavefunctions and charge density were expanded in terms of a plane wave basis set with cutoff energies of 25 and 225 Ry, respectively. Structural optimizations were continued until the force on each atom was less than 1.33×10^{-3} HR/a.u. Integration over Brillouin zones was carried out using an equidistance mesh of $4 \times 4 \times 1$ k-points, which give sufficient convergence in the total energy and electronic structure of GaN with the hexagonal and wurtzite structures. We used the ESM method to impose an open boundary condition in the direction normal to the 2D sheets, allowing us to simulate the polar nature of GaN under periodic boundary conditions [61]. The cell boundary is located above and below the GaN sheet by 4 Å vacuum spacing. In addition, to investigate the geometric and electronic structures of h-GaN under an

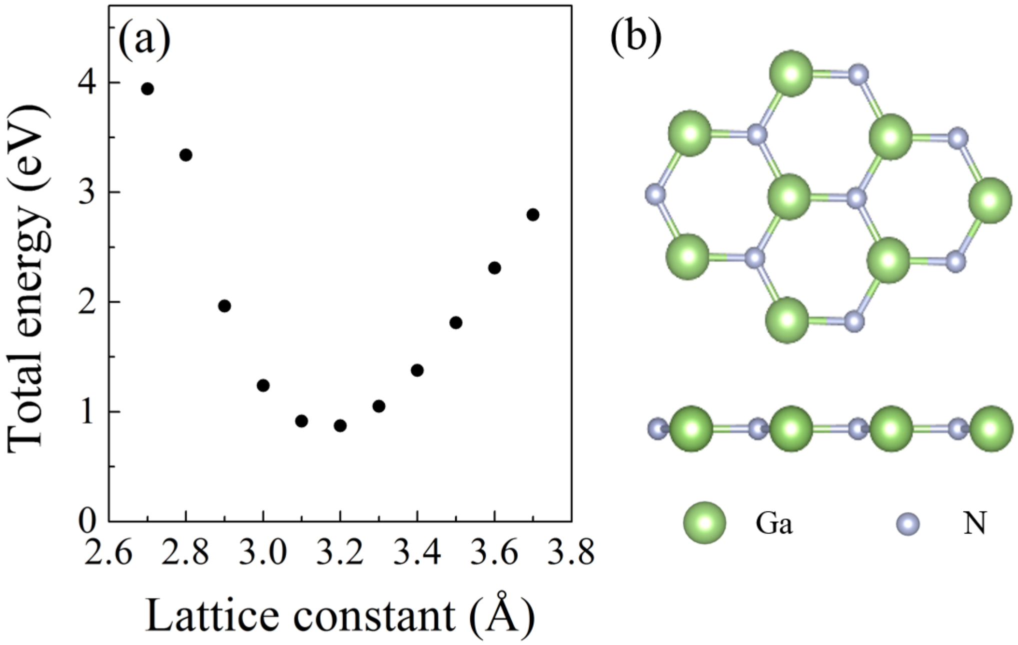

Figure 3.1: (a) Total energies of monolayer h-GaN as a function of the lattice constant; energies are measured from that of bulk GaN with a wurtzite structure. (b) The geometric structure of monolayer h-GaN under the optimum lattice constant.

electric field, we applied an external electric field normal to the sheet between the two planar electrodes, simulated by the effective screening medium with infinite permittivity, arranged parallel to the cell boundaries [61]. For the GaN thin films and van der Waals heterostructures, we considered the van der Waals interaction by treating vdW-DF2 with the C09 exchange-correlation functional to describe the weak dispersive interaction between atomic layer materials [77, 78, 79].

3.2 Energetics and electronic structures of monolayer h-GaN

Figure 3.1(a) shows the total energy of monolayer h-GaN as a function of the lattice constant. We can see that the equilibrium lattice constant of monolayer h-GaN is 3.2 Å, which is very close to that of bulk GaN with the wurtzite structure, while the total energy is higher than that of the bulk GaN by 0.87 eV per pair of GaN. Figure 3.1(b) shows the optimized structure of the monolayer h-GaN under the equilibrium lattice constant; it has a planar hexagonal network consisting of alternating Ga and N atoms, similar to that of h-BN. The optimized bond length of GaN is 1.85 Å, which is small enough to maintain its planar hexagonal structure because of the substantial interaction between the p_z states of Ga and N atoms, although the bond length is longer than that of graphene (1.42 Å) and h-BN (1.44 Å). By carefully checking the other possible structures under the equilibrium lattice constant,

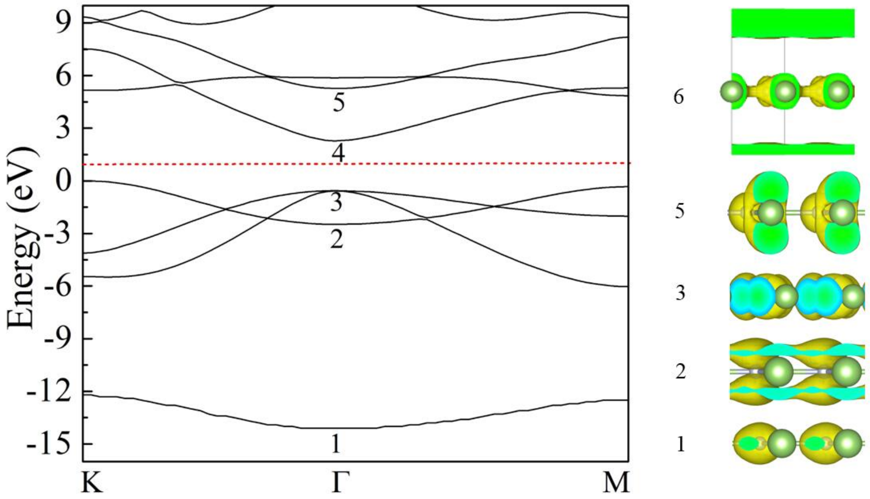

Figure 3.2: Band structure and squared wavefunctions at the Γ point of monolayer h-GaN. Energies are measured from that of the valence band top. Band indexes correspond to those of squared wavefunctions.

h-GaN does not possess a buckled structure as in the case of the atomic layers in bulk GaN with a wurtzite structure, so that the planar structure is confirmed as the ground state conformation of monolayer h-GaN.

Figure 3.2 presents the electronic structure of h-GaN under the equilibrium lattice constant. The h-GaN sheet with the planar conformation is a semiconductor with an indirect energy band gap of 2.28 eV between the K and Γ points for the valance band top and conduction band bottom, respectively. This makes monolayer h-GaN distinct from the bulk GaN with the wurtzite structure, which has a direct band gap of 2.89 eV at the Γ point [80]. The calculated effective masses for the electron and hole are 0.96 and 0.51 m_e, respectively, which are heavier than those of the bulk GaN, where m_e is the bare electron mass. Furthermore, the electronic band structure of h-GaN is different from that of h-BN, which is another planar III-V compound. The squared wavefunctions at the Γ point for all valence bands and the lowest two branches of the conduction band are also shown in Fig. 3.2. The lowest and the doubly degenerated highest valence states at the Γ point are primarily distributed on N atoms with $2s$ and $2p_{x+y}$ characteristics, respectively. The second lowest state, which corresponds to the valence band top at the K point, is the $2p_z$ state of N atoms. In contrast, by focusing on the conduction band, we find different characteristics for the wavefunctions: the lowest unoccupied state is mostly contributed by the $4p_z$ state of Ga atoms, with the $2s$ state of N atoms. The second lowest unoccupied state exhibits different characteristics. The state is distributed not only at the atomic sites but also in the vacuum region where atoms are absent, indicating a nearly free electron state nature that is inherent in layered materials such as graphene and h-BN [81, 82, 83, 84, 85, 86]. Thus, multilayered h-GaN may exhibit metallic properties similar to graphite intercalation compounds by injecting electrons into this state [87, 88].

3.3 Mechanical properties of monolayer h-GaN

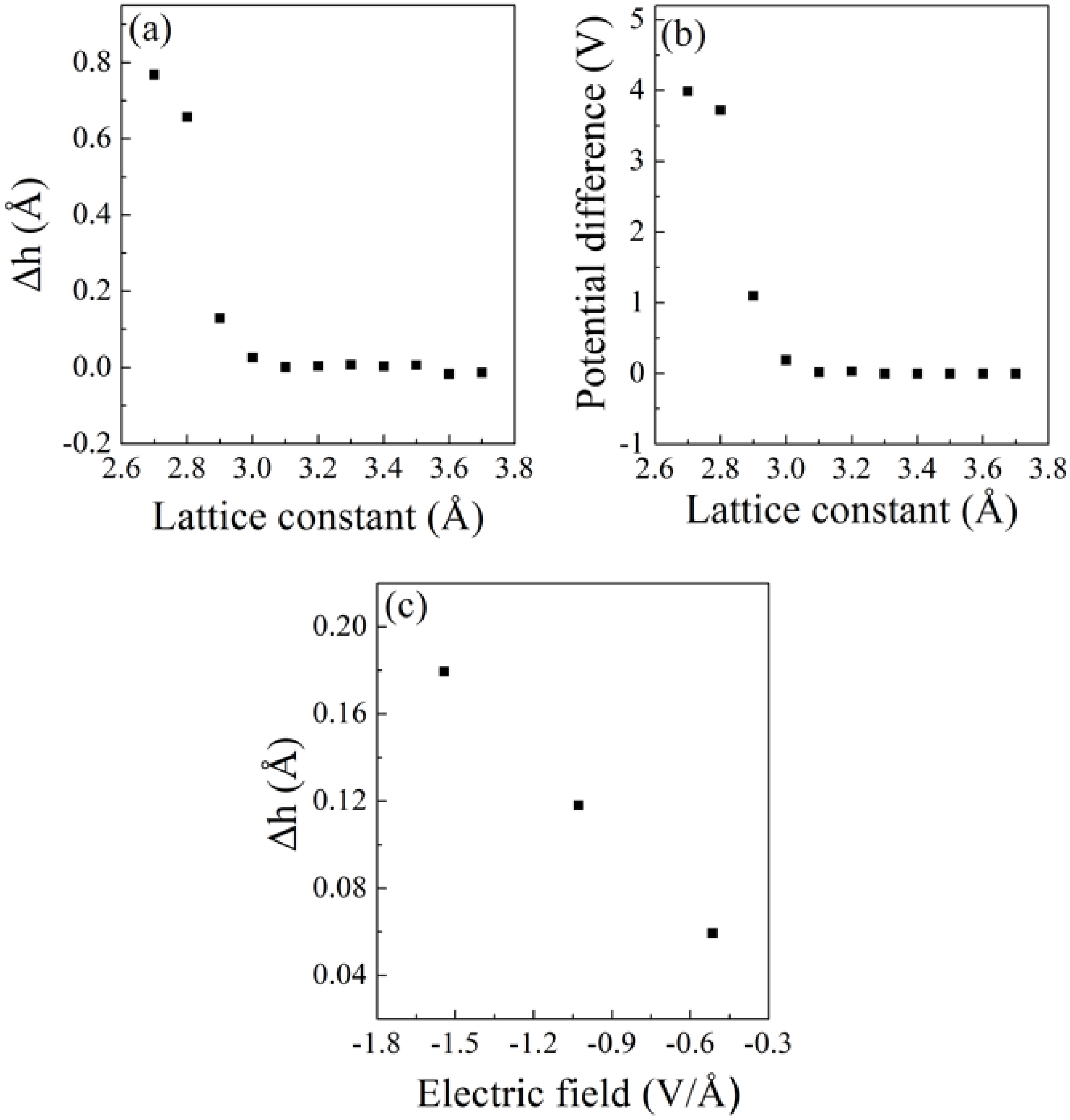

Figure 3.3: (a) Buckling height and (b) electrostatic potential difference in monolayer h-GaN as a function of the lattice constant. (c) Buckling height of monolayer h-GaN under an external electric field.

Because strain can effectively tune the physical properties of a material, we studied the strain effects on the geometric and electronic structure of monolayer h-GaN. Figures 3.3(a) and 3.3(b) show the buckling height and electrostatic potential difference between N and Ga surfaces under biaxial compression, respectively. The buckling height is defined as the longitudinal distance between N and Ga atoms

Table 3.1: Band gap of compressed h-GaN sheet with different lattice constant.

a (Å)	3.2	3.1	3.0	2.9	2.8
E_g (eV)	2.28	2.73	3.05	2.92	0
Gap	indirect	indirect	indirect	direct	metal

under compression. The lateral biaxial compression causes structural buckling on the h-GaN sheet, whose height rapidly increases with decreasing lattice parameter. Under the biaxial compressive strain of 5% or larger corresponding to $a = 3.0$ Å, the h-GaN sheet prefers the buckled structure, of which height depends on the compressive strain, rather than the planar conformation. With structural buckling under the biaxial compression, polarization normal to the sheet occurs, inducing an internal electric field in the buckled GaN sheet. The polarization induced by the lateral compressive strain implies that h-GaN with the planar conformation undergoes a structural phase transition into the buckled conformation under an external electric field normal to the sheet. Figure 3.3(c) shows the buckling height as a function of the external electric field. The buckling height is found to monotonically increase with increasing field intensity, reaching 0.18 Å when the electric field is -1.54 V/Å. In the buckled structure under the electric field, Ga atoms are shifted to negative electrode while the N atoms are shifted to positive electrode. Thus, the h-GaN sheet exhibits piezoelectricity and inverse piezoelectricity, being applicable to piezoelectric devices with atom thickness.

The biaxial compressive strain modulates the electronic structure of the h-GaN sheet. The calculated electronic properties of the compressed h-GaN sheet are summarized in Table 3.1. The electronic structure of compressed h-GaN is sensitive to the lateral lattice constant. With decreasing lattice constant, first, the band gap gradually increases, retaining its indirect band gap nature. With a lattice constant of $a = 2.9$ Å, the sheet is a semiconductor, with a direct gap of 2.92 eV at the Γ point. Then, by further decreasing the lattice constant, suddenly, the sheet undergoes a phase transition into a metallic phase in which the valance and the conduction bands touch each other at the Γ point. This fact indicates that h-GaN under biaxial strain may be applicable as a constituent material of ultrathin optoelectronic, optical, and photovoltaic devices because of its tunable direct band gap.

3.4 Polarity of monolayer h-GaN

Although the h-GaN sheet with the buckled conformation exhibits interesting electronic properties, unsaturated $2p$ and $4p$ states of N and Ga atoms, respectively, cause structural instability without external constraints. To stabilize the h-GaN

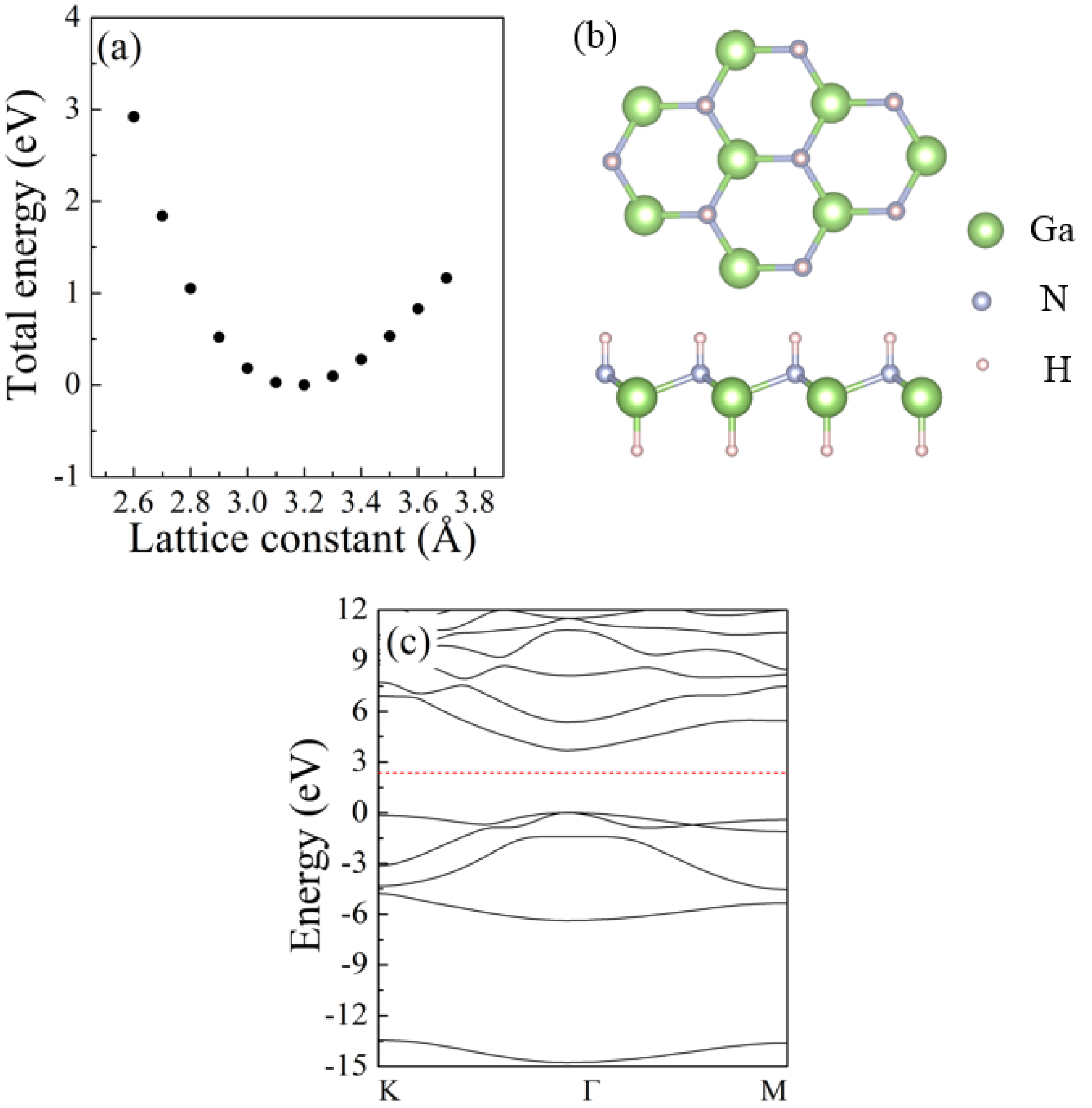

Figure 3.4: (a) Total energies of hydrogenated h-GaN sheet as a function of the lattice constant. (b) Geometric and (c) electronic structures of the fully optimized h-GaN with a hydrogenated surface.

with the buckled conformation, here, we consider h-GaN with the buckled conformation in which an H atom is attached to each Ga/N atom to saturate their p states. The optimal lattice constant of fully hydrogenated h-GaN with buckled conformation is 3.2 Å, which is the same as that of the h-GaN sheet with the planar conformation [Fig 3.4(a)]. Under the optimized structure, the sheet shows structural buckling with a height of 0.69 Å [Fig. 3.4(b)]. Figure 3.4(c) shows the calculated energy band structure of the fully hydrogenated h-GaN. The sheet is a semiconductor with a direct band gap of 3.68 eV at the Γ point, which is wider than those of the sheet with the planar conformation and of bulk GaN with a wurtzite structure.

In addition to the substantial stabilization of h-GaN in the buckled conforma-

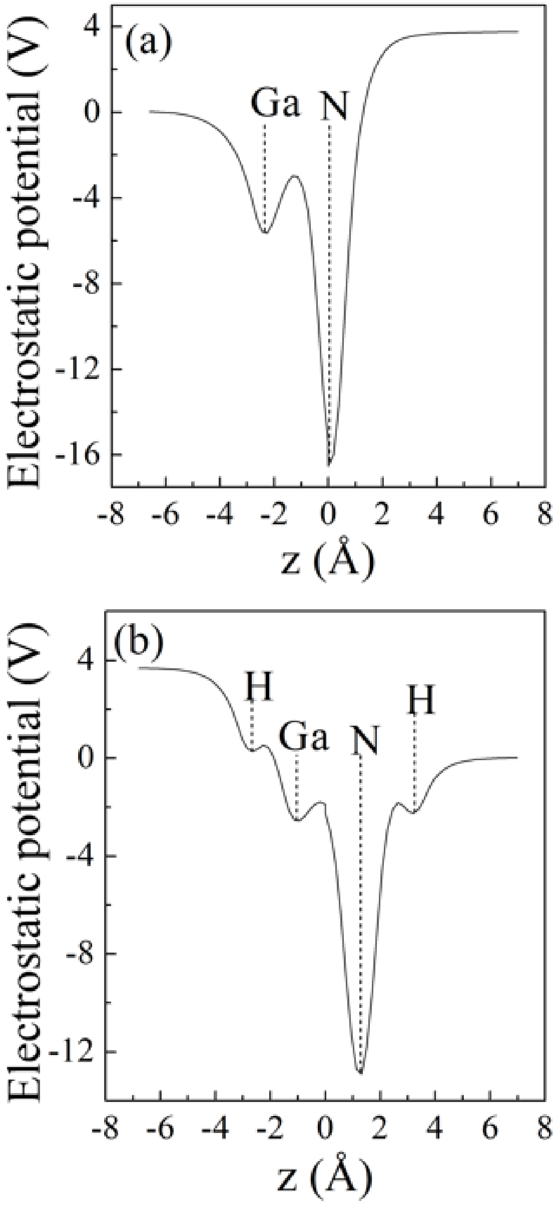

Figure 3.5: Plane-averaged electrostatic potential of h-GaN sheet with (a) clean and (b) hydrogenated surfaces.

tion, hydrogenation of buckled h-GaN sheets causes a polarity inversion. Figure 3.5 shows the plane-averaged electrostatic potential of h-GaN with clean and hydrogenated surfaces normal to the layer. For the buckled sheet with clean surfaces, the electrostatic potential just outside the N surface is higher than that outside the Ga, in accordance with the electric field induced by the compressive strain. In contrast, the potential difference between the N and Ga surfaces of the hydrogenated h-GaN sheet is opposite to that of the buckled sheet with clean surfaces. Thus, surface hydrogenation can tune the polarity of h-GaN with the buckled conformation. The inversion of polarity with hydrogenation is induced by positively and negatively charged H atoms attached to N and Ga atoms, respectively: to saturate the p_z states of surface N and Ga atoms, pseudoatoms with valence electrons of 0.75e and 1.25e are necessary, respectively [89]. Therefore, the neutral H atoms on the surface induce excess and deficit electrons on the N and Ga surfaces, respectively, resulting in polarity opposite to that of the sheet with clean surfaces. It is also expected that chlorination and fluorination of h-GaN lead to different electrostatic potentials and polarities [90].

3.5 Energetics and electronic structures of h-GaN thin films

Then, we investigate the energetics of multi-layer h-GaN by using the DFT with the van der Waals correction and ESM method. Here, we consider the multi-layer h-GaN with the AA' stacking arrangement as the energetically favorable arrangement of h-GaN [75, 91]. We evaluate the interlayer binding energy per pair of Ga and N in n-layered h-GaN ($n = 2 \sim 8$ and ∞), E_I, defined as follows,

$$E_I = \frac{1}{n}(E_n - nE_{mono}), \tag{3.1}$$

where E_n and E_{mono} are the total energies of the n-layered h-GaN and the monolayer h-GaN. Table 3.2 shows the optimum interlayer spacing d_{opt} and interlayer binding energy E_I of these multi-layer h-GaN. The equilibrium interlayer spacing d_{opt} of bilayer and infinite-layer h-GaN systems is approximately 2.2 Å, which is considerably smaller than the optimum spacing of graphite and h-BN [92]. For other multi-layered h-GaN, the optimum interlayer spacing is slightly larger than those for the bilayer and bulk cases whose values are summarized in Table 3.2. This small interlayer spacing also leads to their large interlayer binding energies. These values imply that h-GaN layers are bound each other via not only the van der Waals interaction but also the ionic interaction between h-GaN layers. The small interlayer distance implies the possibility of further structural relaxation from the layered structure to three-dimensional network structures by forming interlayer bonds.

Figure 3.6 shows the electronic structures of multi-layer h-GaN under the equilibrium interlayer spacing. Although, the monolayer h-GaN is a semiconductor with

Table 3.2: Optimum interlayer distance and the corresponding interlayer binding energy per pair Ga and N of n-layered h-GaN ($n = 2 \sim 8$ and ∞)

n	2	3	4	5	6	7	8	∞
d_{opt} (Å)	2.22	2.25	2.26	2.28	2.28	2.29	2.28	2.21
E_I (eV/Å)	-1.175	-1.290	-1.354	-1.390	-1.407	-1.431	-1.436	-1.540

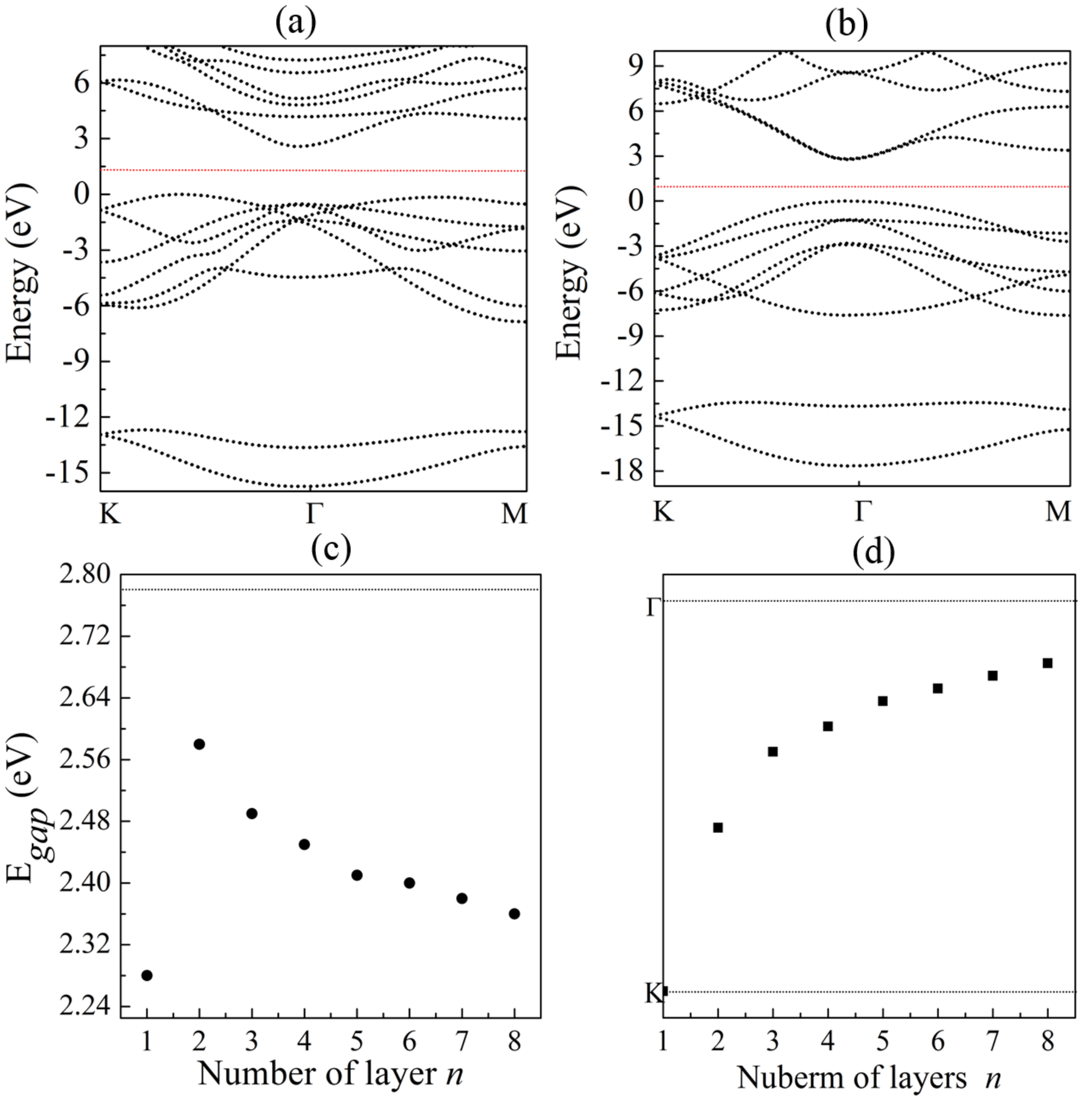

Figure 3.6: Band structures of (a) bilayer h-GaN and (b) bulk h-GaN. Energies are measured from that of the valence band top. The dotted horizontal line denotes the E_F. (c) Band gap value of h-GaN thin films as a function of the number of layers. The dashed horizontal line indicates the band gap value of bulk h-GaN. (d) The k position of the valence band top of h-GaN thin films as a function of the number of layers.

an indirect band gap between the K and Γ points for the valence and conduction band edges, respectively, the multi-layer h-GaN systems show different features: a bilayer h-GaN is also an indirect band gap semiconductor, in which the conduction band bottom (CBB) is located at the Γ point, while the valence band top (VBT) is dislodged from the K point in contrast to the case of monolayer h-GaN. We further found that the $\boldsymbol{k}$ position of the VBT of multi-layer h-GaN gradually approaches the Γ point with increasing the number of layers. In addition to the modulation of the valence band edge, the band gap of the multi-layer h-GaN is sensitive to the number of layers. The band gap of the bilayer h-GaN ($E_g = 2.58$ eV) is wider than that of the monolayer h-GaN ($E_g = 2.28$ eV). In contrast, the calculated band gap of the multi-layer h-GaN monotonically decreases with increasing the number of layers. Note that the bulk h-GaN has a direct band gap of 2.78 eV. The electronic structure modulation is ascribed to the fact that the wavefunction of the VBT of the monolayer h-GaN has a $2p_z$ character of N atoms. Thus, the state substantially shifts downward by the interlayer interaction owing to the small interlayer spacing.

3.6 Energetics and electronic structures of van der Waals heterostructures of h-GaN

Since the interlayer interaction between h-GaN layers substantially modulates the electronic structure of h-GaN in multi-layered structures as in the cases of multi-layer TMDCs, it is worth to investigate whether the electronic structure of h-GaN sheet is also modulated by forming the hybrid structure with the graphene or monolayer

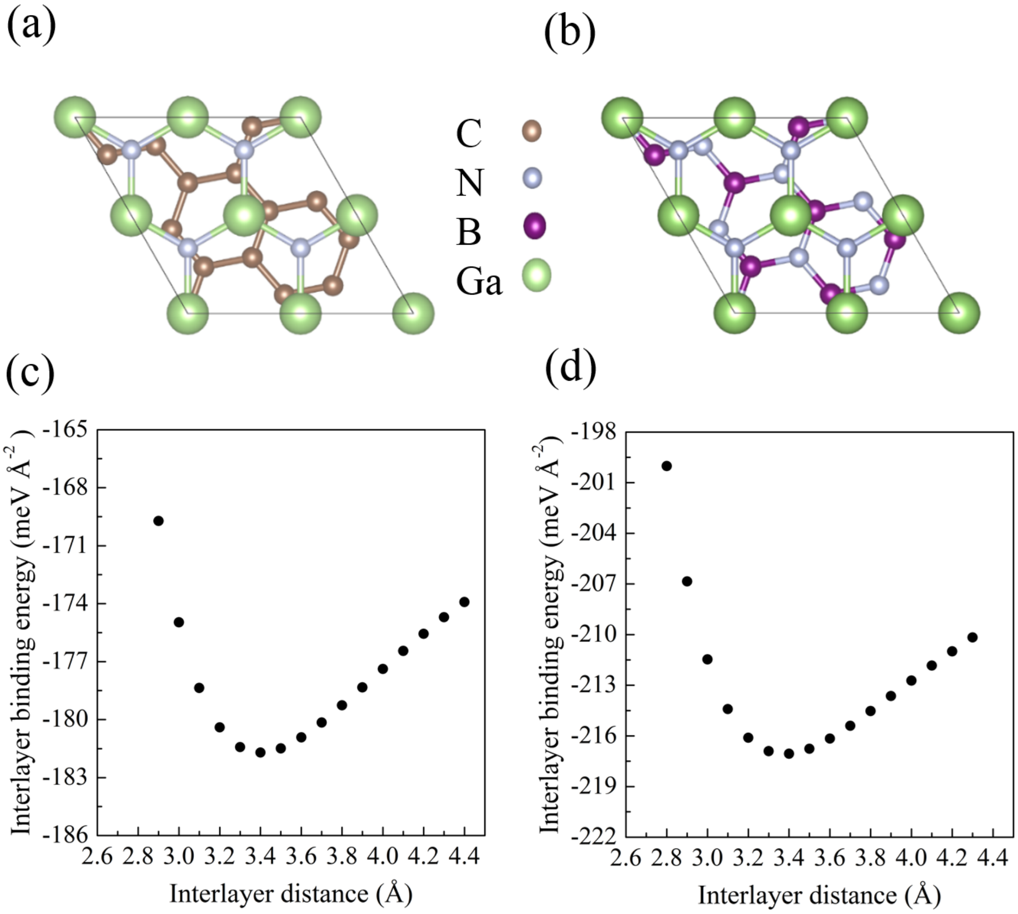

Figure 3.7: Geometric structures of (a) h-GaN/graphene and (b) h-GaN/h-BN. (c) Interlayer binding energies per unit area of (c) h-GaN/graphene and (d) h-GaN/h-BN as a function of interlayer spacing.

h-BN. To impose the commensurability condition between the lateral unit cells of h-GaN and graphene (or h-BN), we apply a supercell consisting of 2×2 unit cell of h-GaN containing four pairs of Ga and N atoms, and $\sqrt{7} \times \sqrt{7}$ unit cell of graphene (or h-BN) with 14 C atoms (or seven pairs of N and B atoms). With the choice of the supercell, the lattice mismatch between h-GaN and graphene (or h-BN) is less than 1.6%. To determine the stable structures of the hybrid systems, we calculate the interlayer binding energy per unit area, E_I, obtained by

$$E_I = \frac{1}{S'}[E_{hybrid} - (E_{mono} + E_X)], \tag{3.2}$$

where E_X is the total energy of an isolated layer of graphene or h-BN, E_{hybrid} is the total energy of the hybrid system, and S' is the interface area between h-GaN and graphene or h-BN. Figure 3.7 shows the geometric structures and the interlayer binding energies per unit area of h-GaN/graphene and h-GaN/h-BN as a function of the interlayer spacing. The optimum interlayer spacing for both systems is 3.4 Å, which is larger than that of multi-layer h-GaN. Furthermore, the value is similar to the interlayer spacing of h-BN and graphite [88, 92]. Under the optimum spacing, the interlayer binding energies of h-GaN/graphene and h-GaN/h-BN are 181 and 217 eV/Å^2, respectively, which are smaller than that of bilayer h-GaN. On the other hand, the value is still larger than that of the graphene and h-BN. Furthermore, the interlayer binding energy of the h-GaN/h-BN is larger than that of h-GaN/graphene. The fact indicates that the ionicity of the sheet affects the interlayer binding energy together with the van der Waals interaction.

Due to the weak van der Waals interaction, the electronic structures of h-GaN/graphene and h-GaN/h-BN heterostructures may be obtained by superposing the electronic structure of each constituent. Figure 3.8(a) presents the band structure of the h-GaN/graphene. We find that the h-GaN/graphene retains the characteristic electronic structure which is described by the electronic structure of each constituent unit near the E_F: the VBT and CBB states of graphene touch each other at the K point with a linear dispersion, and the h-GaN has an energy gap between the K and Γ points as the case of an isolated sheet. Figure 3.8(b) shows the squared wavefunctions at the K and Γ points around the E_F of h-GaN/graphene: the VBT and CBB states at the K point are p_z state of C atoms in graphene, while the second highest valence band at the K point and the lowest conduction band at the Γ point are distributed on h-GaN, retaining their distribution as in the isolated h-GaN sheet. Figures 3.8(c) and 3.8(d) show the electronic band structure and squared wavefunctions of h-GaN/h-BN, respectively. We find that h-GaN/h-BN is a semiconductor with an indirect band gap of 2.11 eV between the K and Γ points for the VBT and CBB, respectively, which is slightly smaller than the value of 2.28 eV of monolayer h-GaN. Meanwhile, the VBT state corresponds to the $2p_z$ state of N atoms, and the CBB state is originated from the $4p_z$ state of Ga atoms and the $2s$ state of N atoms, which is the same as the situation in the isolated monolayer h-GaN.

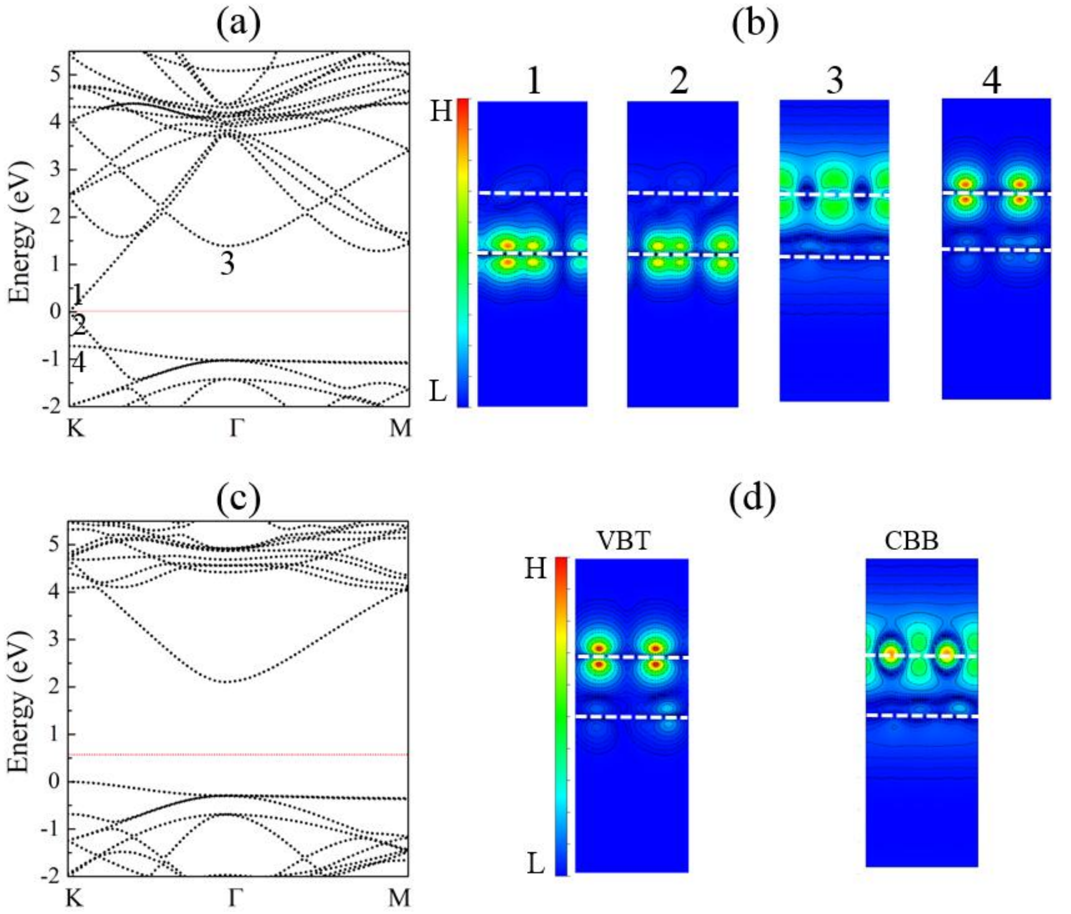

Figure 3.8: (a) Band structure and (b) squared wavefunctions of h-GaN/graphene. The numbers labeled for the energy band correspond to those for wavefunctions. (c) Band structure and (d) squared wavefunctions of the CBB and VBT states of h-GaN/h-BN. Energies are measured from that of the valence band top. The dotted horizontal line in the band structures denotes the E_F. In contour plot, the horizontal dotted lines denote the atomic layer positions of h-GaN, h-BN, and graphene. Adjacent contour lines represent the squared wavefunction amplitude with a difference of one order of magnitude.

3.7 Possible synthesis pathway of monolayer h-GaN

GaN intrinsically possesses a wurtzite structure as its ground state conformation rather than the stacked and layered structure of h-GaN sheets mentioned above. To investigate the possible pathway for synthesizing the layered structure of h-GaN sheets from the wurtzite-GaN thin film, we check the stability of wurtzite-GaN thin films with (0001)/$(000\bar{1})$ surfaces in terms of the number of atomic layers. We find that the wurtzite-GaN thin films with five or more atomic layers retain their wurtzite structure. In contrast, for the thin films with four or less atomic layers, the wurtzite structure spontaneously undergoes a structural phase transition into the layered structure of h-GaN sheets. This result indicates that wurtzite-GaN thin films with (0001)/(000$\bar{1}$) surfaces are the plausible starting material for the synthesis of the layered structure of h-GaN sheets by adopting the layer-by-layer peeling technique on wurtzite-GaN surfaces.

Our calculation showed that the planar monolayer h-GaN turns into the buckled structure under a lateral compressive strain. The fact gives another idea to synthesize the stacked structure of h-GaN sheets. Wurtzite-GaN thin films with

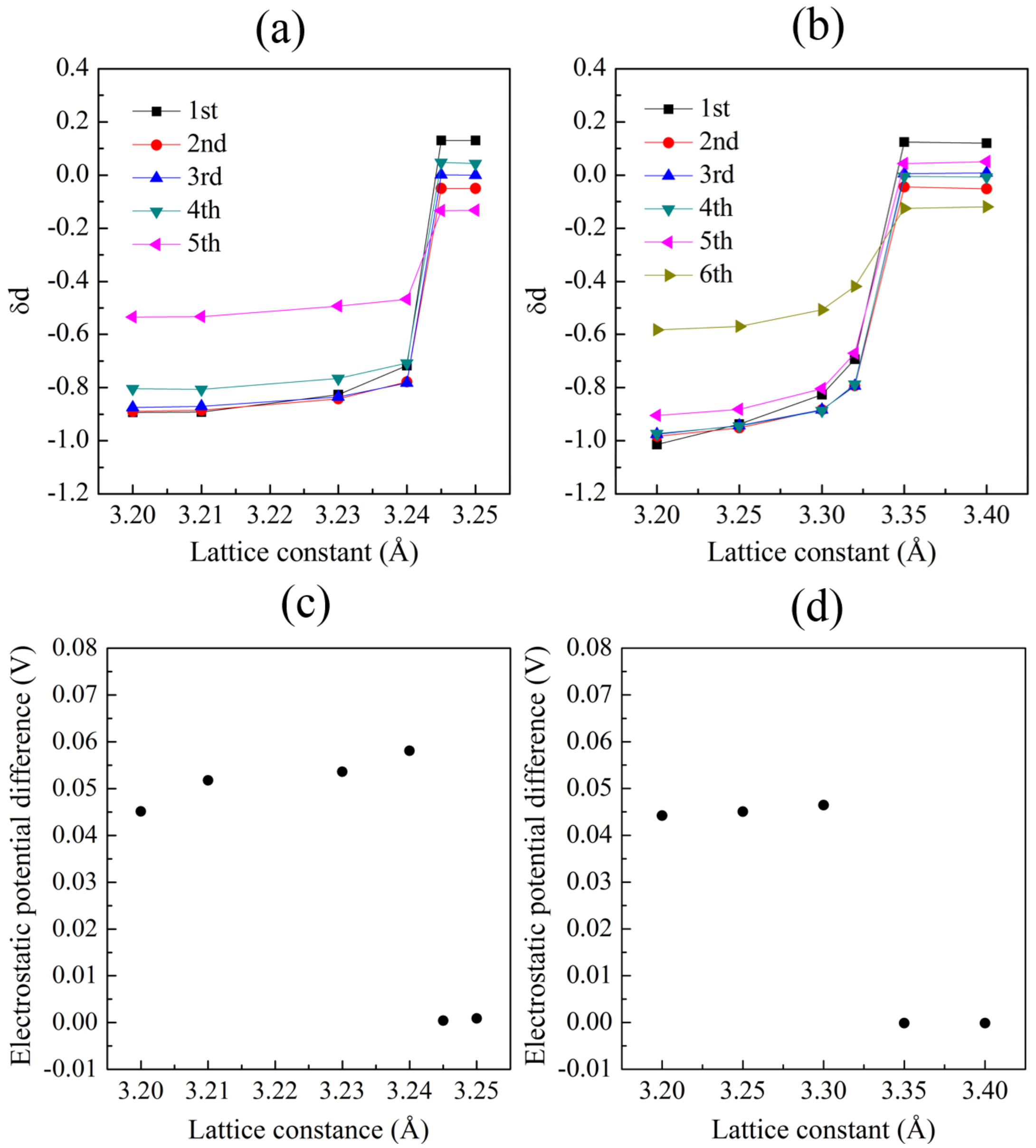

Figure 3.9: Buckled height in each atomic layer of wurtzite-GaN thin films with (a) five and (b) six atomic layers as a function of the biaxial tensile strain. The averaged-electrostatic potential difference between the N and Ga surfaces of wurtzite-GaN thin films with (c) five and (d) six atomic layers as a function of the biaxial tensile strain.

$(0001)/(000\bar{1})$ surfaces may undergo the structural phase transition to the planar stacking configuration under a biaxial tensile strain. Figures 3.9(a) and 3.9(b) show the buckling height of each atomic layer in the wurtzite-GaN thin films with five and six atomic layers as a function of the lateral lattice constant, respectively. The buckling height is defined as the longitudinal distance between N and Ga atoms in each atomic layer. In the buckling structure, N and Ga are separated in the direction normal to the layer in each atomic layer, so that N and Ga atoms are on (0001) and $(000\bar{1})$ surfaces, respectively. In both cases, atomic layers gradually flatten with increasing the tensile strain, then each atomic layer possesses the perfectly planar conformation rather than the buckled conformation above the critical tensile strain corresponding to the lattice constant of 3.25 and 3.35 Å for thin films with five and six atomic layers, respectively. According to the structural reconstruction induced by the tensile strain, the polarity of the GaN thin film also suddenly vanishes at the critical tensile strain as shown in Figs. 3.9(c) and 3.9(d) for thin films with five and six atomic layers, respectively.

3.8 Conclusion

We studied the geometric and electronic structures of hexagonally bonded GaN sheets under the biaxial compressive strain based on first-principles total-energy calculation within the framework of the DFT and ESM. Our calculations showed that the electronic properties of h-GaN are sensitive to the biaxial compression. The biaxial compressive strain causes structural buckling on h-GaN, which leads to the modulation of the electronic energy band around the gap: h-GaN with the planar conformation is an indirect gap semiconductor, while that with the buckled conformation may be a direct gap semiconductor. The structural buckling causes polarization normal to the sheet because of the electronegativity difference between Ga and N atoms. Furthermore, an external electric field normal to the sheet causes the structural modulation of h-GaN from planar to buckled conformations to compensate the external electric field by the polarization. By attaching H atoms onto all Ga and N atoms, h-GaN preserves the buckled structure, in which the polarity of the sheet is opposite to that of the buckled h-GaN with clean surfaces. These facts imply that h-GaN can be applicable for optoelectronic and piezoelectric devices under the biaxial strain.

We also studied the geometric and electronic properties of GaN thin films consisting of 2D atomic layers of h-GaN using the DFT containing van der Waals dispersive interaction combined with the ESM method. Our calculations showed that the interlayer interaction in the thin films of h-GaN is stronger by a magnitude than that in the conventional van der Waals materials such as graphite, indicating that the h-GaN layers are tightly bound each other in their thin film structures. According to the strong interlayer interaction, electronic structures of thin films of h-GaN are sensitive to the number of constituent layers: the gap monotonically decreases with increasing the number of layers. We further investigated the energetics and electronic structures of a monolayer h-GaN adsorbed on graphene and monolayer h-BN. The optimum interlayer spacing of both systems is 3.4 Å irrespective to the substrate species, which is larger than that of multi-layer h-GaN. Due to the weak van der Waals interaction, we find that h-GaN/graphene and h-GaN/h-BN heterostructures preserve the electronic structures of constituent monolayers. We also found that GaN thin films with the wurtzite structure undergo the structural transition into h-GaN thin films by applying the biaxial tensile strain.

Chapter 4

Electrostatic potential properties of graphene edges

In this chapter, we investigate the electrostatic potential properties of graphene edges in terms of their shapes and functional groups under the external electric field to provide theoretical insights into the field emission mechanism of graphene, using the DFT combined with the ESM method.

4.1 Introduction

Graphene is a single layer of graphite with an atom thickness and a honeycomb network of sp^2 C atoms [10]. Tightly bonded σ electrons within the atomic layer endow graphene with remarkable structural stability and mechanical stiffness. Moreover, π electrons distributed normal to the hexagonal covalent network cause pairs of linear dispersion bands around the six corners of the hexagonal Brillouin zone and the E_F, leading to a high carrier mobility up to $200,000$ cm^2/(V·s) [2, 3, 4]. These remarkable properties make graphene a unique material for examining unusual physical phenomena arising from low-dimensionality [1, 6] and for applying in thermal, thermoelectric, and electronic devices [93]. It has also been established that these remarkable properties are sensitive to atomic defects [94, 95, 96, 97], edges [21, 22, 98, 99], and hybrid structures with foreign materials [100, 101, 102, 103, 104, 105, 106, 107, 108], which are inherent in the experimental situations.

Edges are the typical structural imperfections in the graphene network that cause the substantial modulation of the electronic structure. In experimental situations, graphene may have versatile edges with different shapes and functional groups [109, 110, 111]. Such edge variation modulates the characteristic electronic structure of graphene. It has been well known that the stability and electronic properties of the graphene flakes are sensitive to the edge shape: the armchair edge is more energetically stable than the zigzag edge [112, 113, 114]. For the electronic structure, graphene nanoribbons (GNRs) with armchair edges are either metals or semiconductors depending on the ribbon width, whereas GNRs with zigzag edges are metals with half-filled flat dispersion bands in the Brillouin zone boundary because of the delicate balance of the electron transfer among the atoms near the edge [21, 22]. Furthermore, the edge functionalization leads to variations in electronic properties of the GNR. For example, the zigzag GNR symmetrically terminated by hydrogen atoms or hydroxyl groups exhibits spin polarization around the edge atomic sites, while that terminated by O or NH groups does not exhibit spin polarization [115]. The work function and electronic structure of GNRs are also sensitive to the functional group attached to the edge. For example, the GNR with hydroxylated zigzag edges is a metal with peculiar delocalized states possessing nearly free electron nature together with the edge states of π electrons [116]. These versatile electronic properties of graphene nanoflakes arising from their structural variations also further extend the possible applications of graphene.

The large vacuum spacing around the dense covalent atomic network of graphene and other graphitic materials causes a peculiar delocalized state in the unoccupied state below the vacuum level. The states have their amplitude in the vacuum region above the atomic network with a free electron nature parallel to the atomic networks. Thus, the states are now known as nearly free electron (NFE) states or interlayer states in graphitic material [81, 82, 83, 84]. The NFE states also emerge outside the edges of GNRs, which can be regarded as the one-dimensional version of surfaces [86, 117]. Since the external electric field may cause downward shift of the potential in the vacuum region, the NFE states bound in the vacuum region by the attractive electrostatic potential outside the atomic networks shift downward when the external electric field is applied. When the NFE states shift downward and cross the E_F, electrons spill out and are injected in the NFE state.

According to the high structural aspect ratio, mechanical stiffness, chemical stability, and excellent conductivity, graphene is seen as a promising material for field emission devices. Experimental works reported electron emissions from graphene and graphene derivatives [48, 49, 118, 119]. In such field emission devices, edge atomic sites preferentially emit electrons compared with atomic sites in the bulk 2D region or those adsorbed on supporting substrates [48, 49]. Furthermore, the turn-on electric field for the electron emission is further improved by coating with a metal oxide with appropriate thickness [120]. In addition, field emission properties of graphene and graphene-related materials are sensitive to the growth condition and substrate species, which seriously affect the local and global structures of graphene. Graphene synthesized on a titanium substrate under high H_2 gas concentration shows a remarkable field enhancement factor up to 7500 [121]. Several microscopic simulations revealed that the edge enhances the field emission properties of graphene and its derivatives [52, 53, 122, 123]. Although the experimental work on fundamental aspects and applications of field emission phenomena of graphene-based materials is steadily advancing, it is still uncertain how the field emission property of graphene depends on its edge geometries and edge functionalizations, which is highly demanded for further advances in the field emission efficiency of the graphene-based devices.

To study the effect of edge shape of graphene on its field emission property, we considered the clean and edge-hydrogenated GNRs edges with edge angles of 0° for the armchair edge, 8°, 16°, and 23° for the chiral edges, and 30° for the zigzag

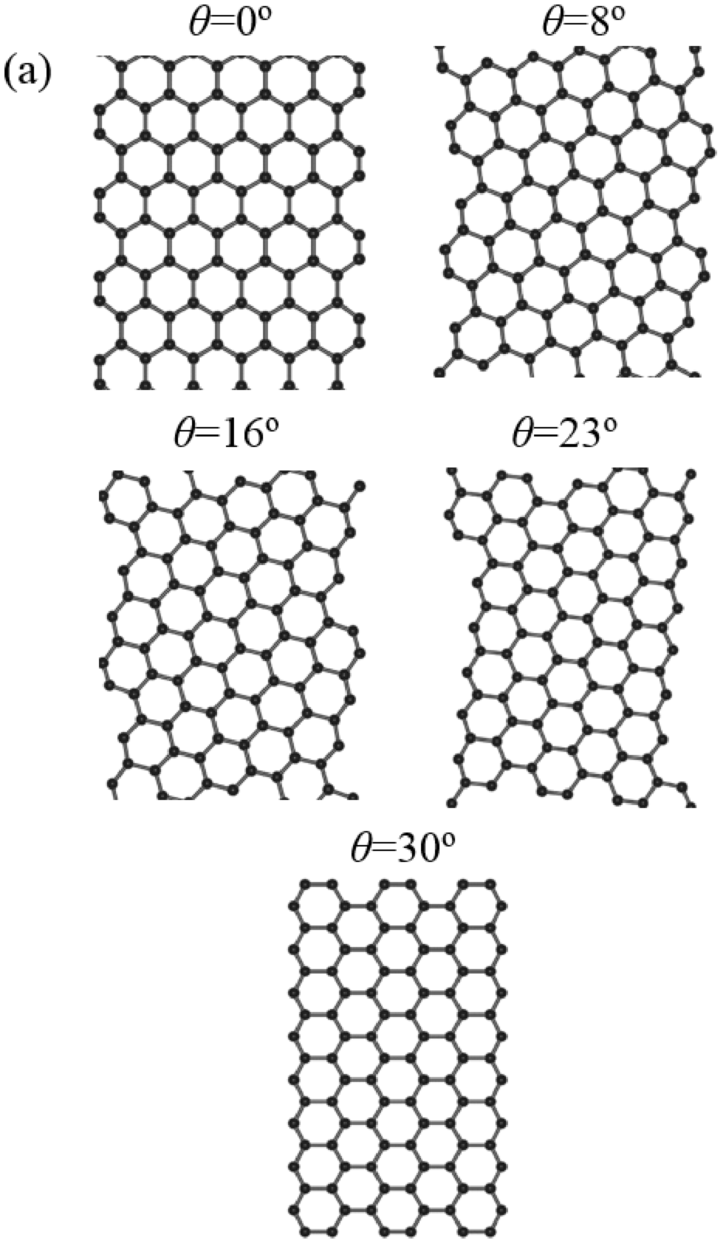

Figure 4.1: Optimized geometries of clean GNRs with edge angles of 0, 8, 16, 23, and 30° in a unit cell.

edge (Figs. 4.1 and 4.2). As for the effect of edge functionalization, we considered the AGNRs and ZGNRs, one of whose edges facing the electrode is terminated by O, CHO, COOH, H, OH, and NH functional groups, respectively, and the other is terminated by H atoms. Figure 4.3 shows the optimized geometries of edge-functionalized AGNRs and ZGNRs. To avoid steric hindrance between functional groups on adjacent edge atomic sites for the CHO and COOH cases, the edge atomic sites are alternately terminated by the H atom and the functional groups.

All calculations are conducted using the DFT with GGA. Atomic structures were optimized until the force on each atom was below 1.33×10^{-3} HR/a.u. under

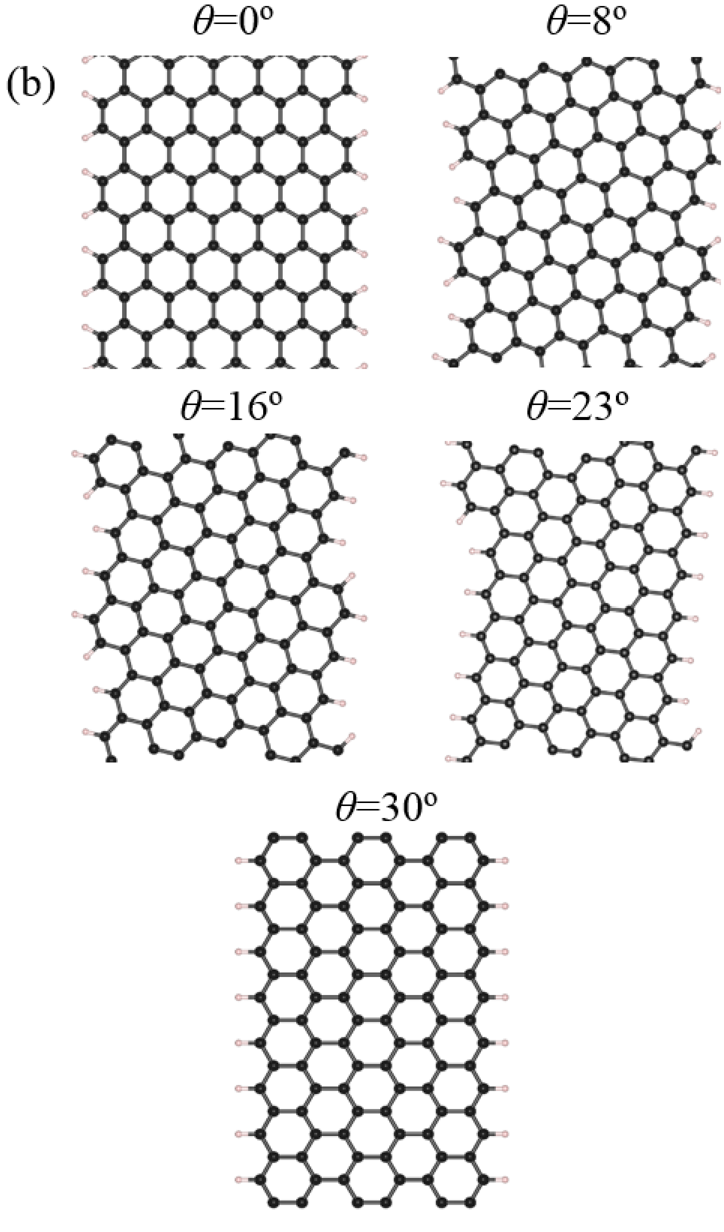

Figure 4.2: Optimized geometries of hydrogenated GNRs with edge angles of 0, 8, 16, 23, and 30° in a unit cell.

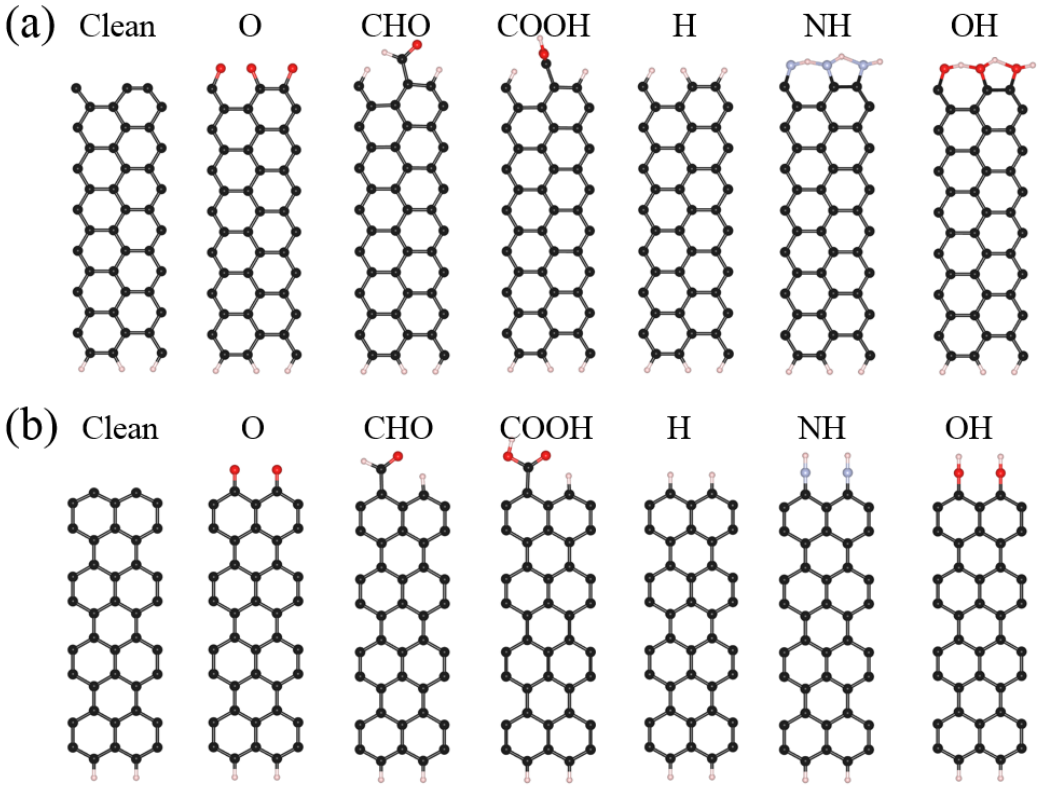

Figure 4.3: Optimized geometries of functionalized AGNRs and ZGNRs. The C, O, N, and H atoms are colored in black, red, grey, and pink, respectively.

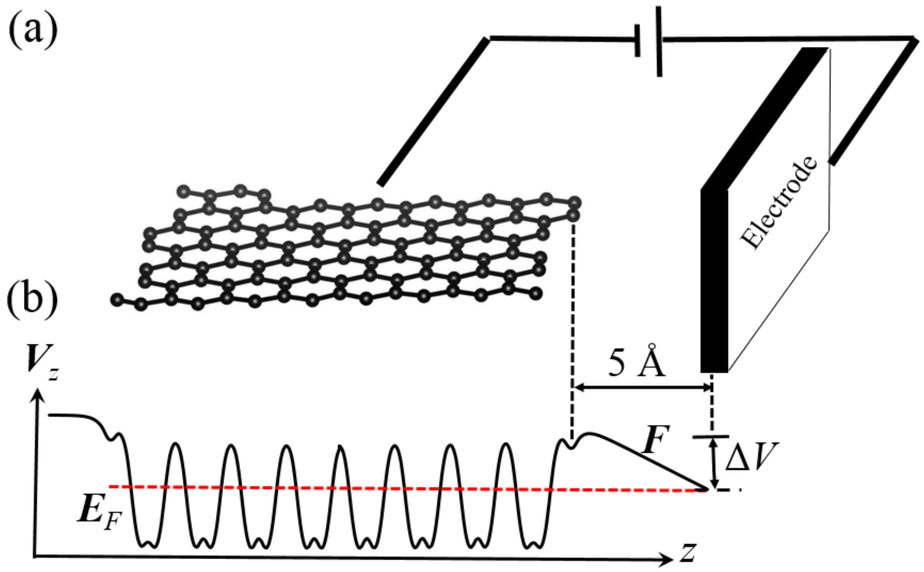

Figure 4.4: (a) Structural model and (b) schematic diagram of the plane-averaged electrostatic potential of the GNR under a lateral electric field. The dotted horizontal line denotes the E_F energy. ΔV denotes the electrostatic potential barrier for the electron emission from the GNR.

Table 4.1: Work functions of clean and hydrogenated GNRs with edge angles (θ) of 0°, 8°, 16°, 23°, and 30° (in eV).

θ	0°	8°	16°	23°	30°
Clean	5.15	6.05	5.84	6.01	6.03
Hydrogenated	3.91	3.84	3.78	3.78	3.83

the zero-electric-field condition. Integration over the Brillouin zone was carried out using an equidistance mesh of 4 k-points along the ribbon, which enabled sufficient convergence in the total energy and electronic structures of graphene and other carbon materials [114]. To inject electrons into GNRs leading to the electric field outside them, we considered a planar counter metal electrode described by the ESM having an infinite relative permittivity separated by the 5-Å vacuum spacing from the edge of GNRs [Fig. 4.4(a)] with the aid of the ESM method. In contrast, an open boundary condition is imposed at the opposite cell boundary described by a relative permittivity of 1 with the vacuum spacing of 5 Å from the other edge of the GNRs. During the calculations of the electronic structure under an electric field, all atomic structures were fixed as those obtained under a zero electric field.

4.2 Edge-shape effect on the field emission property of graphene

4.2.1 Work function

Table 4.1 shows the work functions of GNRs with clean and hydrogenated edges. For GNRs with clean edges, the work function of the armchair edge is in particular smaller than those of the other edges. The remaining edges possess almost the same work function. The rather small work function of the armchair edge is ascribed to the semiconducting electronic structure because of the strong pairing of the edge C atoms, which reduces the dangling bonds of the edge atoms [124]. In contrast, the other GNRs have metallic electronic structures, in which the E_F is pinned at dangling bond states located below the Dirac point. For GNRs with hydrogenated edges, the work function almost retains a constant value, irrespective of the edge shape, because the E_F is located at the Dirac point. Furthermore, the work function for the graphene edge decreases upon the edge hydrogenation because the dangling bond state vanishes and the dipole between the edge C and H atoms is strong. Hence, from a work function perspective, hydrogenated graphene edges may be suitable for the electron emission.

4.2.2 Potential barrier for the electron emission

Figures 4.5(a) and 4.5(b) show the electrostatic potential barrier for the electron emission from the clean and hydrogenated edges, respectively, as a function of the electric field. The potential barrier monotonically decreases with increasing electric field, irrespective of edge shape and termination. For clean edges, the potential barrier in the armchair edge is the lowest among the edges studied here for all electric fields because of its smallest work function. The potential barrier in the chiral edges (edge angles of 8, 16, and 23°) rapidly decreases with increasing electric field compared with those in the armchair and zigzag edges. Hence, the zigzag edge possesses the highest potential barrier for all electric fields. For the hydrogenated edges, the potential barrier monotonically decreases with increasing electric field. The barrier strongly depends on the edge angle, although the work function is insensitive to the edge angle: the armchair edge has the lowest barrier, whereas the zigzag edge has the highest barrier for all electric fields.

4.2.3 Electrostatic potential and electric field

To clarify the influence of the edge shape on electrostatic properties of the GNRs, we analyzed the electrostatic potential and electric field outside the GNRs with different edge angles under an external electric field. Figures 4.6 and 4.7 present contour plots of the electrostatic potential and vector plots of electric field for the GNRs with clean and hydrogenated edges, respectively, under the critical electric field at which the electrostatic potential on the electrode crosses the E_F [Fig. 4.4(b)]. The electrostatic potential under the external electric field is calculated by subtracting the electrostatic potential in the absence of an external field from that with the critical electric field to remove the deep potential valleys arising from the ions. In all cases, the electrostatic potential monotonically decreases with approaching the electrode, indicating a constant electric field in the vacuum between the graphene edge and the electrode. In contrast, the field concentrates near the edge atomic sites because of the atom-thick electron distribution in the GNRs. In addition, the electrostatic potential and the electric field are spatially modulated along the edge direction in some instances, by reflecting the detailed atomic structures of the edges: for the armchair and zigzag edges, the electrostatic potential and electric field are uniform along the edge direction, irrespective of the termination, suggesting that electrons are homogeneously distributed along the edge. In contrast, for clean chiral edges, we found the potential peaks at the edge atomic sites belonging to zigzag portions, leading to the concentration of the electric field. The fact indicates that zigzag sites are preferred in electron emissions than armchair sites in graphene with the chiral edges because of the electron concentration induced by the dangling bond. For chiral GNRs with hydrogenated edges, the potential peaks and field

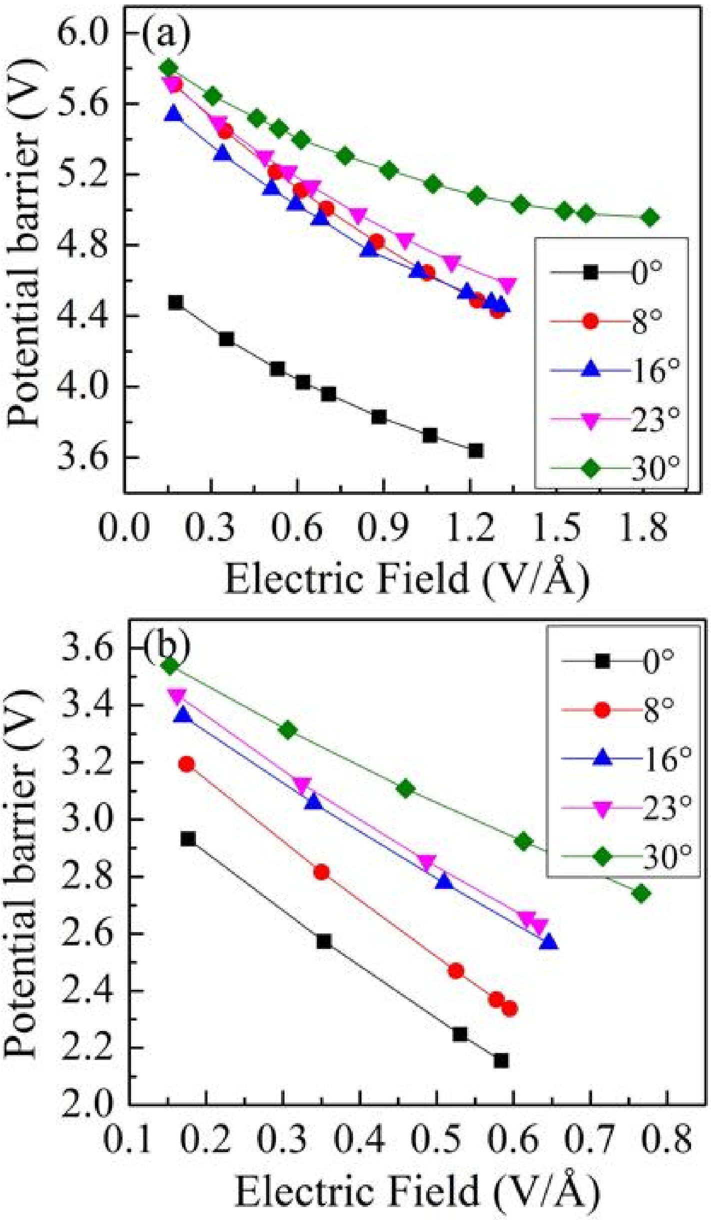

Figure 4.5: Electric-field dependence of the potential barrier for the field emission in the (a) clean and (b) hydrogenated GNRs with the edge shape ranging from armchair to zigzag.

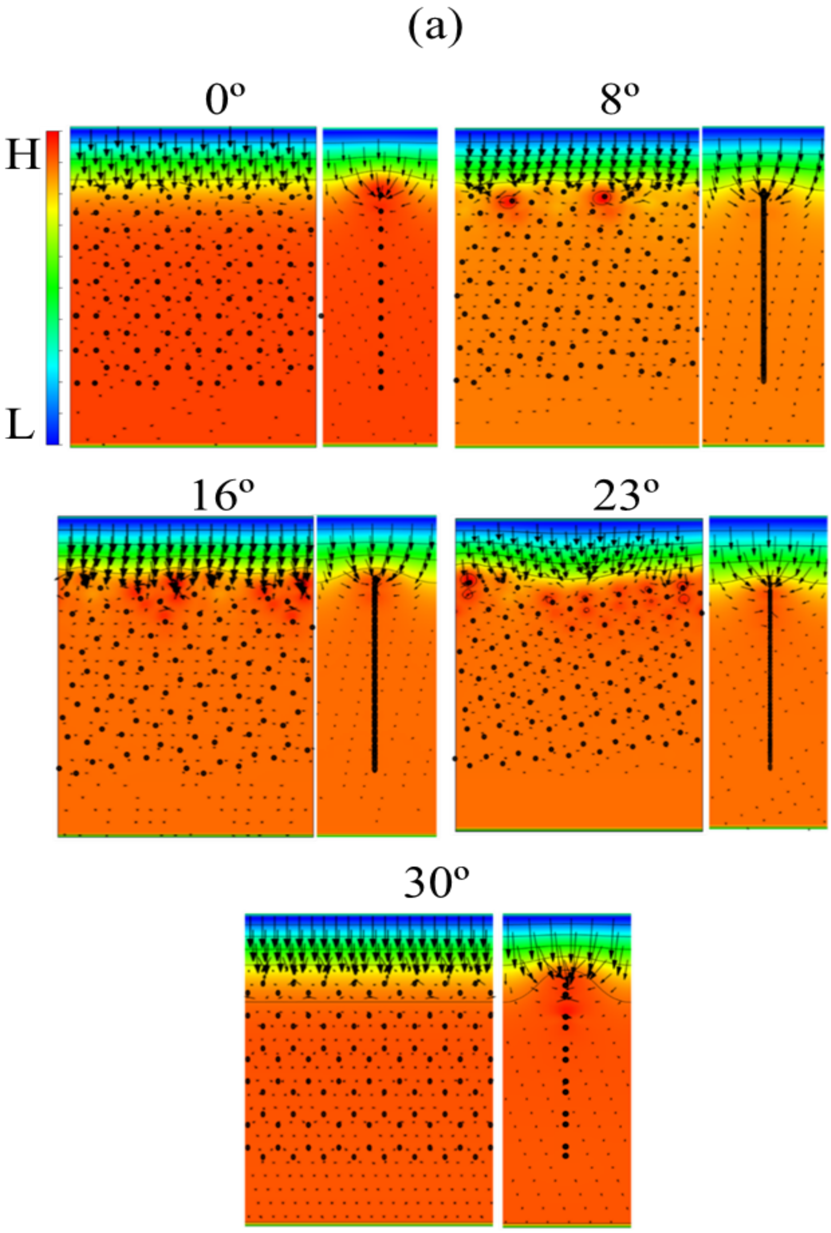

Figure 4.6: Contour and vector plots of the electrostatic potential and the electric field of clean GNRs with edge angles of 0, 8, 16, 23, 30° subject to the critical electric field for the electron emission. The left and right panels for each angle correspond to parallel and vertical planes, respectively, of the GNRs. Black dots denote the atomic position of GNRs. Red, green, and blue indicate the high, moderate, and low potential regions, respectively.

concentrations occur at the zigzag sites, even though the edges do not possess a dangling bond. In this case, the potential peak is ascribed to the higher charge density around the zigzag sites induced by the edge states.

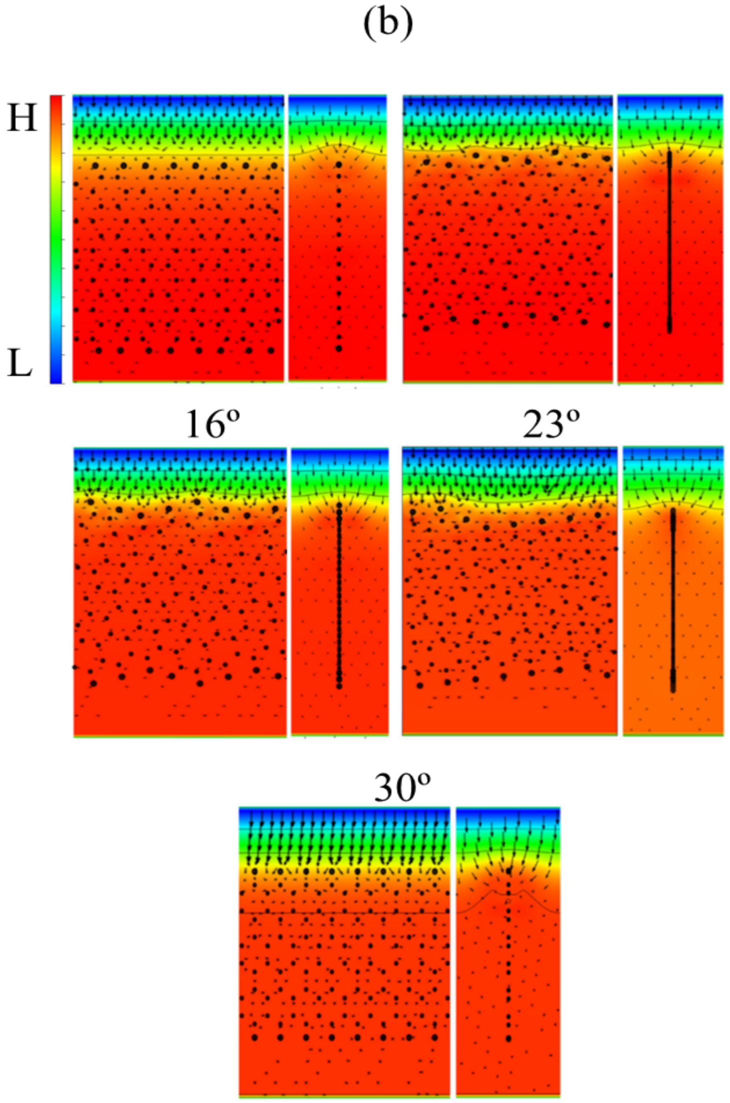

Figure 4.7: Contour and vector plots of the electrostatic potential and the electric field of edge-hydrogenated GNRs with edge angles of 0, 8, 16, 23, 30° subject to the critical electric field for the electron emission. The left and right panels for each angle correspond to parallel and vertical planes, respectively, of the hydrogenated GNRs. Black dots denote the atomic position of hydrogenated GNRs. Red, green, and blue indicate the high, moderate, and low potential regions, respectively.

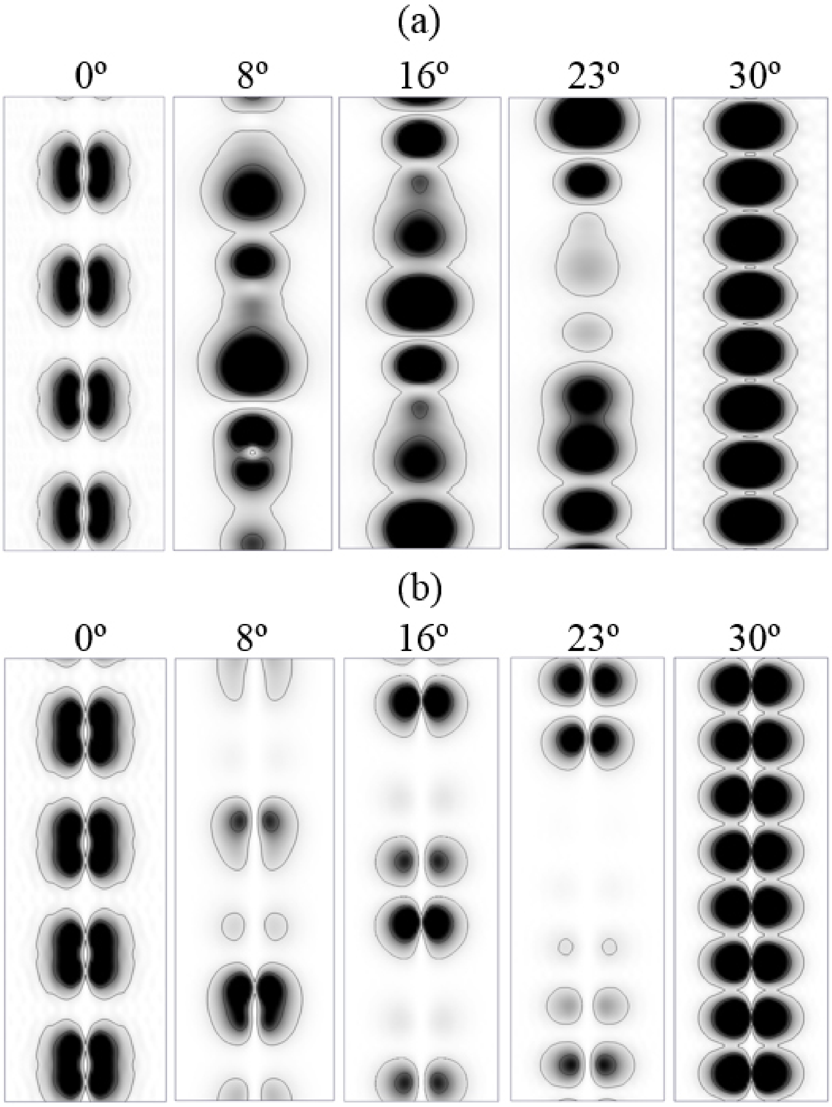

Figure 4.8: Contour plots of LDOS of (a) clean and (b) hydrogenated GNRs with various edge angles under the critical electric field for the electron emission. The contours are depicted on the plane parallel to the electrode situated at the 1 Å from the outermost edge atomic site.

4.2.4 Local density of states

Figures 4.8(a) and 4.8(b) show the local density of states (LDOS) outside the GNRs with clean and hydrogenated edges, respectively, near the E_F, to simulate projected images by the emitted electrons from the edges, since the electron tunneling from the edge to the electrode is attributed to the electron states near the E_F. The LDOS is defined by

$$\rho(r) = -\frac{1}{\pi} \mathrm{Im} \sum_{n,k} \int_{E_F-\Delta}^{E_F} dE \frac{|\phi_{n,k}|^2}{E - \epsilon_{n,k} + i\delta}, \tag{4.1}$$

where Δ is 1 eV. The LDOS depends on the edge shape and termination. Thus, the edge shape and termination affect the field emission patterns from the graphene edges. For clean and hydrogenated armchair edges, the LDOS is uniformly extended along the direction of the edge with bonding π-state nature. For clean chiral and zigzag edges, the LDOS does not have a nodal line with respect to the graphene layer, indicating their dangling σ-bond state nature. The LDOS also contains edge states, because it is slightly elongated along the direction normal to the graphene layer. In contrast, for hydrogenated chiral and zigzag edges, the LDOS image exhibits the nonbonding π-state nature, which also implies the fact that the edge state at or near the zigzag portions of the hydrogenated chiral or zigzag edges significantly contributes to the electron emission.

4.2.5 Field emission current

We analyzed the emission current density as a function of the plane-averaged external electric field. The current density I is calculated from the relation

$$I = \lambda \nu T, \tag{4.2}$$

where λ is the averaged electron charge density accumulating near the edge by the external electric field, and ν is the collision frequency of electrons estimated by $\nu = E_k/h$ with the kinetic energy E_k. Since the electron emission is associated with the electron near the E_F, the emission current may be overestimated by the definition of ν under the low temperature condition. The transmission coefficient T is evaluated using the equation

$$T = \exp\left[\frac{-4\pi}{h}\int\sqrt{2m(V(z)-E_F)}dz\right], \tag{4.3}$$

where $V(z)$ is the plane-averaged electrostatic potential.

The emission current density from clean and hydrogenated edges as a function of the electric field is shown in Figs. 4.9(a) and 4.9(b), respectively. The emission current density increases with increasing the electric field. It is also sensitive to the edge shape and termination. The armchair edge generates a larger current density than the other edges for both clean and hydrogenated cases. The edge hydrogenation substantially enhances the emission current density for all edge shapes. These behaviors are attributed to a decrease in the electrostatic potential barrier outside the ribbon edge upon edge hydrogenation. Furthermore, Fowler-Nordheim plots at the hydrogenated edges exhibit linear relations with regard to the reciprocal of the electric field (Fig. 4.10).

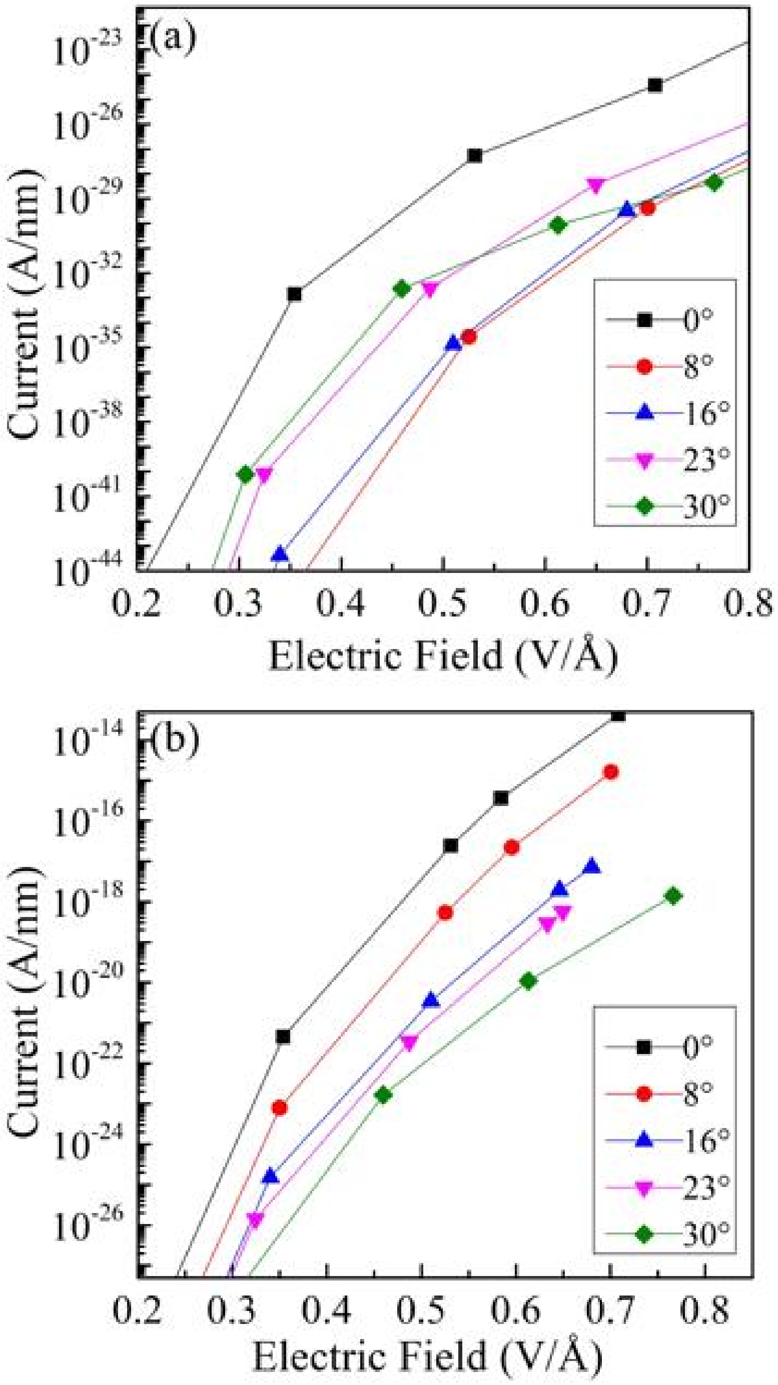

Figure 4.9: Field emission current density as a function of the plane-averaged electric field for (a) clean and (b) hydrogenated GNRs.

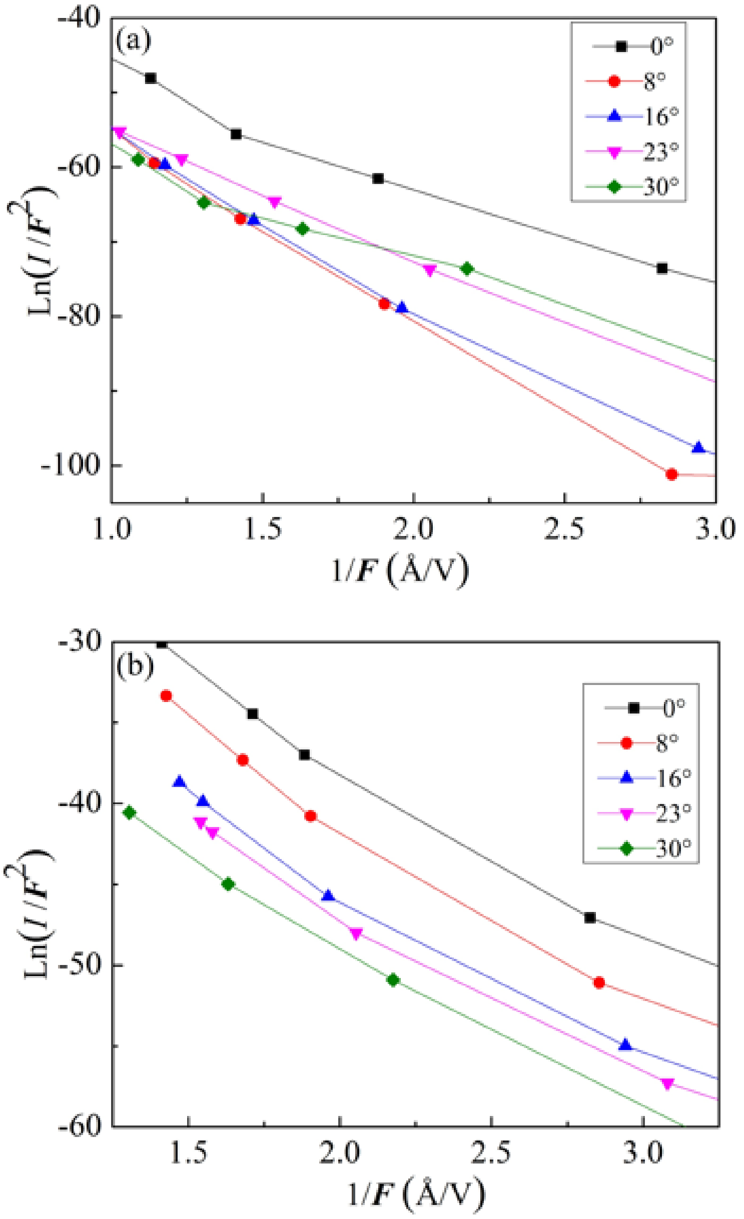

Figure 4.10: Fowler-Nordheim plots of (a) clean and (b) hydrogenated GNRs. ***F*** indicates electric field.

4.3 Edge-functionalization effect on the field emission property of graphene

4.3.1 Work function

Table 4.2 shows the work functions of GNRs with clean and functionalized edges with O, CHO, COOH, H, NH, and OH groups. The work function depends on the attached functional group and edge shape. For the armchair edge, O, CHO, and NH groups increase the work function to 7.09, 6.21, and 5.95 eV, respectively, from 5.38 eV for the clean edge, while H, OH, and COOH decrease its work function to 3.71, 3.33, and 4.48 eV, respectively. For the zigzag edge, O and CHO groups increase the work function to 8.12 and 6.59 eV, respectively, from 5.95 eV for the clean edge, while H, OH, NH, and COOH functional groups decrease the work function to 3.84, 1.99, 2.67, and 4.95 eV, respectively. The OH group causes the smallest work function for both the armchair and zigzag edges among all functional groups studied here, because it has the largest dipole moment at the edges. The clean zigzag edge has a larger work function than the clean armchair edge, so that the work functions of the functionalized zigzag edges are also larger than those of the functionalized armchair edges except when the edge is terminated by OH or NH. For OH and NH functionalizations, the zigzag edge shows a smaller work function than that of the armchair edge, because the edge geometries cause the dipole at the zigzag edge functionalized by OH or NH to be stronger than that at the armchair edge.

Table 4.2: Work functions of AGNRs and ZGNRs with clean and functionalized edges (in eV).

Edge	Clean	O	CHO	COOH	H	NH	OH
AGNR	5.38	7.09	6.21	4.48	3.71	5.95	3.33
ZGNR	6.34	8.12	6.59	4.95	3.84	2.67	1.99

Figures 4.11 and 4.12 show the distributions of accumulated electrons in AGNRs and ZGNRs, respectively, under an external electric field, which injects 0.05 electrons into the GNR. We find that injected electrons are primarily distributed around the ribbon edge depending on the edge shape and functionalization. For the O and NH armchair edges, the carrier concentrations occur near the edge atomic sites, while for other armchair edges, carriers not only accumulate near the edge atomic sites but also penetrate inside the GNRs. In contrast, electrons in GNRs with zigzag edges are mostly accumulated around the edges, *i.e.*, at edge C atoms and functional groups, suggesting that these atoms contribute to the field emission from the graphene edges. In particular, the electron distributions outside the clean, O, and CHO edges indicate

that the dangling bond state at each edge is also responsible for the field emission. By integrating the electron distribution around each edge atomic site, we find that approximately 90% of injected electrons are accumulated around the edge atomic sites of all GNRs.

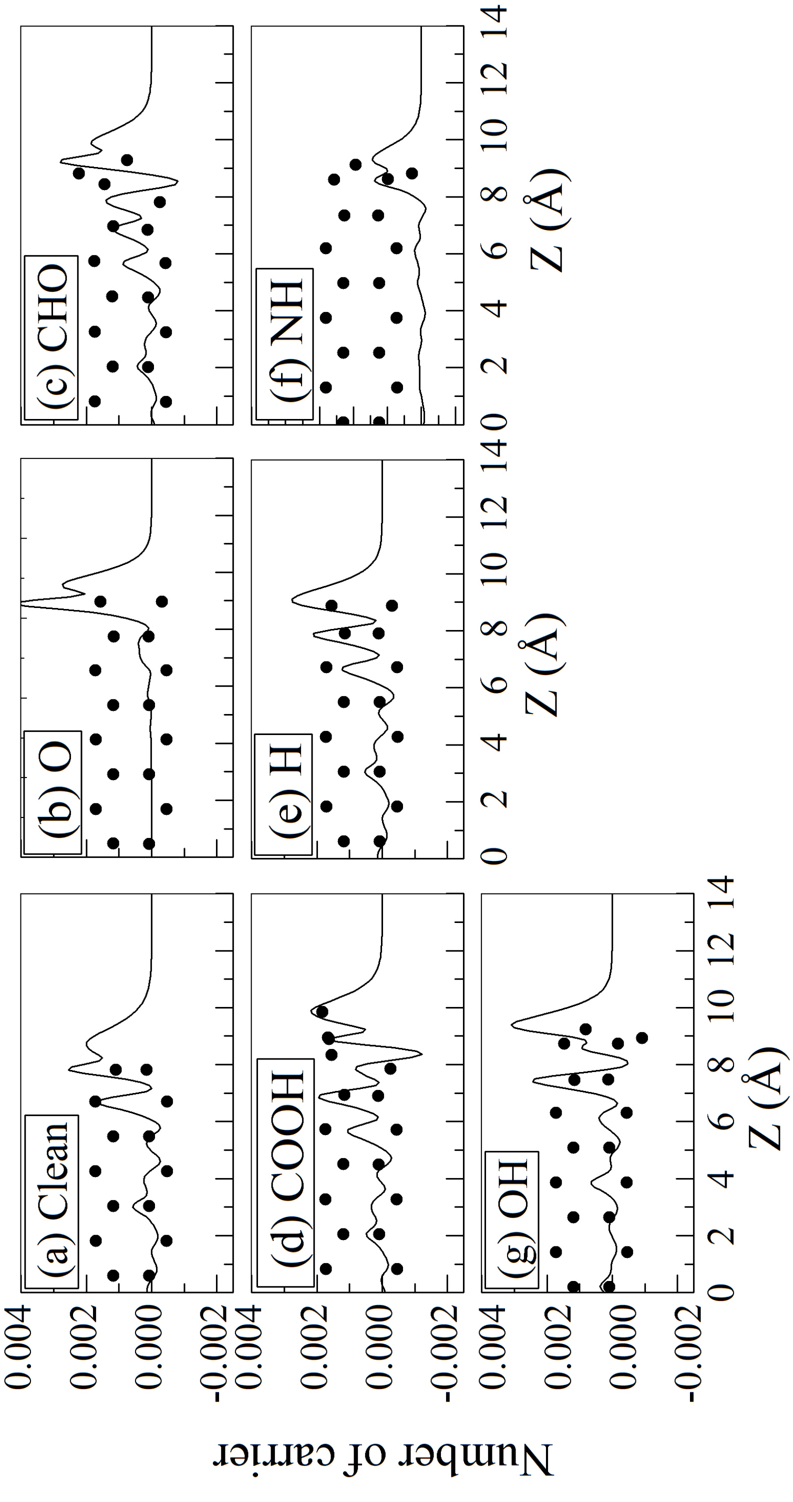

Figure 4.11: Distribution of accumulated electrons in AGNRs with (a) clean, (b) O, (c) CHO, (d) COOH, (e) H, (f) NH, and (g) OH edges under an external electric field corresponding to doping of 0.05 electrons per unit cell. Black dots in each panel indicate atomic positions.

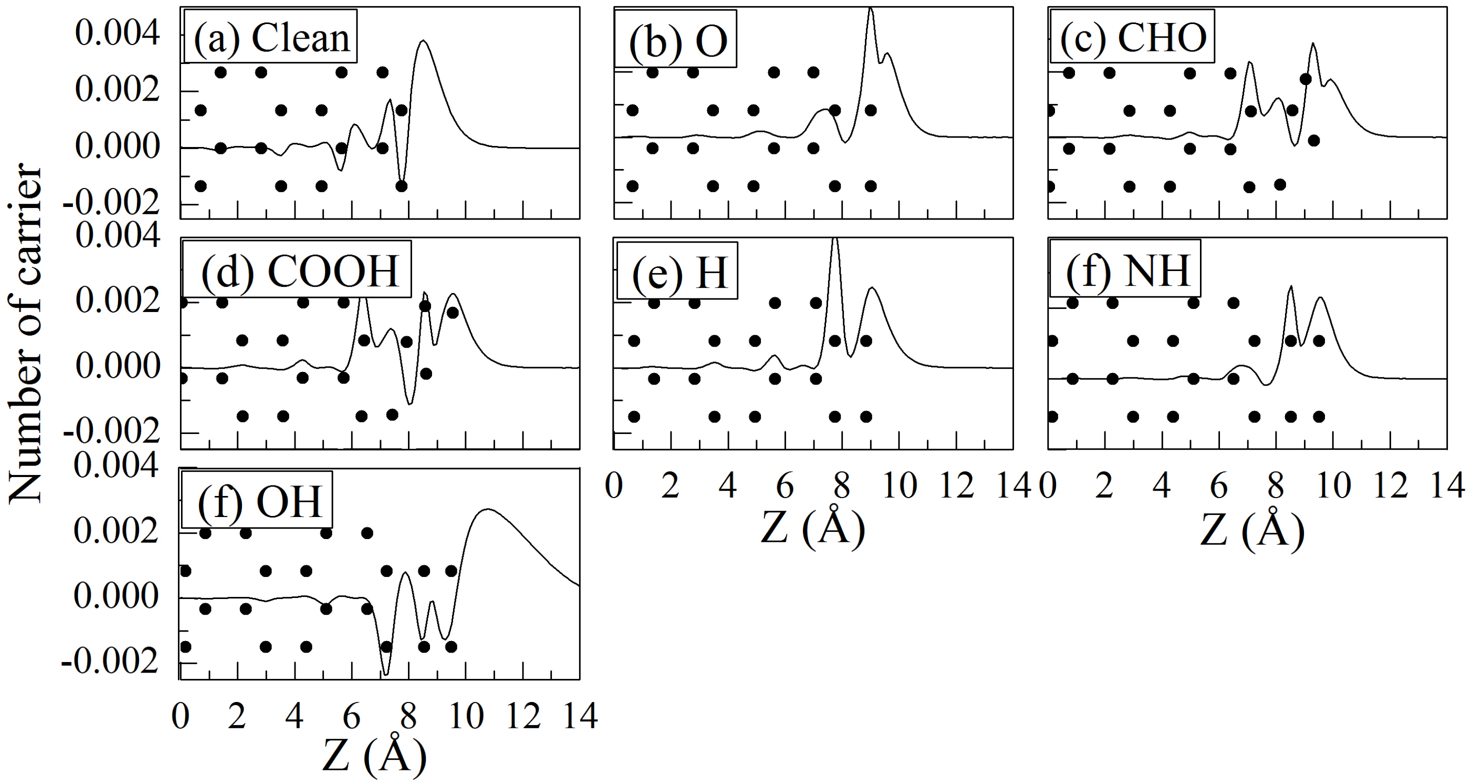

Figure 4.12: Distribution of accumulated electrons in ZGNRs with (a) clean, (b) O, (c) CHO, (d) COOH, (e) H, (f) NH, and (g) OH edges under an external electric field corresponding to doping of 0.05 electrons per GNR. Black dots in each panel indicate atomic positions.

4.3.2 Potential barrier for electron emission

Since the electrostatic potential barrier outside a material is a key factor in determining its field emission, we calculate this barrier for electron emission from edges with OH, H, O, CHO, COOH, and NH functional groups. Figure 4.13 shows the potential barriers of GNRs with clean and functionalized edges as functions of the electric field. Each potential barrier depends on the edge shape and termination. For the armchair edge, the potential barrier decreases monotonically with increasing electric field for all functional groups. Moreover, the potential barrier depends on the edge functionalization: the AGNR with O, NH, or CHO edge has a larger potential barrier than that with a clean edge, while the AGNR with COOH, H, or OH has a smaller potential barrier than that with a clean edge [Fig. 4.13(a)]. Therefore, we expect that COOH, H, and OH improve the field emission of graphene with the armchair edge. In particular, the edge with the OH group will have the largest field emission current among all armchair edges, because it has the lowest potential barrier among all edge-functionalized AGNRs.

For the zigzag edge, the potential barrier also monotonically decreases with increasing electric field for all functionalizations except for OH, whose potential barrier increases with increasing the field [Fig. 4.13(b)]. Even when the external electric field increases, the potential barrier of the OH edge remains the lowest for all zigzag edges studied here. As in the case of armchair edges, zigzag edges with O and CHO groups have higher potential barriers compared with other functionalized zigzag edges. By summarizing these facts, graphene with an OH-functionalized zigzag edge is the most efficient for electron emission among the structures studied here.

4.3.3 Electrostatic potential and the electric field

To clarify the physical origin of this anomalous potential barrier associated with the field for the ZGNR terminated by the OH group, we investigate the electrostatic potential and electric field of functionalized ZGNRs under the critical external electric field (Fig. 4.14). The electrostatic potential shown in Fig. 4.14 is calculated by taking the difference between the electrostatic potential for the ZGNRs under the electric field and those under the zero electric field to remove the deep potential arising from the ions. The electrostatic potential peak emerges in the vacuum region outside the OH terminated edge and extends along the edge. This potential peak outside the OH terminated edge leads to the opposite electric field to the external electric field by the electrode at the vicinity of the edge atomic site, which suppresses the electron emission from the OH terminated edge. The potential peak is ascribed to the spilled electron in the vacuum region owing to the NFE state, which causes the repulsive potential for the electrons. Therefore, the spilled electron due to the NFE state causes the anomalous potential barrier for electron emission from the

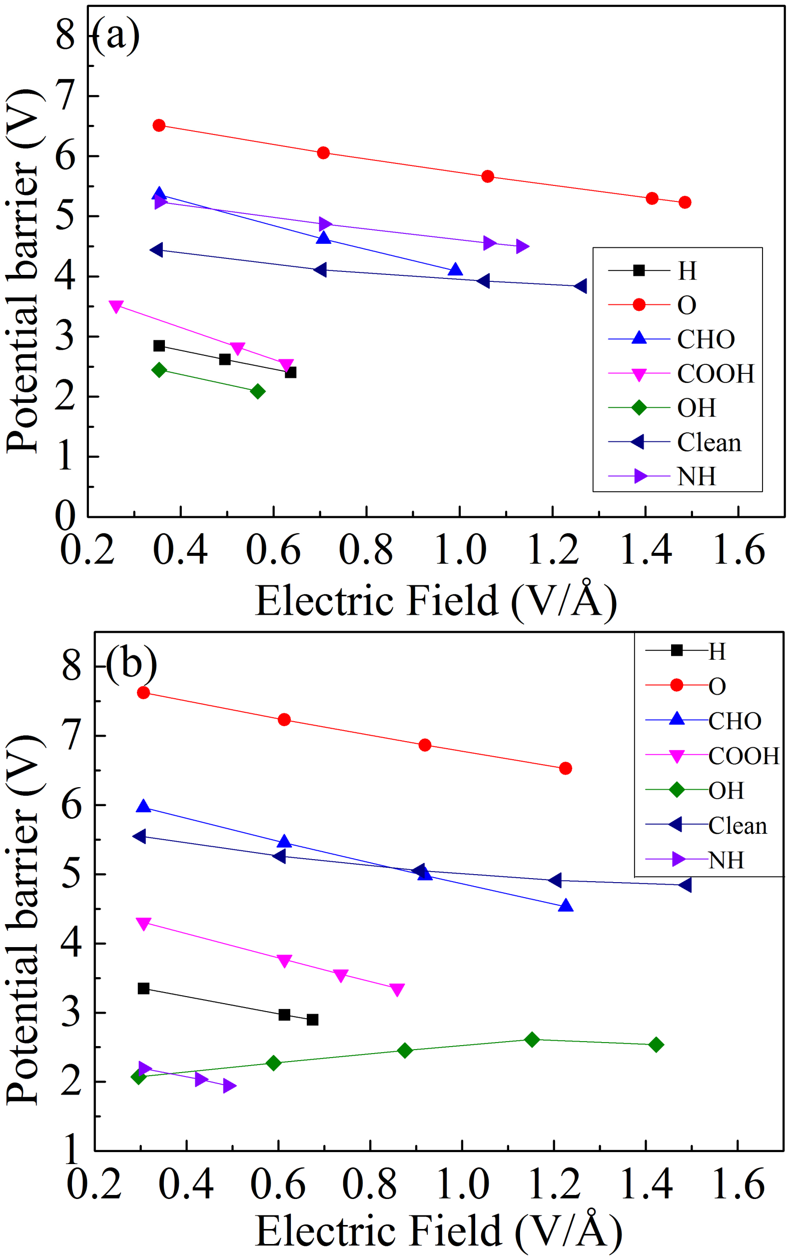

Figure 4.13: Potential barriers for electron emission from functionalized (a) armchair and (b) zigzag edges as functions of the external electric field.

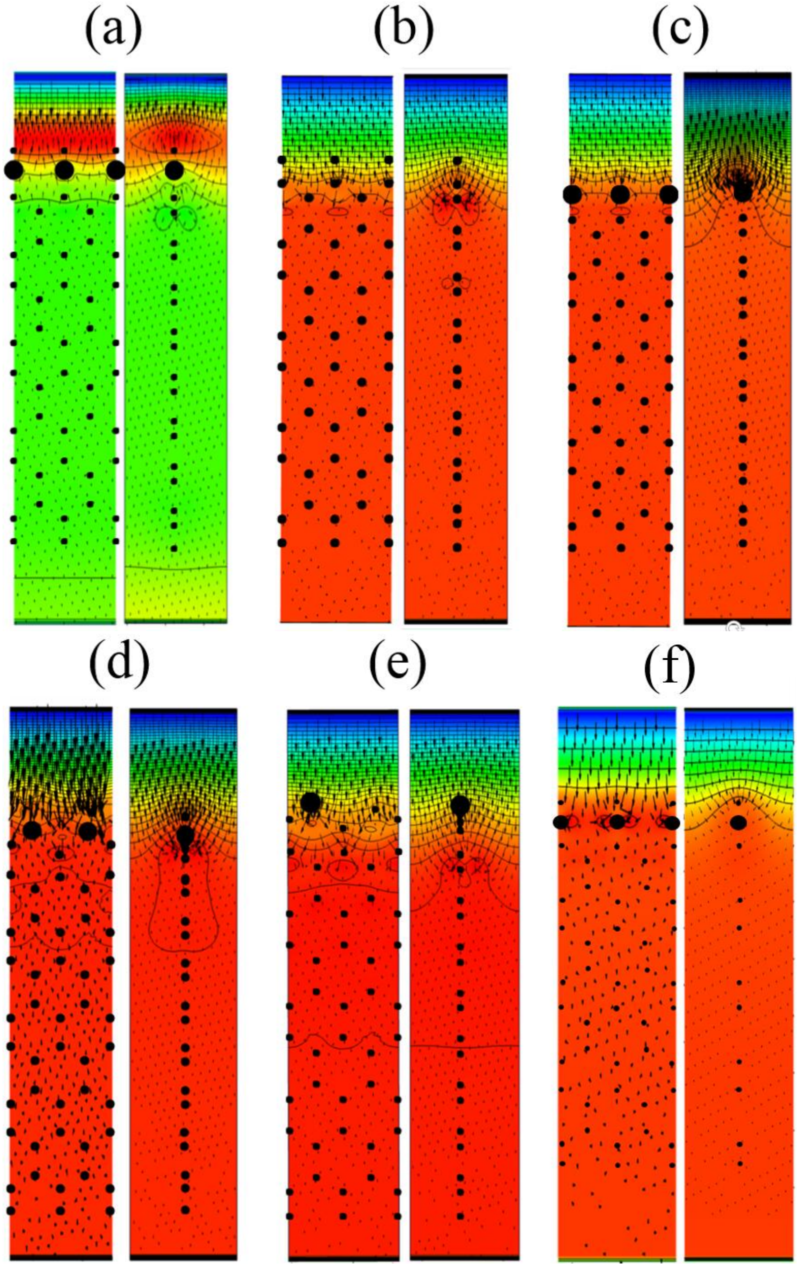

Figure 4.14: Contour and vector plots of electrostatic potential and the electric field, respectively, of ZGNR functionalized by (a) OH, (b) H, (c) O, (d) CHO, (e) COOH, and (f) NH functional groups under the critical electric field for the electron emission. The left and right panels in each figure correspond to parallel and vertical planes, respectively, of ZGNRs. Black dots denote the atomic position of edge functionalized ZGNRs. Red, green, and blue indicate the high, moderate, and low potential regions, respectively.

OH terminated edges. For the edges with H, O, CHO, COOH, and NH groups, the electrostatic potential monotonically decreases with approaching the electrode leading to the constant electric field except the vicinity of the edge atomic site. At the vicinity of the edges, the field concentration occurs owing to the ultimate thickness of the electron distribution on ZGNRs. In addition, along the edge direction, we also found that the spatial modulation of the electrostatic potential owing to the functional groups, leading to the further field concentration around them. Thus, ZGNRs with H, O, CHO, COOH, and NH edges may efficiently emit the electron from their edges, and the electric field required for the electron emission depends on their work function. In contrast, for the ZGNR with OH terminated edge, owing to the extended nature of the NFE states, the field concentration is hardly to occur at or near the edge. Therefore, the graphene with OH terminated edge may not work as the efficient field emission source without further modification around the edge environment in terms of the electrostatic potential and electric field near the GNR edge. During the calculations under the electric field (electron doping), the atomic coordinate is fixed to that under the zero electric field. The electron injection may elongate OH bond, so that the barrier slightly decrease under the structural reconstruction near the edges associated with the electric field.

4.3.4 Local density of state

Figure 4.15 shows the local density of states (LDOS) for functionalized ZGNRs near the E_F and at the vacuum space between the functional edge and electrode, which is defined by

$$\rho(r) = -\frac{1}{\pi} \mathrm{Im} \sum_{n,k} \int_{E_F-\Delta}^{E_F} dE \frac{|\phi_{n,k}|^2}{E - \epsilon_{n,k} + i\delta}, \tag{4.4}$$

where Δ is 1 eV, to simulate the projected images by the emitted electrons from the functionalized graphene edges, since the tunneling electron from edges to electrode is associated to the electron states near the E_F. From the LDOS images at the plane in vacuum parallel to the electrode, the LDOS depends on the functional group attached to the edges. The fact indicates that the functional group affects the field emission pattern from the functionalized edges of graphene. For H, O, CHO, COOH and, NH edges, the LDOS possess symmetric distribution with respect to the ZGNR plane, indicating the p_z nature of C and O/N atoms. In contrast to these functionalized edges, LDOS of the OH terminated edge shows different characteristics from the other edges: the LDOS exhibits symmetric distribution with respect to the ZGNR plane. Furthermore, the LDOS is extended along the direction of the edge, leading to approximately uniform distribution.

4.3.5 Field emission current

We calculated the emission current from functionalized edges as a function of the external electric field. The current density I was calculated from the relation

$$I = \lambda \nu T, \tag{4.5}$$

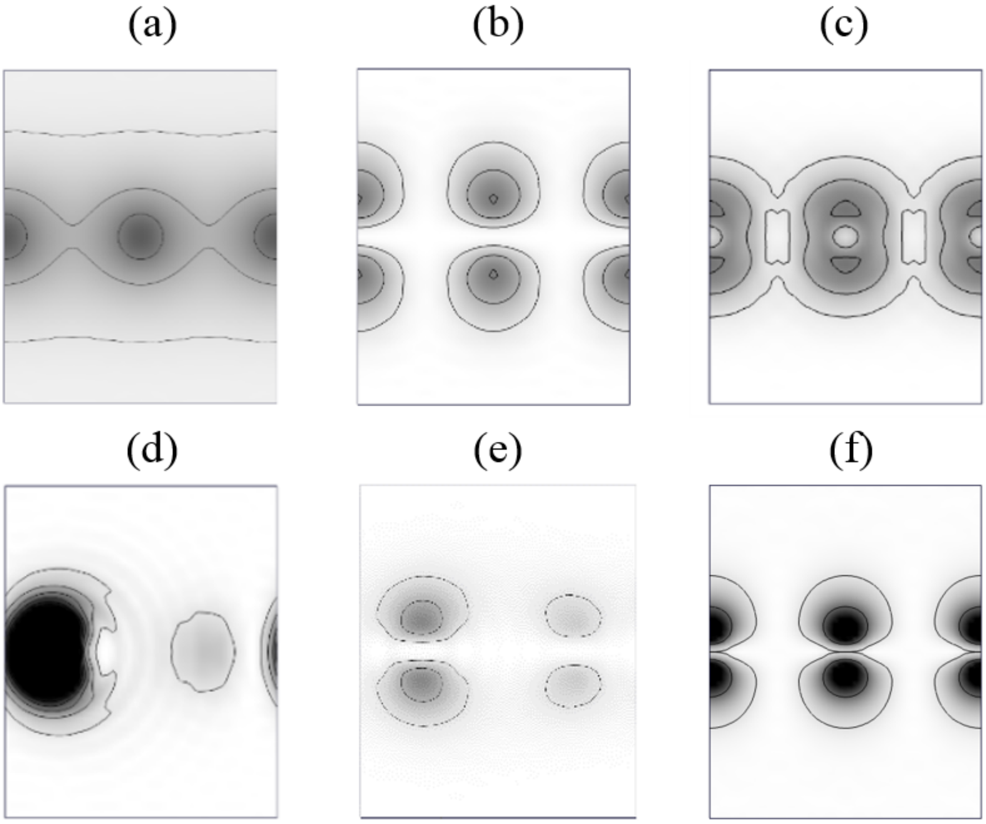

Figure 4.15: Contour plots of LDOS of ZGNRs functionalized by (a) OH, (b) H, (c) O, (d) CHO, (e) COOH, and (f) NH functional groups under the critical electric field for the electron emission. The contours are depicted at the plane parallel to the electrode situated 1 Å from the outermost edge atomic site.

where λ is the electron density accumulated near the edge by the external electric field, and ν is the collision frequency of electrons estimated by $\nu = E_k/h$ with the electron kinetic energy E_k. The transmittance coefficient T is evaluated using the equation

$$T = \exp\left[\frac{-4\pi}{h}\int\sqrt{2m(V(z)-E_F)}dz\right], \tag{4.6}$$

where $V(z)$ is the plane-averaged electrostatic potential across the GNRs. Figures 4.16(a) and 4.16(b) show calculated emission current densities for the clean and functionalized armchair and zigzag edges, respectively, as functions of the external electric field. Each emission current density I depends on the external electric field, edge shapes, and edge functional groups. Overall, the emission current monotonically increases with increasing electric field. The increase of the current strongly depends on the edge shape and functional group. For the armchair edge [Fig. 4.16(a)], OH, H, or COOH group enhances the emission current, while O, CHO, or NH suppresses the current. The emission current strongly correlates with the potential barrier outside the edge: a small potential barrier leads to a large emission current from the functionalized armchair edges.

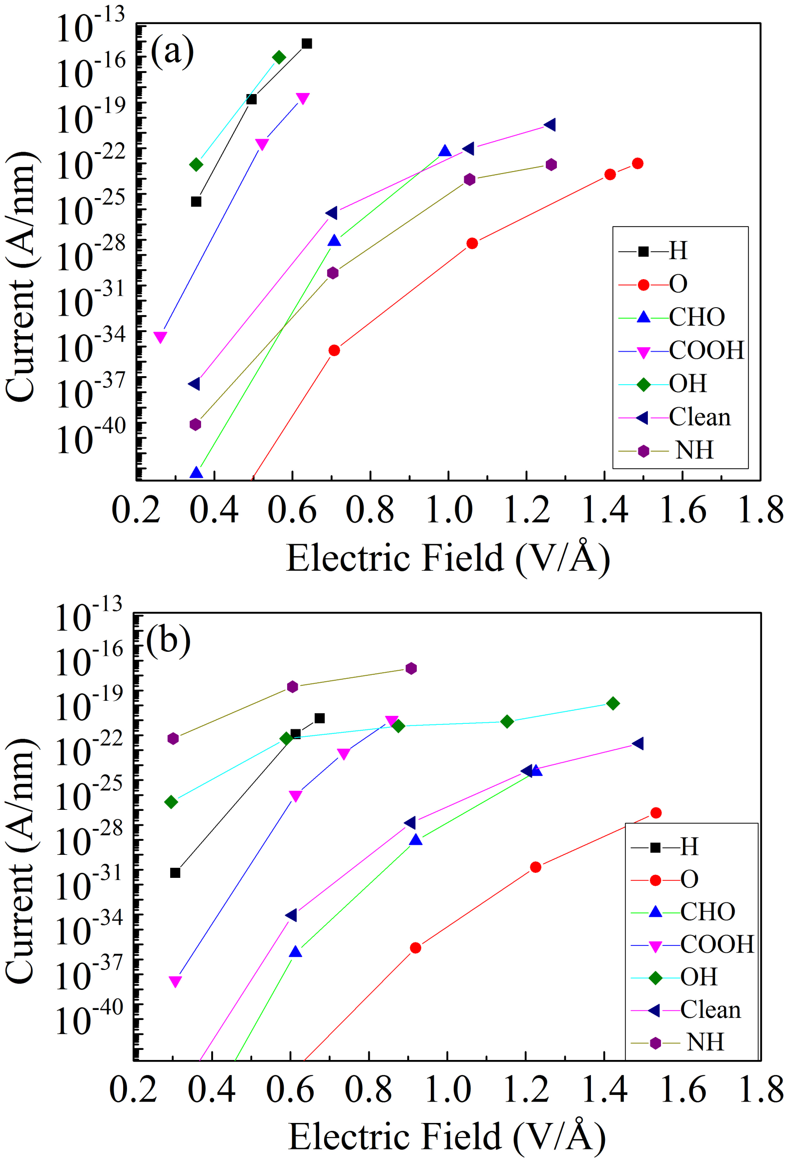

Figure 4.16: Field emission current densities from functionalized (a) armchair and (b) zigzag edges as functions of the external electric field.

For the zigzag edge, the O functionalization substantially suppresses the emission current, while other groups except CHO enhance the current. The NH functionalization provides the largest current because this zigzag edge has a low potential barrier. The zigzag edge with an OH group also has a large emission current because of the low potential barrier outside the edge. Note that the emission current from the OH edge less depends on the external electric field than does that from the other functionalized edges. This implies that the edge with the OH group is stable emission source with respect to the electric field. For H, COOH, CHO, OH, and O groups, the armchair edge provides a larger emission current than that with the zigzag edge, as in the case of clean edges.

4.3.6 Electrostatic potential barrier of hydrogenated graphene edge under high electric field

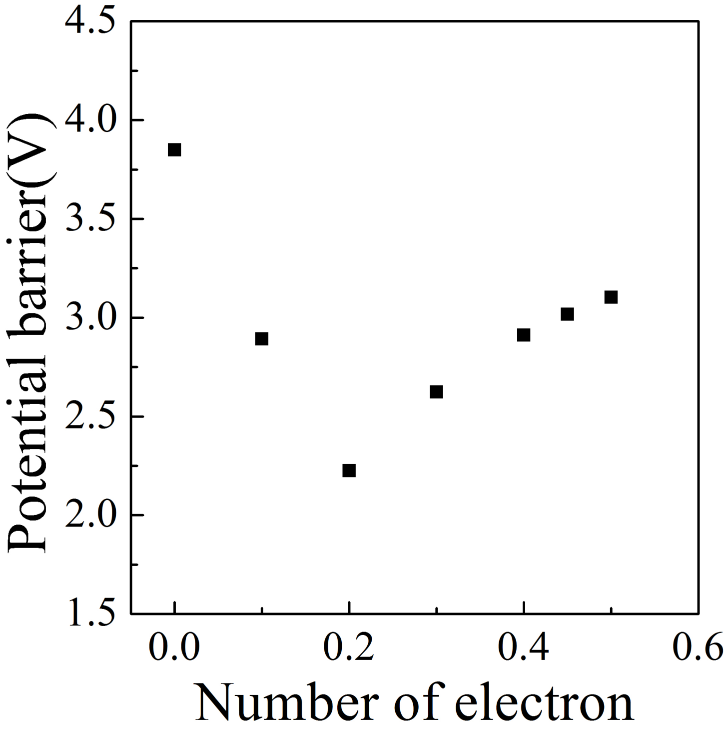

Figure 4.17: The electrostatic potential barrier, ΔV, at the vacuum region of hydrogenated ZGNR as a function of the number of the doped electron per unit cell.

The electric field naively decreases the electrostatic potential barrier in vacuum region for the electron emission from the graphene edges. To check the correlation between electrostatic potential barrier and electric field. Figure 4.17 shows the electrostatic potential barrier ΔV for the electron emission outside the hydrogenated ZGNR as a function of the number of doped electron in the ZGNR. The potential barrier decreases with the increase in the number of doped electrons up to 0.2e doping corresponding to the increase of the external electric field. However, the potential barrier, then, increases with further increase in the number of doped electrons. The fact indicates that too strong electric field or too many doped electrons may hinder the electron emission from the graphene edges, which implies the electrostatic environment outside the edge is modulated by the carrier injection.

To elucidate the reason why the electrostatic potential barrier outside the hydrogenated ZGNR increases under 0.3e doping, we further investigate the electronic structure of the hydrogenated ZGNR under the carrier concentration of 0.3e per unit cell. Figure 4.18 shows the electronic structures and squared wavefunctions at the Γ point around the E_F of the hydrogenated ZGNR without and with additional

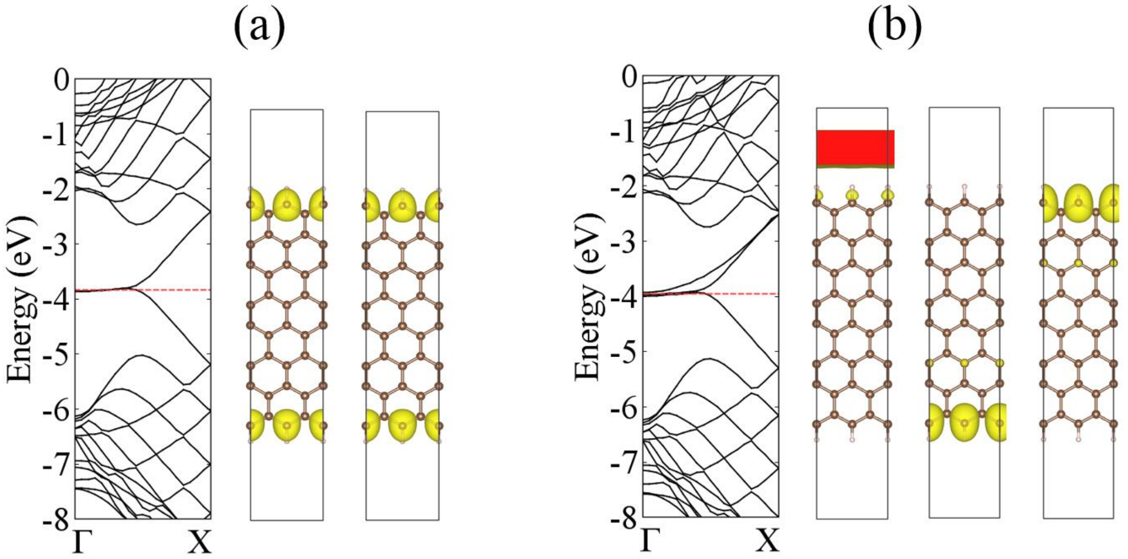

Figure 4.18: Electronic structure and squared wavefunctions at the Γ point and the E_F of hydrogenated ZGNR (a) without electron doping and (b) with excess electron of 0.3e. The red dotted line indicates the E_F energy.

electron. The non-doped ZGNR with hydrogenated edges is a metal in which two flat dispersion bands cross the E_F around the Γ point [Fig. 4.18(a)]. These states are localized at the edge C atoms, indicating their edge state nature. Note that the edge states are folded into the vicinity of the Γ point from the X point, because the energy band calculation is conducted under the double periodicity of the ZGNR. In contrast, the functionalized ZGNR with 0.3e doping exhibits an unusual electronic structure: a parabolic dispersion band emerges at the Γ point around the E_F in addition to two flat dispersion bands [Fig. 4.18(b)]. Two flat dispersion bands are distributed on the edge C atoms terminated by H atoms, exhibiting the edge state nature. In contrast, the state with the parabolic dispersion is distributed in the vacuum region outside the edge facing to the electrode indicating their NFE state nature. Thus, under the electron concentration of 0.3e or higher, the electrons are spilled out the vacuum region attributed from the downward shift of the NFE state. The spilled electron in NFE states cause the increase in the electrostatic potential in the vacuum region where the NFE state has their maximum amplitude.

4.4 Conclusion

We investigated the electronic properties of edges of clean and hydrogenated GNRs with respect to their edge shapes under the lateral electric fields, using the DFT with the ESM method. The electrostatic potential properties of the GNR were found to depend on the edge shape and termination. The armchair edge possesses lower potential barrier and larger field emission current than the other edges, irrespective of edge termination. Furthermore, hydrogenation decreases the potential barrier by introducing a dipole, causing an increase in the field emission current. In addition, for chiral GNRs, the electron emission is primarily attributed to the zigzag portion of edges because of the concentration of electrons arising from either the dangling bond state or the edge state.

We also investigated the electrostatic potential properties of GNRs with zigzag and armchair edges functionalized by O, CHO, COOH, H, NH, and OH groups under the external electric field. Our calculations revealed that the work functions and potential barriers for the electron emission from these edges depend on the attached functional groups. Accordingly, the emission current depends not only on the applied electric field but also on the functional group. GNRs with H, OH, and COOH functional groups exhibit remarkable field emission currents from their edges, owing to their low potential barriers. In contrast, edges with O termination have lower emission currents compared with the other functionalized edges, owing to their higher electrostatic potential barriers. The edges functionalized by the NH group show unusual behavior whereby the NH group enhances the field emission current from the zigzag edge but suppresses that from the armchair edge, because the dipole moment of the NH in the zigzag edge is larger than that in the armchair edge, arising from the conformation difference of the NH group.

In addition, we found that the potential barrier in the vacuum region outside the edge depends on the carrier concentration in H terminated ZGNR edge. The potential barrier, firstly, monotonically decreases with increasing the number of carriers, while then it increases above the critical carrier concentration at which the NFE crosses the E_F inducing the electron leakage in the vacuum region, which suggests that the strong electric field also causes a potential barrier for the electron emission from the H terminated ZGNR edge owing to the downward shift of the NFE state. The present results provide a guiding principle to further enhance the field emission current from the graphene edges.

Chapter 5

Summary

In this thesis, we studied geometric and electronic properties of low-dimensional materials performing the first-principle total-energy calculations based on the DFT.

In Chapter 3, we investigated the geometric and electronic properties of h-GaN. In particular, we theoretically clarified the modulation of the geometric and electronic structure of h-GaN under the compression, surface hydrogenation, and an external electric field to present possible applications of h-GaN in electronic and piezoelectric devices. Our calculations showed that the biaxial compression causes structural buckling, which leads to the modulation of electronic properties of an isolated sheet of h-GaN: h-GaN is an indirect band gap semiconductor in the planar conformation, while it is a direct band gap semiconductor in its buckled conformation. Furthermore, compressed h-GaN with a buckled conformation possess polarity normal to the sheet, because of the chemical difference between Ga and N atoms. By attaching H atoms onto all Ga and N atoms, h-GaN preserves the buckled structure, in which the polarity of the sheet is opposite to that of the buckled h-GaN with clean surfaces. In addition, the external electric field normal to the sheet causes the structural modulation of h-GaN from planar to buckled conformations to compensate the external electric field by polarization. These facts imply that h-GaN can be applicable for optoelectronic and piezoelectric devices under the biaxial strain.

We also investigated energetics and electronic structures of thin films and heterostructures of h-GaN using the DFT containing the van der Walls correction. The h-GaN sheets in the thin films are tightly bound each other owing to the small interlayer spacing, so that their electronic structures are sensitive to the number of layers: wave number corresponding to the valence band top monotonically decreases and approaches the Γ point, corresponding to the bulk h-GaN, with increasing the number of atomic layers. The band gap also depends on the number of layers. We further found that GaN thin films with a wurtzite structure undergo a structural phase transition into the layered structures of h-GaN by applying a biaxial tensile strain. The optimum interlayer spacing of both h-GaN/graphene and h-GaN/h-BN is 3.4 Å, indicating that h-GaN sheet is bound to the graphene or h-BN via a weak van der Waal interaction.

In Chapter 4, we studied the electronic structures of graphene edges under an external electric field to clarify field emission properties from graphene edge in terms of the edge shape and functionalization. The armchair edge has lower work function than the other edges, leading to the largest field emission current with the lowest potential barrier for the field emission among edges with various shapes studied here. For chiral edges, the field emission primarily occurs at the zigzag sites because of the electron concentration arising from either the dangling band state or the edge state. Besides the edge shape, the field emission properties from graphene edges are also sensitive to the edge functionalizations. The functional groups H, OH, and COOH decrease the work function of the graphene edge, while O and CHO increase it for both armchair and zigzag edges. Accordingly, the functionalizations by H, OH, and COOH enhance the field emission current by reducing the potential barrier for the field emission, while the functionalizations by O and CHO suppress the current by increasing the potential barrier. For the edges functionalized by the NH, the field emission current from armchair edge is suppressed with the increase of the potential barrier, while the current from zigzag edge is enhanced with the decrease of the potential barrier, because of the different electrostatic environment around the edge atomic sites arising from the NH conformations.

Publications

1. Yanlin Gao, Yayama Tomoe, and Susumu Okada. *Polar properties of a hexagonally bonded GaN sheet under biaxial compression*, Appl. Phys. Express **9** (2016) 095201. (doi: 10.7567/APEX.9.095201)
2. Yanlin Gao and Susumu Okada. *Electrostatic potential barrier for electron emission at graphene edges induced by the nearly free electron states*, Appl. Phys. Express **10** (2017) 055104. (doi: 10.7567/APEX.10.055104)
3. Yanlin Gao and Susumu Okada. *Energetics and electronic structures of thin films and heterostructures of a hexagonal GaN sheet*, Jpn. J. Appl. Phys. **56** (2017) 065201. (doi: 10.7567/JJAP.56.065201)
4. Yayama Tomoe, Yanlin Gao, and Susumu Okada, and Toyohiro Chikyow. *Polarization modulation of nanotrenches in GaN (0001)/(000-1) by surface hydrogenation.* Jpn. J. Appl. Phys. **56** (2017) 111002. (doi: 10.7567/JJAP.56.111002)
5. Yanlin Gao and Susumu Okada. *Electrostatic properties of graphene edges for electron emission under an external electric field.* Appl. Phys. Lett. **112** (2018) 163105. (doi: 10.1063/1.5023845)
6. Yanlin Gao and Susumu Okada. *Field emission properties of edge-functionalized graphene.* Carbon **142** (2019) 190–195. (doi: 10.1016/j.carbon.2018.10.019)

Acknowledgments

I would like to deeply acknowledge my supervisor Prof. Susumu Okada for his continuous supports during my Ph.D. course at University of Tsukuba. I also would like to express my special appreciation to Prof. Takazumi Kawai for his kind and fruitful advices. I would like to express my appreciation to Dr. Mina Maruyama, Dr. Ayaka Yamanaka, and Ms. Manaho Matsubara for their conversations, discussions, and friendship with me, which make my doctoral life more colorful and interesting. I am also thankful to all members in the research group of Prof. Okada for their supports. I acknowlege the scholarship support from the Japan Ministry of Education, Culture, Sports, Science and Technology (MEXT) of Japan, and I am also in debt to the Japan Society for the Promotion of Science (JSPS) for being a doctoral researcher (DC2 category). Finally, I also would like to thank my family. With their continuous supports and love, I am able to take the path to pursue my doctoral degree.

Bibliography

[1] K. S. Novoselov, A. K. Geim, S. V. Morozov, D. Jiang, M. I. Katsnelson, I. V. Grigorieva, S. V. Dubonos, and A. A. Firsov, *Two-dimensional gas of massless Dirac fermions in graphene*, Nature **438**, 197–200, 2005.

[2] K. I. Bolotin, K. J. Sikes, Z. Jiang, M. Klima, G. Fudenberg, J. Hone, P. Kim, and H. L. Stormer, *Ultrahigh electron mobility in suspended graphene*, Solid State Commun. **146**, 351–355, 2008.

[3] J. B. Oostinga, H. B. Heersche, X. Liu, A. F. Morpurgo, and L. M. K. Vandersypen, *Gate-induced insulating state in bilayer graphene devices*, Nat. Mater. **146**, 151–157, 2008.

[4] Y. Zhang, T. Tang, C. Girit, Z. Hao, M. C. Martin, A. Zettl, M. F. Crommie, Y. R. Shen, and F. Wang, *Direct observation of a widely tunable bandgap in bilayer graphene*, Nature **459**, 820–823, 2009.

[5] M. J. Allen, V. C. Tung, and R. B. Kanter, *Honeycomb carbon: A review of graphene*, Chem. Rev. **110**, 132–145, 2010.

[6] Y. Zhang, Y. W. Tan, H. L. Stormer, and P. Kim, *Experimental observation of the quantum Hall effect and Berry's phase in graphene*, Nature **438**, 201–204, 2005.

[7] C. L. Kane and E. J. Mele, *Quantum spin Hall effect in graphene*, Phys. Rev. Lett. **95**, 226801, 2005.

[8] C. Lee, X. Wei, J. W. Kysar, and J. Hone, *Measurement of the elastic properties and intrinsic strength of monolayer graphene*, Science **321**, 385–388, 2008.

[9] A. A. Balandin, S. Ghosh, W. Bao, I. Calizo, D. Teweldebrhan, F. Miao, and C. N. Lau, *Superior thermal conductivity of single-layer graphene*, Nano Lett. **8**, 902–907, 2008.

[10] K. S. Novoselov, A. K. Geim, S. V. Morozov, D. Jiang, Y. Zhang, S. V. Dubonos, I. V. Grigorieva, and A. A. Firsov, *Electric field effect in atomically thin carbon films*, Science **306**, 666–669, 2004.

[11] S. Trivedi, A. Srivastava, and R. Kurchania, *Silicene and germanene: A first principle study of electronic structure and effect of hydrogenation-passivation*, J. Comput. Theor. Nanosci. **11**, 781–787, 2014.

[12] B. Lalmi, H. Oughaddou, H. Enriquez, A. Kara, S. Vizzini, B. Ealet, and B. Aufray, *Epitaxial growth of a silicene sheet*, Phys. Rev. B **97**, 223109, 2010.

[13] A. Fleurence, R. Friedlein, T. Ozaki, H. Kawai, Y. Wang, and Y. Yamada-Takamura, *Experimental evidence for epitaxial silicene on diboride thin films*, Phys. Rev. Lett. **108**, 245501, 2013.

[14] L. Meng, Y. Wang, L. Zhang, S. Du, R. Wu, L. Li, Y. Zhang, G. Li, H. Zhou, W. A. Hofer, and H.-J. Gao, *Buckled silicene formation on Ir(111)*, Nano Lett. **13**, 685–690, 2013.

[15] K. Takeda and K. Shiraishi, *Theoretical possibility of stage corrugation in Si and Ge analogs of graphite*, Phys. Rev. B 50, **50**, 14916, 1994.

[16] Y. L. Liu, G. X. Luo, N. Xu, H. Y. Tian, and C. D. Ren, *Integer quantum Hall effect and topological phase transitions in silicene*, Condens. Matter Phys. **20**, 43701, 2017.

[17] M. Topsakal, E. Akturk, and S. Ciraci, *First-principles study of two- and one-dimensional honeycomb structures of boron nitride*, Phys. Rev. B **79**, 115442, 2009.

[18] A. Kuc, Z. Nourdine, and T. Heine, *Influence of quantum confinement on the electronic structure of the transition metal sulfide* TS_2, Phys. Rev. B **83**, 245213, 2011.

[19] G. L. Yu, R. Jalil, B. Belle, A. S. Mayorov, P. Blake, F. Schedin, S. V. Morozov, L. A. Ponomarenko, F. Chiappini, S. Wiedmann, U. Zeitler, M. I. Katsnelson, A. K. Geim, K. S. Novoselov, and D. C. Elias, *Interaction phenomena in graphene seen through quantum capacitance*, Chem. Rev. **110**, 3282–3286, 2013.

[20] G. Rudren and Z. Qing, *Few-layer* MoS_2*: A promising layered semiconductor*, ACS Nano **8**, 4074–4099, 2014.

[21] K. Nakada, M. Fujita, G. Dresselhaus, and M. S. Dresselhaus, *Edge state in graphene ribbons: Nanometer size effect and edge shape dependence*, Phys. Rev. B **54**, 17954, 1996.

[22] M. Fujita, K. Wakabayashi, K. Nakada, and K. Kusakabe, *Peculiar localized state at zigzag graphite edge*, J. Phys. Soc. Jpn. **65**, 1920–1923, 1996.

[23] Y.-W. Son, M. L. Cohen, and S. G. Louie, *Energy gaps in graphene nanoribbons*, Phys. Rev. Lett. **97**, 216803, 2006.

[24] S. Cahangirov, M. Topsakal, and S. Ciraci, *Armchair nanoribbons of silicon and germanium honeycomb structures*, Phys. Rev. B **81**, 195120, 2010.

[25] Y.-L. Song, Y. Zhang, J.-M. Zhang, and D.-B. Lu, *Effects of the edge shape and the width on the structural and electronic properties of silicene nanoribbons*, Appl. Surf. Sci. **256**, 6313–6317, 2010.

[26] C.-H. Park and S. G. Louie, *Energy gaps and stark effect in boron nitride nanoribbons*, Nano Lett. **8**, 2200–2203, 2008.

[27] Y. Li, Z. Zhou, S. Zhang, and Z. Chen, *MoS_2 nanoribbons: High stability and unusual electronic and magnetic properties*, J. Am. Chem. Soc. **130**, 16739–16744, 2008.

[28] A. R. Botello-Méndez, F. López-Urías, M. Terrones, and H. Terrones, *Metallic and ferromagnetic edges in molybdenum disulfide nanoribbons*, Nanotechnology **20**, 325703, 2009.

[29] C. Ataca, H. Sahin, E. Akturk, and S. Ciraci, *Mechanical and electronic properties of MoS_2 nanoribbons and their defects*, J. Phys. Chem. C **115**, 3934–3941, 2011.

[30] H. Pan and Y.-W. Zhang, *Edge-dependent structural, electronic and magnetic properties of MoS_2 nanoribbons*, J. Mater. Chem. **22**, 7280–7290, 2012.

[31] A. Yamanaka and S. Okada, *Energetics and electronic structure of h-BN nanoflakes*, Scientific Reports **6**, 30653, 2016.

[32] M. Koshino, *Stacking-dependent optical absorption in multilayer graphene*, New J. Phys. **15**, 015010, 2013.

[33] K. F. Mak, J. Shan, and T. F. Heinz, *Electronic structure of few-layer graphene: experimental demonstration of strong dependence on stacking sequence*, Phys. Rev. Lett. **104**, 176404, 2010.

[34] A. H. C. Neto, *The electronic properties of graphene*, Rev. Mod. Phys. **81**, 109, 2009.

[35] K. F. Mak, M. Y. Sfeir, J. A. Misewich, and T. F. Heinz, *The evolution of electronic structure in few-layer graphene revealed by optical spectroscopy*, Proc. Natl. Acad. Sci. U. S. A. **107**, 14999–15004, 2010.

[36] C. Kamal, A. Chakrabarti, A. Banerjee, and S. K. Deb, *Silicene beyond monolayers-different stacking configurations and their properties*, J. Phys.: Condens. Matter **25**, 085508, 2013.

[37] H. Behera and G. Mukhopadhyay, *Strain-tunable band gap in graphene/h-BN hetero-bilayer*, J. Phys. Chem. Solids **73**, 818–821, 2012.

[38] X. D. Li, S. Yu, S. Q. Wu, Y. H. Wen, S. Zhou, and Z. Z. Zhu, *Structural and electronic properties of superlattice composed of graphene and monolayer* MoS_2, J. Phys. Chem. C **117**, 15347–15353, 2013.

[39] Y. Fan, M. Zhao, Z. Wang, X. Zhang, and H. Zhang, *Tunable electronic structures of graphene/boron nitride heterobilayers*, Phys. Rev. Lett. **98**, 083103, 2011.

[40] H. Zhang, Y. Zhang, H. Liu, and L. Liu, *Novel heterostructures by stacking layered molybdenum disulfides and nitrides for solar energy conversion*, J. Mater. Chem. A **2**, 15389–153950, 2014.

[41] S. R. Suryawanshi, P. S. Kolhe, C. S. Rout, D. J. Late, and M. A. More, *Spectral analysis of the emission current noise exhibited by few layer* WS_2 *nanosheets emitter*, Ultramicroscopy **149**, 51–57, 2015.

[42] M. B. Erande, M. A. Suryawanshi, Sachin R. More, and D. J. Late, *Electrochemically exfoliated black phosphorus nanosheets-prospective field emitters*, Eur. J. Inorg. Chem. **2015**, 3102–3107, 2015.

[43] Y. Bando, L. Yin, and D. Golberg, *Field nanoemitters: Ultrathin BN nanosheets protruding from* Si_3N_4 *nanowires*, Nano Lett. **6**, 2982–2986, 2006.

[44] Z.-G. Chen and J. Zou, *Field emitters: ultrathin BN nanosheets protruded from BN fibers*, J. Mater. Chem. **21**, 1191–1195, 2011.

[45] S. Ahmadi, P. D. K. Nezhad, A. Hosseinian, and E. Vessally, *A computational study on tuning the field emission and electronic properties of BN nanocones by impurity atom doping*, Physica E **100**, 63–68, 2018.

[46] D. J. Late, P. A. Shaikh, R. Khare, R. V. Kashid, M. Chaudhary, M. A. More, and S. B. Ogale, *Pulsed laser-deposited MoS_2 thin films on W and Si: Field emission and photoresponse studies*, Appl. Mater. Interfaces **6**, 15881–15888, 2014.

[47] M. Terrones, J.-C. Charlier, A. Gloter, E. Cruz-Silva, E. Terres, Y. B. Li, A. Vinu, Z. Zanolli, J. M. Dominguez, H. Terrones, Y. Bando, and D. Golberg, *Stacking-dependent optical absorption in multilayer graphene*, Nano Lett. **8**, 1026–1032, 2008.

[48] Z. Xiao, J. She, S. Deng, Z. Tang, Z. Li, J. Lu, and N. Xu, *Field electron emission characteristics and physical mechanism of individual single-layer graphene*, ACS Nano **4**, 6332–6336, 2010.

[49] J. T. H. Tsai, T. Y. E. Chu, J. Y. Shiu, and C. S. Yang, *Field emission from an individual freestanding graphene edge*, Small **8**, 3739–3745, 2012.

[50] H. J. Jeong, H. Y. Kim, H. D. Jeong, S. Y. Jeong, J. T. Han, and G.-W. Lee, *Arrays of vertically aligned tubular-structured graphene for flexible field emitters*, J. Mater. Chem. **22**, 11277, 2012.

[51] Y. Zhang, J. Du, S. Tang, P. Liu, S. Deng, J. Chen, and N. Xu, *Optimize the field emission character of a vertical few-layer graphene sheet by manipulating the morphology*, Nanotechnology **23**, 015202, 2012.

[52] K. Tada and K. Watanabe, *Ab initio study of field emission from graphitic ribbons*, Phys. Rev. Lett. **88**, 127601, 2002.

[53] S. F. Huang, T. C. Leung, B. Li, and C. T. Chan, *First-principles study of field-emission properties of nanoscale graphite ribbon arrays*, Phys. Rev. B **72**, 035449, 2005.

[54] P. Hohenberg and W. Kohn, *Inhomogeneous electron gas*, Phys. Rev. **136**, B864, 1964.

[55] W. Kohn and L. J. Sham, *Self-consistent equations including exchange and correlation effects*, Phys. Rev. A **140**, 1133, 1965.

[56] J. P. Perdew and A. Zunger, *Self-interaction correction to density-functional approximations for many-electron systems*, Phys. Rev. B **23**, 5048, 1981.

[57] D. M. Ceperley and B. J. Alder, *Ground state of the electron gas by a stochastic method*, Phys. Rev. Lett. **45**, 566, 1980.

[58] J. P. Perdew, K. Burke, and M. Ernzerhof, *Generalized gradient approximation made simple*, Phys. Rev. Lett. **77**(18), 3865, 1996.

[59] J. P. Perdew, K. Burke, and M. Ernzerhof, *Generalized gradient approximation made simple [phys. rev. lett. 77, 3865 (1996)]*, Phys. Rev. Lett. **78**(7), 1997.

[60] D. Vanderbilt, *Soft self-consistent pseudopotentials in a generalized eigenvalue formalism*, Phys. Rev. B **41**, 7892, 1990.

[61] M. Otani and O. Sugino, *First-principles calculations of charged surfaces and interfaces: A plane-wave nonrepeated slab approach*, Phys. Rev. B **73**, 115407, 2006.

[62] S. Cahangirov, M. Topsakal, E. Akturk, H. Şahin, and S. Ciraci, *Two- and one-dimensional honeycomb structures of silicon and germanium*, Phys. Rev. Lett. **102**, 236804, 2009.

[63] G. G. Guzmán-Verri and L. C. Lew Yan Voon, *Electronic structure of silicon-based nanostructures*, Phys. Rev. B **76**, 075131, 2007.

[64] K. Watanabe, T. Taniguchi, and H. Kanda, *Direct-bandgap properties and evidence for ultraviolet lasing of hexagonal boron nitride single crystal*, Nat Mater. **3**, 404, 2004.

[65] L. Wirtz, A. Marini, and A. Rubio, *Excitons in boron nitride nanotubes: Dimensionality effects*, Phys. Rev. Lett. **96**, 126104, 2006.

[66] R. M. Ribeiro and N. M. R. Peres, *Stability of boron nitride bilayers: Ground-state energies, interlayer distances, and tight-binding description*, Phys. Rev. B **83**, 235312, 2011.

[67] R. J. Molnar, R. Singh, and T. D. Moustakas, *Blue-violet light emitting gallium nitride p-n junctions grown by electron cyclotron resonance-assisted molecular beam epitaxy*, Appl. Phys. Lett. **66**, 268, 1995.

[68] J. M. Van Hove, R. Hickman, J. J. Klassen, and P. P. Chow, *Ultraviolet-sensitive, visible-blind GaN photodiodes fabricated by molecular beam epitaxy*, Appl. Phys. Lett. **70**, 2282, 1998.

[69] Y. Zhao, R. M. Farrell, Y. R. Wu, and J. S. Speck, *Valence band states and polarized optical emission from nonpolar and semipolar III–nitride quantum well optoelectronic devices*, Jpn. J. Appl. Phys. **53**, 100206, 2014.

[70] D. S. Lee, Z. Liu, and T. Palacios, *GaN high electron mobility transistors for sub-millimeter wave applications*, Jpn. J. Appl. Phys. **53**, 100212, 2014.

[71] T. Kachi, *Recent progress of GaN power devices for automotive applications*, Jpn. J. Appl. Phys. **53**, 100210, 2014.

[72] H. Zhao, G. Liu, J. Zhang, J. D. Poplawsky, V. Dierolf, and N. Tansu, *Approaches for high internal quantum efficiency green InGaN light-emitting diodes with large overlap quantum wells*, Opt. Express **19**, A991–A1007, 2011.

[73] X. Liu, Y. Lu, W. Yu, J. Wu, J. He, D. Tang, Z. Liu, P. Somasuntharam, D. Zhu, W. Liu, P. Cao, S. Han, S. Chen, and L. S. Tan, *AlGaN/GaN metal-oxide-semiconductor high-electron-mobility transistor with polarized P(VDF-TrFE) ferroelectric polymer gating*, Scientific Reports **5**, 14092, 2015.

[74] H. Şahin, S. Cahangirov, M. Topsakal, E. Bekaroglu, E. Aktrk, R. T. Senger, and S. Ciraci, *Monolayer honeycomb structures of group-IV elements and III-V binary compounds: First-principles calculations*, Phys. Rev. B **80**, 155453, 2009.

[75] A. Onen, D. Kecik, E. Durgun, and S. Ciraci, *GaN: From three- to two-dimensional single-layer crystal and its multilayer van der Waals solids*, Phys. Rev. B **93**, 085431, 2016.

[76] Y. Morikawa, K. Iwata, and K. Terakura, *Theoretical study of hydrogenation process of formate on clean and Zn deposited Cu(111) surfaces*, Appl. Surf. Sci. **169–170**, 11, 2001.

[77] K. Lee, E. D. Murray, L. Kong, B. I. Lundqvist, and D. C. Langreth, *Higher-accuracy van der Waals density functional*, Phys. Rev. B **82**, 081101(R), 2010.

[78] V. R. Cooper, *Van der Waals density functional: An appropriate exchange functional*, Phys. Rev. B **81**, 161104(R), 2010.

[79] I. Hamada and M. Otani, *Comparative van der Waals density-functional study of graphene on metal surfaces*, Phys. Rev. B **82**, 153412, 2010.

[80] K. Miwa and A. Fukumoto, *First-principles calculation of the structural, electronic, and vibrational properties of gallium nitride and aluminum nitride*, Phys. Rev. B **48**, 7897, 1993.

[81] M. Posternak, A. Baldereschi, A. J. Freeman, E. Wimmer, and M. Weinert, *Prediction of electronic interlayer states in graphite and reinterpretation of alkali bands in graphite intercalation compounds*, Phys. Rev. Lett. **50**, 761, 1983.

[82] M. Posternak, A. Baldereschi, A. J. Freeman, and E. Wimmer, *Prediction of electronic surface states in layered materials: Graphite*, Phys. Rev. Lett. **52**, 863, 1984.

[83] A. Catellani, M. Posternak, A. Baldereschi, and A. J. Freeman, *Bulk and surface electronic structure of hexagonal boron nitride*, Phys. Rev. B **36**, 6105, 1987.

[84] X. Blase, A. Rubio, S. G. Louie, and M. L. Cohen, *Quasiparticle band structure of bulk hexagonal boron nitride and related systems*, Phys. Rev. B **51**, 6868, 1995.

[85] N. T. Cuong, M. Otani, and S. Okada, *Gate-induced electron-state tuning of* MoS_2*: First-principles calculations*, J. Phys. Condens. Matter **26**, 135001, 2014.

[86] A. Yamanaka and S. Okada, *Electron injection into nearly free electron states of graphene nanoribbons under a lateral electric field*, Appl. Phys. Express **7**, 125103, 2014.

[87] T. Enoki, M. Suzuki, and M. Endo, *Graphite intercalation compounds and applications*, Oxford University Press, 2003.

[88] M. S. Dresselhaus and G. Dresselhaus, *Intercalation compounds of graphite*, Adv. Phys. **30**, 139, 1981.

[89] K. Shiraishi, *A new slab model approach for electronic structure calculation of polar semiconductor surface*, J. Phys. Soc. Jpn. **59**, 3455, 1990.

[90] M. Xiao, T. Yao, Z. Ao, P. Wei, D. Wang, and H. Songa, *Tuning electronic and magnetic properties of GaN nanosheets by surface modifications and nanosheet thickness*, Phys. Chem. Chem. Phys **17**, 8692, 2015.

[91] D. Xu, H. He, R. Pandey, and S. P. Karna, *Stacking and electric field effects in atomically thin layers of GaN*, J. Phys.: Condens. Matter **25**, 345302, 2013.

[92] G. Graziano, J. Klimeš, F. Fernandez-Alonso, and A. Michaelides, *Improved description of soft layered materials with van der Waals density functional theory*, J. Phys.: Condens. Matter **24**, 424216, 2012.

[93] M. F. Craciun, S. Russo, M. Yamamoto, J. B. Oostinga, A. F. Morpurgo, and S. Tarucha, *Trilayer graphene is a semimetal with a gate-tunable band overlap*, Nat. Nanotechnol. **4**, 383–388, 2009.

[94] Y. Ma, P. O. Lehtinen, A. S. Foster, and R. M. Nieminen, *Magnetic properties of vacancies in graphene and single-walled carbon nanotubes*, New J. Phys. **6**, 68, 2004.

[95] H. Amara, S. Latil, V. Meunier, P. Lambin, and J. C. Charlier, *Scanning tunneling microscopy fingerprints of point defects in graphene: A theoretical prediction*, Phys. Rev. B **76**, 115423, 2007.

[96] M. M. Ugeda, I. Brihuega, F. Hiebel, P. Mallent, J. Y. Veuillen, J. M. Gómez-Rodriguez, and F. Ynduráin, *Electronic and structural characterization of divacancies in irradiated graphene*, Phys. Rev. B **85**, 121402(R), 2012.

[97] M. Dvorak, W. Oswald, and Z. Wu, *Bandgap opening by patterning graphene*, Sci. Rep. **3**, 2289, 2013.

[98] Y. Miyamoto, K. Nakada, and M. Fujita, *Edge state in graphene ribbons: Nanometer size effect and edge shape dependence*, Phys. Rev. B **59**, 9858, 1999.

[99] S. Okada and A. Oshiyama, *Magnetic ordering in hexagonally bonded sheets with first-row elements*, Phys. Rev. Lett. **87**, 146803, 2001.

[100] T. G. Pedersen, C. Flindt, J. Pedersen, N. A. Mortensen, A. P. Jauho, and K. Pedersen, *Graphene antidot lattices: Designed defects and spin qubits*, Phys. Rev. Lett. **100**, 136804, 2008.

[101] J. O. Sofo, A. S. Chaudhari, and G. D. Barber, *Graphane: A two-dimensional hydrocarbon*, Phys. Rev. B **75**, 153401, 2007.

[102] J. Zhou, M. M. Wu, X. Zhou, and Q. Sun, *Tuning electronic and magnetic properties of graphene by surface modification*, Appl. Phys. Lett. **95**, 103108, 2009.

[103] F. Withers, T. H. Bointon, M. Dubois, S. Russo, and M. F. Craciun, *Nanopatterning of fluorinated graphene by electron beam irradiation*, Nano Lett. **11**, 3912–3916, 2011.

[104] N. T. Cuong, M. Otani, and S. Okada, *Electron-state engineering of bilayer graphene by ionic molecules*, Appl. Phys. Lett. **101**, 233106, 2012.

[105] S. Y. Zhou, G. H. Gweon, A. V. Fedorov, P. N. First, W. A. d. Heer, D. H. Lee, F. Guinea, A. H. C. Neto, and A. Lanzara, *Substrate-induced bandgap opening in epitaxial graphene*, Nat. Mater. **6**, 770–775, 2007.

[106] A. Mattausch and O. Pankratov, *Ab initio study of graphene on SiC*, Phys. Rev. Lett. **99**, 076802, 2007.

[107] N. T. Cuong, M. Otani, and S. Okada, *Semiconducting electronic property of graphene adsorbed on (0001) surfaces of* SiO_2, Phys. Rev. Lett. **106**, 106801, 2011.

[108] K. Kamiya, N. Umezawa, and S. Okada, *Energetics and electronic structure of graphene adsorbed on* HfO_2 *(111): Density functional theory calculations*, Phys. Rev. Lett. **83**, 153413, 2011.

[109] K. A. Ritter and J. W. Lyding, *The influence of edge structure on the electronic properties of graphene quantum dots and nanoribbons*, Nat. Mater. **8**, 235–242, 2009.

[110] G. M. Rutter, N. P. Guisinger, J. N. Crain, P. N. First, and J. A. Stroscio, *Edge structure of epitaxial graphene islands*, Phys. Rev. B **81**, 245408, 2010.

[111] J. Tian, H. L. Cao, W. Wu, Q. K. Yu, and Y. P. Chen, *Direct imaging of graphene edges: Atomic structure and electronic scattering*, Nano Lett. **11**, 3663–3668, 2011.

[112] V. Barone, O. Hod, and G. E. Scuseria, *Electronic structure and stability of semiconducting graphene nanoribbons*, Nano Lett. **06**, 2748–2754, 2006.

[113] S. Okada, *Energetics of nanoscale graphene ribbons: Edge geometries and electronic structures*, Phys. Rev. B **77**, 041408(R), 2008.

[114] A. Yamanaka and S. Okada, *Energetics and electronic structure of graphene nanoribbons under a lateral electric field*, Carbon **96**, 351–361, 2016.

[115] D. Gunlycke, J. Li, and J. W. Mintmire, *Altering low-bias transport in zigzag-edge graphene nanostrips with edge chemistry*, Appl. Phys. Lett. **91**, 112108, 2007.

[116] R. Taira and S. Okada, *Electronic structure modulation of graphene edges by chemical functionalization*, Appl. Phys. Express **9**, 115102, 2016.

[117] C.-C. Liu, W. Feng, and Y. Yao, *Quantum spin Hall effect in silicene and two-dimensional germanium*, Phys. Rev. Lett. **107**, 076802, 2011.

[118] V. I. Kleshch, D. A. Bandurin, A. S. Orekhov, S. T. Purcell, and A. N. Obraztsov, *Edge field emission of large-area single layer graphene*, Appl. Surf. Sci. **357**, 1967–1974, 2015.

[119] A. D. Bartolomeo, F. Giubileo, L. Iemmo, F. Romeo, S. Russo, S. Unal, M. Passacantando, V. Grossi, and A. M. Cucolo, *Leakage and field emission in side-gate graphene field effect transistors*, Appl. Phys. Lett. **109**, 023510, 2016.

[120] C. Wu, F. Li, Y. Zhang, and T. Guo, *Field emission from vertical graphene sheets formed by screen-printing technique*, Vacuum **94**, 48–52, 2013.

[121] A. Malesevic, R. Kemps, A. Vanhulsel, M. P. Chowdhury, A. Volodin, and C. V. Haesendonck, *Field emission from vertically aligned few-layer graphene*, J. Apply. Phys. **104**, 084301, 2008.

[122] M. Araidai, Y. Nakamura, and K. Watanabe, *Field emission mechanisms of graphitic nanostructures*, Phys. Rev. B **70**, 245410, 2004.

[123] Y. Gao and S. Okada, *Electrostatic potential barrier for electron emission at graphene edges induced by the nearly free electron states*, Appl.Phys.Express **10**, 055104, 2017.

[124] T. Kawai, Y. Miyamoto, O. Sugino, and Y. Koga, *Graphitic ribbons without hydrogen-termination: Electronic structures and stabilities*, Phys. Rev. B **62**, R16349(R), 2000.